

ELECTROCHEMICAL IMPEDANCE SPECTROSCOPY WEARABLE SYSTEMS FOR
REPORTING BIOMARKER MODULATION IN SWEAT

by

Devangsingh Gajendar Singh Sankhala

APPROVED BY SUPERVISORY COMMITTEE:

Shalini Prasad, Chair

Dinesh Bhatia, Co-Chair

Sriram Muthukumar

Poras T. Balsara

Copyright 2021

Devangsingh Gajendar Singh Sankhala

All Rights Reserved

In God we trust, all others bring data.
W. Edward Deming

Time you enjoy wasting, was not wasted time.
John Lennon

ELECTROCHEMICAL IMPEDANCE SPECTROSCOPY WEARABLE SYSTEMS FOR
REPORTING BIOMARKER MODULATION IN SWEAT

by

DEVANGSINGH GAJENDAR SINGH SANKHALA, BE, MS

DISSERTATION

Presented to the Faculty of
The University of Texas at Dallas
in Partial Fulfillment
of the Requirements
for the Degree of

DOCTOR OF PHILOSOPHY IN
ELECTRICAL ENGINEERING

THE UNIVERSITY OF TEXAS AT DALLAS

December 2021

ACKNOWLEDGMENTS

The journey of pursuing my Ph.D. degree has been one of the most challenging and eye-opening experiences of my life. It has been full of opportunities to learn, understand, implement, and improve upon unique designs as well as my skills. I would like to take this opportunity to thank the people who have made this journey a success.

I would like to begin with my advisor, Dr. Shalini Prasad, and Dr. Sriram Muthukumar for providing me with this opportunity of designing the first few stable prototypes for the lab. It involved countless days and nights, guidance, and of course, literal blood and sweat! I sincerely thank my co-advisor, Dr. Dinesh Bhatia, and Dr. Poras Balsara for their continued support and guidance. They are a great source of inspiration, advice, company, and foresightedness.

Great research cannot be achieved without great teamwork. Hence, I would like to thank my colleagues, people who came together from various disciplines to achieve something phenomenal and greater than themselves: Badri, Ambalika, Ashlesha, Sayali, David, Paul, Kevin, Madhavi, Vikram, Antra, Abha, Nathan, Nella, Sarah, Sasya, Anirban, Ivneet and Durgasha. It was a pleasure working with all of them in some way. I would like to thank all the undergraduate student workers for their help and support: Roshan, Aashay, Saqib, Ruinan, Steven, Joshua, and Alice. Our work is never finished, but we are proud of the progress we have made together.

I would also like to thank the people who invested their time to make me the person I am today. I thank my mother Rita, father Gajendar, uncle Mahendar and aunt Mansi for their love and support.

My grandfather Retired Sergeant Ranjit Singh Sankhala has instilled values like punctuality, integrity, and steadfastness in me. My brother Yash and my cousins Jay and Prachi have been the source of joy in my life. I will always remain indebted to my family. Finally, I thank the friends I made along the way who helped me in innumerable ways outside studies: Amar, Kaushal, Kirtan, Maitrey, Jay, Vivek, Jimmy, Jaydeep, Jainish, Hardik, Aditya, Nikhil, Rithesh, Matthew, Trusit, Shreyas, Pingu, Satwik.

November 2021

ELECTROCHEMICAL IMPEDANCE SPECTROSCOPY WEARABLE SYSTEMS FOR REPORTING BIOMARKER MODULATION IN SWEAT

Devangsingh Gajendar Singh Sankhala, PhD
The University of Texas at Dallas, 2021

Supervising Professor: Shalini Prasad, Chair
Dinesh Bhatia, Co-Chair

The commercial wearable device market today majorly consists of activity trackers and smartwatches: that enable the monitoring of user states such as walking, sleeping, and exercising using sensors relying on physically measurable quantities. These devices are the ones that make a huge impact on the lives of people suffering from chronic illnesses and their quality of life. Integrating a sweat-based electrochemical biosensor with a wearable device opens new avenues in health management and decision support systems for healthcare providers as they can provide a physiologically relevant and clinically acceptable output. Integrating a glucose-sensing sweat biosensor adds more value in the lives of diabetics, who require support in terms of balancing quality of life using good diet and exercise routines. This work is a methodology of understanding the aspects of making such a wearable platform, starting from understanding the needs of the wearable device user population. The current market technology is thoroughly studied to pick relevant aspects and an electronic front end is designed within the bounds of good design practice to enable good accuracy, ease of use, and 1-week battery life. This in turn is utilized to collect human subject data to get an understanding of the performance of the sensors in varying

environmental conditions and user states. Finally, mathematical modeling approaches are used to build correlations between the outcome to be presented to the user against change in the recorded data features as per the human subject experimentation.

TABLE OF CONTENTS

ACKNOWLEDGMENTS	v
ABSTRACT.....	vii
LIST OF FIGURES	xii
LIST OF TABLES	xvi
 CHAPTER 1 INTRODUCTION	 1
1.1 Overview	1
1.2 Motivation and problem analysis.....	1
1.3 Proposed research	2
 CHAPTER 2 SPECIFICATION DEFINITION FOR WEARABLE DEVICES	 3
2.1 Expanse and user acceptance criteria for wearable devices.....	3
2.2 Anatomy of a wearable device.....	6
2.3 Classification of sensing mechanisms	12
2.4 Types of electrochemical sensing techniques	14
2.4.1 Potentiometric sensing	14
2.4.2 Amperometric sensing.....	15
2.4.3 Conductometric sensing	15
2.4.4 Impedimetric sensing	15
2.5 Concept of impedance.....	16
2.6 Types of impedance measurement techniques.....	17
2.6.1 Zero crossing detector	18
2.6.2 Lissajous patterns	19
2.7 Comprehensive digital assistance for impedance measurements	21
2.7.1 Odd and even part of a signal.....	21
2.7.2 Extraction of odd and even parts.....	22
2.7.3 Simulation-based verification	23
 CHAPTER 3 DESIGN AND VALIDATION OF THE PROPOSED WEARABLE DEVICE ..	 26

3.1	Sensors and wearables for diabetes.....	26
3.1.1	Evolution of the glucose biosensor	26
3.1.2	Contemporary clinical and wearable glucose-sensing technology	28
3.2	Design objectives of the proposed wearable device	30
3.3	Analysis of lab instrument circuitry.....	31
3.4	Selection of measurement hardware	35
3.5	System-level design methodology for proposed wearable device.....	36
3.6	Dry-load calibration	37
3.7	Calibration using control buffers	40
3.8	Effect of temperature and RH.....	41
3.9	Incremental noise analysis of the sensor.....	43
3.10	Finite state machine (FSM) approach to firmware implementation	46
3.11	Power optimization using time-averaging	48
CHAPTER 4	MODELLING SENSOR BEHAVIOR FOR HUMAN SUBJECT DATA.....	50
4.1	Collection of human subject data.....	50
4.2	Methods of modeling	51
4.3	Exploratory data analysis and preparation.....	51
4.3.1	Interpolation	54
4.4	Machine learning-based regression.....	55
4.4.1	Generalization	58
4.4.2	Validation methodology.....	59
4.4.3	Training results.....	60
4.4.4	Test results.....	61
4.5	Time series analysis	62
4.5.1	Trend	62
4.5.2	Seasonality	62
4.5.3	Autocorrelation.....	65
4.5.4	Stationarity in time-series data.....	66
4.5.5	Operations on time-series data	67
4.5.6	ARIMA modeling and test results.....	69

CHAPTER 5 CONCLUSION.....	73
APPENDIX ELECTRICAL DESIGN DOCUMENTATION.....	74
REFERENCES	86
BIOGRAPHICAL SKETCH	92
CURRICULUM VITAE.....	93

LIST OF FIGURES

Figure 2.1. An infographic of a consumer survey report that highlights acceptance of the form factor of wearable devices. Source: [10][11].....	4
Figure 2.2. Acceptance percentage of a new wearable device among new users versus experienced users in a survey. Source: [10].....	5
Figure 2.3. Major reasons cited in a survey as to why a user chose to abandon a wearable device. Source: [10].....	6
Figure 2.4. Classification of wearable devices into basic versus the high end. Source: [12]	7
Figure 2.5. Teardown of a Microsoft® Band. The PPG sensor and the board are in the center of the band, whereas 2 batteries are integrated into the band body[15].....	10
Figure 2.6. A motherboard of the Huawei® Watch 3 centered around Ambiq Apollo® 4 ARM® processor with an active current of 4μA/MHz. The recess above the processor is for the battery, whereas auxiliary circuits are on the other side of the board (not shown)[16].....	10
Figure 2.7. A motherboard of the Fitbit® Sense with a Mediatek® GPS SoC, Kingston® external flash memory, USI® BLE module, and FitBit® application SoC. Auxiliary sensors are on the other side of this board (not shown)[17].....	11
Figure 2.8. Teardown of a variant of Apple® Watch Series 6 with the S6 system-in-package (SiP) with connectors allowing access for auxiliary circuits (power, wireless communication) to interface (not shown)[18].	11
Figure 2.9. Classification of sensing mechanisms in mainstream use. Source: [19]	12
Figure 2.10. Classification of biosensors used in mainstream testing scenarios. This work focuses on the integration of impedimetric sensors. Source: [20]	13
Figure 2.11. A generic signal flow for a biosensor system. Source: [20].....	14
Figure 2.12. A comparison of schematics for commonly used electrochemical sensing techniques such as (A) Amperometric/voltammetric (B) potentiometric (C) conductometric and (D) impedimetric biosensors. Source: [19]	16
Figure 2.13. A phase measurement circuit for a piezoelectric transducer using a threshold detector and an XOR gate, reprinted from [26].	18
Figure 2.14. Trigonometric evaluation of Lissajous curves to the slope and phase of the input signal [27].	20

Figure 2.15. Output for a Lissajous pattern for variation of frequency and phase of one signal to the other.	21
Figure 2.16. Comparison of an even versus an odd function.....	22
Figure 2.17. A MATLAB® Simulink model of the FFT-based impedance measurement system using a conductance transfer function for resistance and Randle’s circuit. This method will be used for impedance measurement in subsequent works.	25
Figure 3.1. Evolution of glucose biosensors over the last century. Source [36].....	27
Figure 3.2. An ideal representation of a programmable potentiostat with necessary signal generation, excitation, sensing and signal conditioning blocks. Source: [54]	32
Figure 3.3. Signal generation architecture for the Gamry® Reference 3000. Source: [55]	32
Figure 3.4. Electrochemical cell connection to the Gamry® Reference 3000. Source: [55].....	33
Figure 3.5. Voltage and current sensing ADC circuitry channel for the Gamry® Reference 3000. Source: [55].....	34
Figure 3.6. A system-level representation of the proposed FFT-based impedance measurement wearable device. Auxiliary circuits include Bluetooth Low Energy, LiPo battery management, and temperature + RH sensor.	37
Figure 3.7. A universal dummy cell by Gamry Instruments®. All calibration experiments for this work were done using the side marked for calibration.	38
Figure 3.8. Comparison of measured accuracy for Gamry measured impedance values versus the wearable device for a universal load cell.	39
Figure 3.9. Comparison of measured precision for Gamry measured impedance values versus the wearable device for a universal load cell.	39
Figure 3.10. A. Calibration dose-response of the system using synthetic sweat buffer of various pH. B. A box-whisker plot is used to observe the true variability of a given dose concentration as a composite of all buffers used in this experiment.	41
Figure 3.11. The sensor module was connected to four cortisol biosensors and placed in the temperature chamber for temperature testing. The change of measured impedance parameters was recorded, along with the instantaneous temperature. Cortisol doses made in synthetic sweat buffer of pH 4 and 8 were used for this experiment. (B) The test conditions for temperature study include an increase of dose concentration every 5 min and a change of temperature as per a profile. (C) Fractional change of Zmod. (D) Fractional change of Zimag. The change in Zimag is a quadratic function corresponding to an increase in cortisol dose concentration irrespective of change in temperature[57].	42

Figure 3.12. (a) A cross-section of antigen-antibody interaction on the functionalized biosensor surface. (b) Cross-section of the materials of the biosensor when placed on the skin (not to scale). (c) Incremental circuit model of the biosensor. (d) Noise source superposition on the incremental circuit model. (e) FFT noise spectrum of the biosensor when dosed with synthetic sweat without glucose, demarcated with noise margins. (f) Noise voltage level progression for the 100 Hz band of the FFT spectrum over 30 minutes.....	46
Figure 3.13. An example of a finite state machine for the proposed wearable device with states demarcated as S_n and relevant flags.	47
Figure 3.14. Measured current consumption of the proposed wearable device using a DC power analyzer. Each of the FSM states is demarcated to highlight the shape of the current waveform as per firmware execution.	49
Figure 4.1. Classification of methods of data modeling for the proposed wearable device. The methods shown in bold are discussed in this work.	51
Figure 4.2. (A) Box plot of values of selected features across the data collected from various subjects. (B) Correlation matrix of the selected features for the training data.	52
Figure 4.3. Concept diagram of interpolation signal generation using reference points.	54
Figure 4.4. Complete system-level diagram of the wearable device-app-cloud platform infrastructure to support collection, curation, and analysis of sweat biosensor data, part 1 of 2.	56
Figure 4.5. Complete system-level diagram of the wearable device-app-cloud platform infrastructure to support collection, curation, and analysis of sweat biosensor data, part 2 of 2.	57
Figure 4.6. Change in the skew of interpolated training dataset when adding Gaussian noise with varying equivalent SNR of the output signal. This affects the change in train and test loss.	58
Figure 4.7. An example of the workflow of the k-fold validation methodology.	59
Figure 4.8. Comparison of the RMSE and R^2 values obtained for various machine learning regression models used during the model training process.	60
Figure 4.9. Results obtained on the test dataset for the 3 human subject data showing the actual progression of reported values and interpolated reference values.	61
Figure 4.10. An example of an autoregression function with window sizes 8, 16, and 24 when evaluated for a square wave pulse. Higher AR order implies a good fit for fast-moving input signals.	68

Figure 4.11. An example of a moving average function with window sizes 3 and 9 when evaluated for a square wave pulse. Higher window size implies a sluggish response in time.	68
Figure 4.12. (A) Autocorrelation plot for Zmod for subject 1. (B) Autocorrelation plot for Zmod for subject 2. (C) Autocorrelation plot for dZmod for subject 1. (D) Autocorrelation plot for dZmod for subject 2. (E) Skin temperature and relative humidity for subject 1. (F) Skin temperature and relative humidity for subject 2.	71
Figure 4.13. (A) Comparison of interpolated vs. RegARIMA sweat glucose concentrations for subject 1. (B) Comparison of interpolated vs. RegARIMA sweat glucose concentrations for subject 2. (C) Histogram of residuals for ARIMA(10,0,3) model.	72
Figure A.1. Schematic, printed circuit board layers and assembly information for the proposed wearable device.	74

LIST OF TABLES

Table 3.1. Comparison of prevalent glucose level measurements.	28
Table 3.2. Comparison of commercial continuous glucose monitoring devices.	29
Table 4.1. ARIMA (10,0,3) coefficients.....	70
Table A.1. Pick and place information for components used for the wearable device.....	83
Table A.2. Bill of materials for the components used in the wearable device.	84

CHAPTER 1

INTRODUCTION

1.1 Overview

Wearable healthcare devices are envisioned to be the modern technology that will disrupt methods of diagnosis and significantly enhance human health[1]. These will enable patients to monitor their health themselves, without the need for blood-based diagnostic procedures; take responsibility for their health, and be better informed about dynamic changes to their health[2].

1.2 Motivation and problem analysis

According to the CDC National Center for Health Statistics, the prevalence of obesity in adults was 42.4% in 2018. With the hectic lifestyle combined with the decrease in the quality of food being consumed, these numbers are expected to skyrocket by the end of this decade[3]. This prevalence has led to World Health Organization (WHO) declaring obesity as a major unmet public health problem[4], [5]. Obesity is linked to several pathological disorders including hypertension, type 2 diabetes mellitus, cardiovascular diseases, cancer, respiratory system abnormalities, sleep disorders, and metabolic disorders[6]. Specifically, this obesity pandemic has resulted in a dramatic increase in cases of type 2 diabetes mellitus and cardiovascular diseases. However, the outcomes of being obese do not often lead to complications resulting in the development of lifestyle disorders. This case-by-case variation in the disease progression is caused due to a complex interplay of genetic and environmental factors that contributed to obesity in the first place. The origins of this disease can be either due to genetic predisposition or due to dietary intake combined with a sedentary lifestyle[7]. One of the factors that exacerbate the outcomes of obesity

includes dietary fat and carbohydrate intake[8]. With the recent advancement in the development of point-of-need wearables, it has now become feasible to monitor both glucose and cortisol independently in a noninvasive manner. Human eccrine sweat has emerged to be the bio-fluid of choice toward enabling the dynamic and on-demand tracking of these biomarkers[9].

1.3 Proposed research

The key to informed health-related decision-making would be a system that has the capability of reporting on-demand measurements for several biomolecules. This work is a methodology for designing such a wearable hardware and software infrastructure around a novel passive-sweat biosensor, albeit the conventional approach of designing lancet-based approaches. Preexisting wearable device architectures are studied and discussed to come up with the specifications and needs of such an on-demand wearable system. Thereafter, the concept of electrochemical impedance spectroscopy (EIS) is discussed along with probable implementation methods and trade-offs. This led to the conception of a power-efficient, small form-factor, EIS-based wearable device with wireless communication capability, which was tested for accuracy, battery life, reliable output using controlled buffer solutions, and inherent noise threshold. Finally, the data collection of human data, exploratory data analysis, and two methodologies of data analyses are discussed.

CHAPTER 2

SPECIFICATION DEFINITION FOR WEARABLE DEVICES

The creation of an electrochemical wearable platform incorporates 2 major components: a sensing element and an electronic measurement front-end. However, it is important to discuss how these two blocks will come together to interact to form the system that will be called a wearable device to the levels of acceptance of the target user population. Modern wearable devices are aimed to utilize physical sensing methods such as acceleration, location, infrared reflectance for heart rate, and oxygen saturation to build correlations between states of activity. However, they may not be a true reflection of the bodily function of the user, and it would add value to integrate an electrochemical or biological sensing modality to a wearable. To do so, this chapter is an understanding of how wearable devices are perceived by users and how they can be made better and more lucrative to use, in turn adding more value to the quality of life of the user.

2.1 Expanse and user acceptance criteria for wearable devices

From the bulky mobile phone wristwatches from the 2000s to the latest fitness bands, wearable technology has dramatically evolved in recent years. Now, wearables are changing the way consumers interact with the environment, and their popularity is growing. However, the wearables market is still in the early phases of expansion and currently dominated by health, wellness, and activity tracking devices – despite industry developments pointing to an increasing number of use cases[10]. It would be helpful to understand how wearables might break beyond health and wellness scenarios and cover more diverse needs.

The first criterion of user acceptance begins with the form factor of the device. Figure 2.1 shows the results of a survey[11] about what form factor would be ideal for users to see and use for a wearable device. 29% of the survey population voted for a wearable that could be embedded into clothing, 28% voted for a wearable to wear on the wrist, whereas smaller percentages voted for wearables that can be worn on the arm, legs, glasses, ears, etc. Hence, this sets a clear precedent that wearable devices should be designed as part of clothing or as something that could be worn on a wrist for easy access.

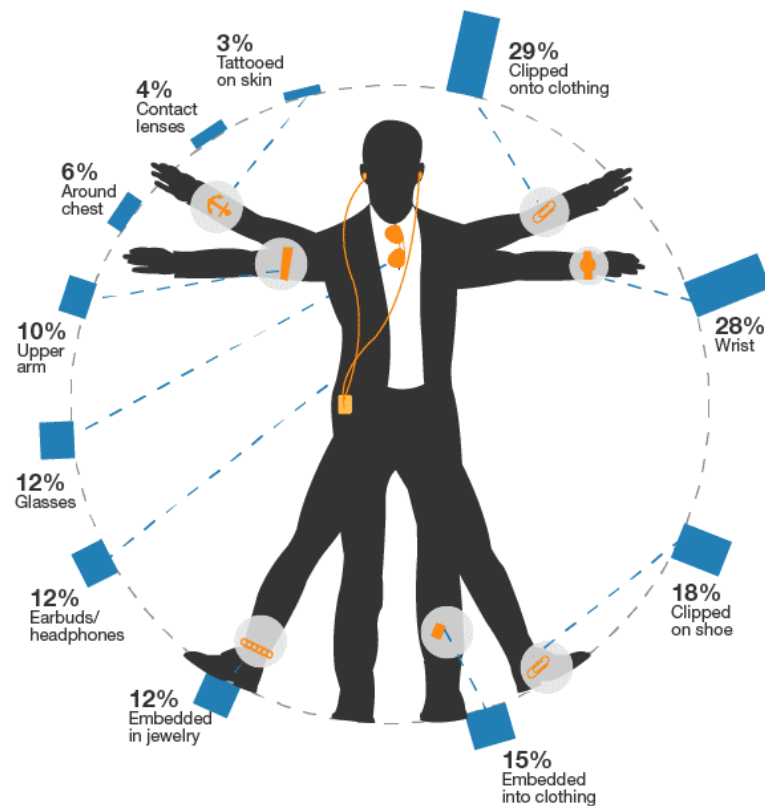


Figure 2.1. An infographic of a consumer survey report that highlights acceptance of the form factor of wearable devices. Source: [10][11]

The demographic classification of the user population may affect the acceptance of new technology based on its ease of use. For example, younger users may be more accepting of a new product introduction rather than older populations. In a survey[10], a staggering 32% of new users of age 25-24 and 24% of new users of age 15-24 had purchased a wearable in the last 3 months from the date of the survey. Moreover, beyond the purchase of a wearable device, the users saw an increase in their fitness and wellness which can be termed as an experienced user category. In this scenario, the most prominent age group to have fully integrated a wearable device was the age group 35-44. Hence this showed that people are more willing to accept a wearable device into their routine to move away from a sedentary lifestyle.

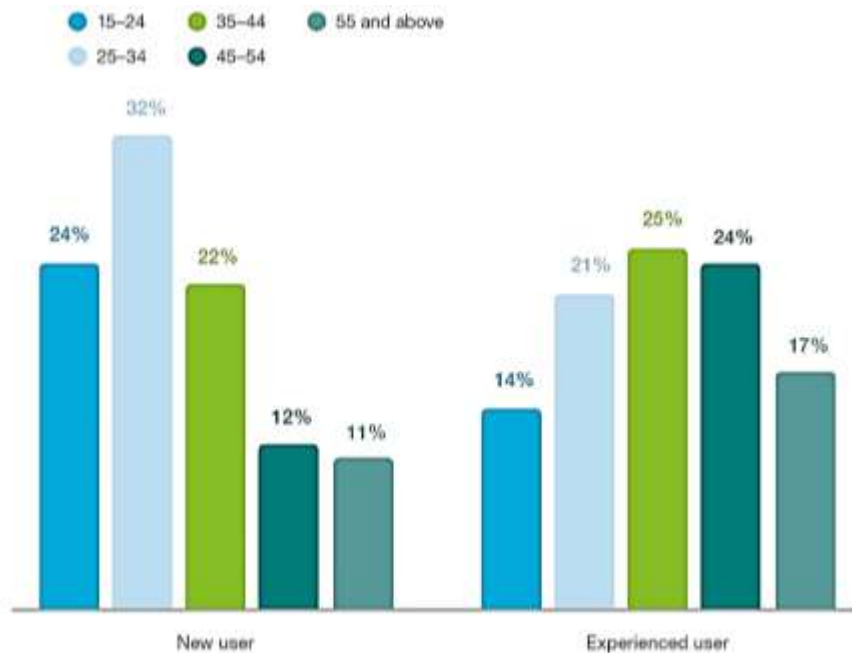


Figure 2.2. Acceptance percentage of a new wearable device among new users versus experienced users in a survey. Source: [10]

The above analysis shows how well wearable devices integrate into the user's lifestyle; however, it is also important to understand the reason why users may abandon wearable devices. Among the

people to abandon the wearable they purchased, the primary reason was the limited functionality of the device they purchased (21%), followed by the devices being not standalone (14%) and no LTE connectivity (9%). Other users rated inaccurate data (9%), poor phone integration (9%), low battery life (8%), poor design (6%), etc. Hence, the feedback provided by the survey[10] raises important questions in the direction of how wearable devices can be made better and easier to use, especially among the user population that may face challenges in integrating them into their daily lives.

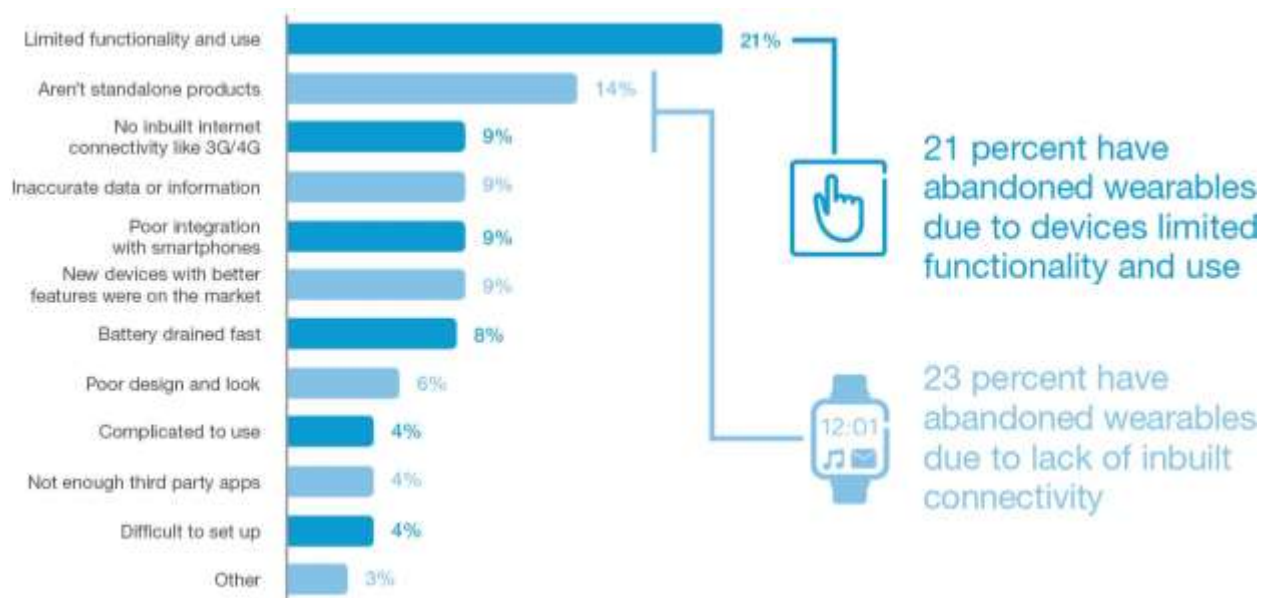


Figure 2.3. Major reasons cited in a survey as to why a user chose to abandon a wearable device. Source: [10]

2.2 Anatomy of a wearable device

A wearable device comprises an electronic circuit that is capable of recording and reporting various measures of human health and wellness. Thus, it is equipped in a manner that it can seamlessly integrate into the lifestyle of the user for recording this data. Wearable devices today are available

in small form factors, however, are powerful enough to measure, record and report data regarding sedentary or activity states of the user, heart rate, oxygen saturation, calories burnt for a specified activity, steps walked along with GPS pinpoints, speed of walking or running, etc. Hence, a well-designed electronic system is needed that enables all features mentioned above. The most generic system design approach in this scenario would be a central processor system that controls peripheral sensors to measure these physical signals and report them promptly. This processor would ensure that signals are sampled well above the Nyquist rate of information collection to ensure the recorded signal captures the true change of the physical quantity. A potential challenge for this scenario would be maintaining a low battery consumption to make the device last longer on a single charge.

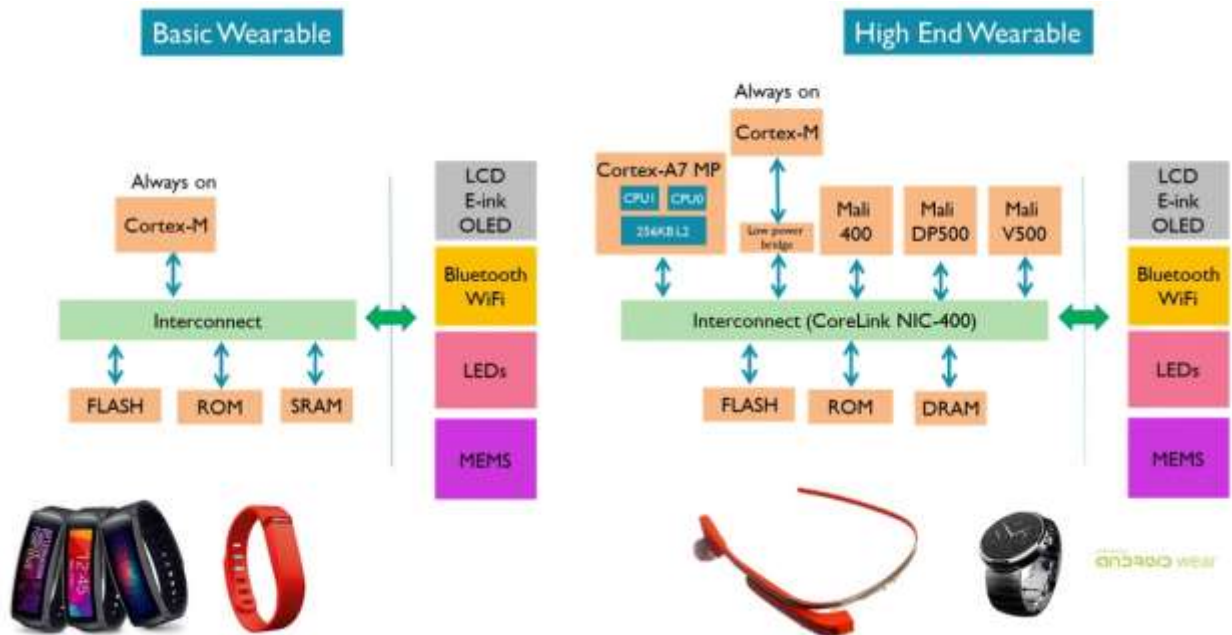


Figure 2.4. Classification of wearable devices into basic versus the high end. Source: [12]

A basic classification of wearable devices can be done into the basic or high end. A basic wearable device consists of minimalistic peripheral blocks to achieve rudimentary fitness goals. These goals

are primarily walking and running step count, activity and sleep detection, heart rate monitoring, and display. A high-end wearable device consists of the same peripherals as a basic wearable fitness band; however, more features may be added to it that may not necessarily align with one's fitness goals and may be more aligned with added functionality. Figure 2.4 shows the basic difference between a basic versus a high-end wearable device, clearly with more blocks and always-on processing capability. One can understand the balance of available peripherals versus the battery life using some of the commercially available wearable device architectures is discussed below.

Figure 2.5 shows an image of a teardown of a Microsoft® Band 2, which is an example of a basic wearable device. The dissection of the device shows two batteries interconnected to a central processing board via flexible printed circuit (FPC) substrates. The screen is on the other side of the motherboard, hence not seen. The motherboard also supports a heart rate and oxygen saturation measurement front end, which is a combination of an LED and a photosensor. The reported battery life for this device is 48 hours, hence a clear indicator of power optimization issues against the two batteries seen in the image.

Figure 2.6 shows an image of the Huawei® Watch 3, which is an example of a high-end wearable device in a round form factor. The dissection of the device revealed multiple boards to incorporate auxiliary circuitry, however, the main battery and the main processor system lie on one of the boards as shown. This wearable features a subthreshold processor[13] system, which has a lower active current in the μA range, thus, even in inactive modes, this wearable would perform better than the former. In addition, even though this wearable has a color touchscreen since the active current is already significantly reduced, this would not cause higher battery consumption and reports 1-

week battery life. Hence, having an advantage in processor technology may prove to be beneficial while designing a wearable device rather than strictly connecting more batteries. Moreover, the reported 1-week battery life relies on the fact that only certain peripherals are turned on, e.g. SpO₂, normal motion with 3 high-intensity workouts per week, and 50 message alerts per week. Hence, the amount of data recorded may also affect the battery life irrespective of good battery optimization or processor and/or auxiliary circuit technology used.

Going higher into the high-end wearable products, Figure 2.7 shows the motherboard for a FitBit[®] Sense with 1-week battery life. This wearable is also supported by a motherboard, with a touchscreen, SpO₂ sensors, GPS, and always-on notifications. However, one additional feature that can be seen in this dissection is an external flash engine that helps record more data over time. External flash memory has two additional advantages: data retention over power cycles and a lesser need to synchronize health data from the device to the phone. Hence, this wearable seems more aligned with a user's need with minimal synchronization needs.

Figure 2.8 shows a dissection for Apple[®] Watch Series 6, which is designed for a 1-day battery life with motion sensing, heart rate, and SpO₂, FDA-approved ECG[14], altitude sensor, compass, VO₂max, GPS, WiFi, BLE, NFC, and LTE with eSim technology. Even though this wearable has poor battery life, it provides better hardware integration into one system-in-package system (SiP) for less hardware circuit complexity, meaning most required system blocks may be laid down on one silicon. It also provides better user interaction in terms of mobile connectivity, mobile-less connectivity, data recording accuracy, fitness notifications, and medical value by detecting A-fib and sleep apnea. Hence, at the cost of battery life, one may create a wearable device that may be able to provide more user interactivity, measurement accuracy, and wellness-centric feedback.

Thus, the lifestyle of the user dominates which wearable may be useful, however, the ideal design principles of high battery life and good measurement accuracy and interactivity still stand.



Figure 2.5. Teardown of a Microsoft® Band. The PPG sensor and the board are in the center of the band, whereas 2 batteries are integrated into the band body[15].



Figure 2.6. A motherboard of the Huawei® Watch 3 centered around Ambiq Apollo® 4 ARM® processor with an active current of $4\mu\text{A}/\text{MHz}$. The recess above the processor is for the battery, whereas auxiliary circuits are on the other side of the board (not shown)[16].



Figure 2.7. A motherboard of the Fitbit® Sense with a Mediatek® GPS SoC, Kingston® external flash memory, USI® BLE module, and FitBit® application SoC. Auxiliary sensors are on the other side of this board (not shown)[17].

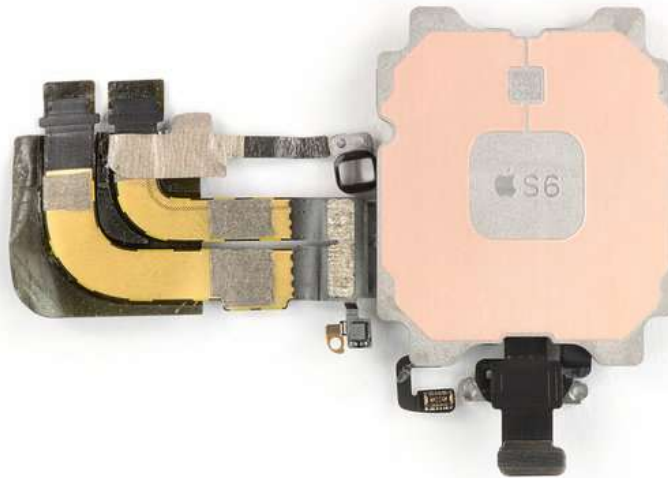


Figure 2.8. Teardown of a variant of Apple® Watch Series 6 with the S6 system-in-package (SiP) with connectors allowing access for auxiliary circuits (power, wireless communication) to interface (not shown)[18].

2.3 Classification of sensing mechanisms

The terms ‘sensor’ and ‘transducer’ are used interchangeably in the system design space, however, there is a fundamental difference in the expression of the output signal. A sensing mechanism expresses its output in terms of its inherent physical properties. A transducing mechanism translates the change in a property to be sensed into readable, meaningful data.

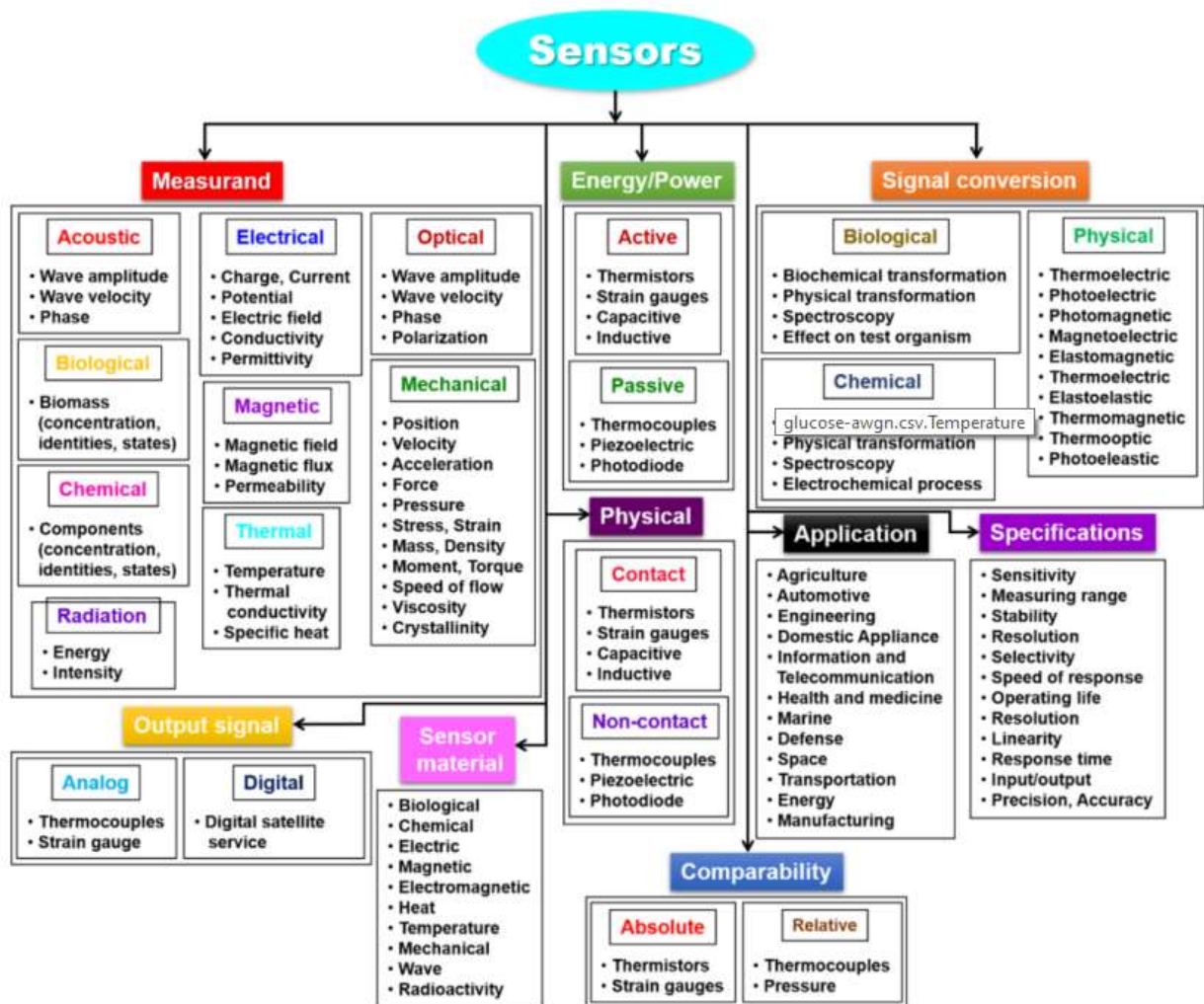


Figure 2.9. Classification of sensing mechanisms in mainstream use. Source: [19]

Hence a sensor pairs better with a detecting system, whereas a transducer is more so a translation system. The method of some of the biological signals is shown in Figure 2.9, which ranges from a variety of physical quantities such as magnetic, electrical, mechanical, optical, etc.

A biosensor is an analytical device, which converts a biological response into an electrical signal. It consists of two main components: a bioreceptor or biorecognition element, which recognizes the target analyte, and a transducer, for converting the recognition event into a measurable electrical signal[20]. A bioreceptor can be a microorganism, cell, enzyme, antibody, etc. and the transduction may be optical, electrochemical, thermometric, piezoelectric, magnetic, and micromechanical or combinations of one or more of the above techniques.

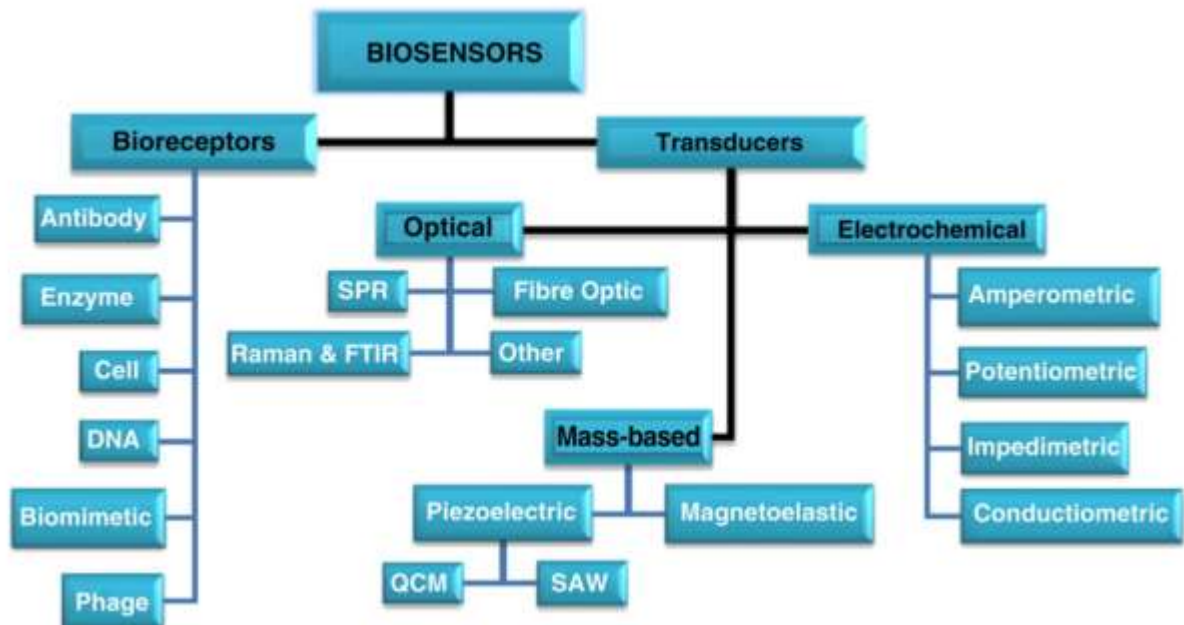


Figure 2.10. Classification of biosensors used in mainstream testing scenarios. This work focuses on the integration of impedimetric sensors. Source: [20]

Figure 2.11 shows a system-level diagram of a biosensor. The bioreceptor recognizes the target analyte and the corresponding biological responses are then converted into equivalent electrical

signals by the transducer. The amplifier in the biosensor responds to the small input signal from the transducer and delivers a large output signal that contains the essential waveform features of an input signal. The amplified signal is then processed by the signal processor where it can later be stored, displayed, and analyzed.

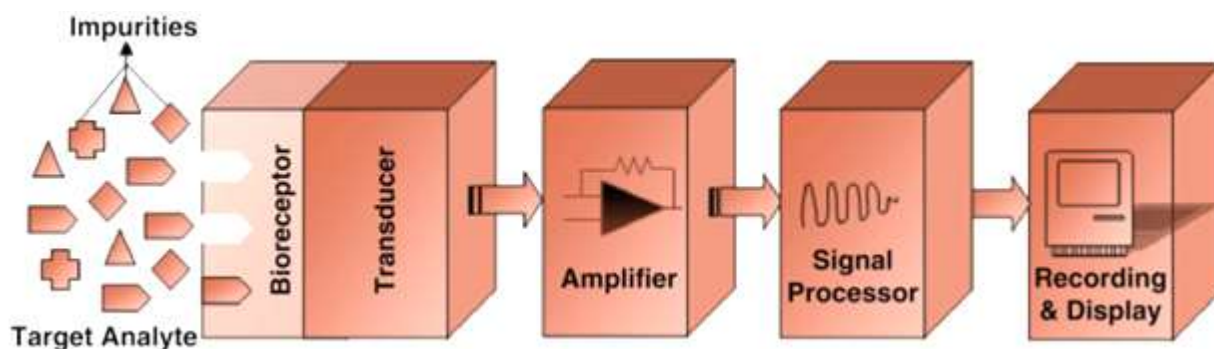


Figure 2.11. A generic signal flow for a biosensor system. Source: [20]

2.4 Types of electrochemical sensing techniques

An electrochemical sensing technique is a process of applying an electrical signal to obtain an electrical and/or chemical output. The applied electrical signal may vary in terms of amplitude in voltage, current, or frequency of the signal over time. A detailed overview of the commonly used technique and circuit design techniques are discussed in Figure 2.12.

2.4.1 Potentiometric sensing

Potentiometric biosensors measure the charge accumulated due to the analyte and bioreceptor interaction at the working electrode relative to the reference electrode under zero current. To transform a biochemical reaction into a potential signal, ion-selective electrodes, and ion-sensitive field-effect transistors are used[19], [21]–[23].

2.4.2 Amperometric sensing

Amperometric biosensors operate in two or three-electrode configurations. These sensors measure the current produced due to electrochemical oxidation or reduction of electroactive species at the working electrode when a constant potential is applied to the working electrode concerning the reference electrode. The current produced on the surface of the working electrode is proportional to the concentration of the analyte present in the solution[19], [21]–[23]. Compared with potentiometric biosensors, this method allows sensitive, fast, precise, and linear response, which makes it more suitable for mass production. However, poor selectivity and interferences from other electroactive substances are the disadvantages of these sensors [19], [24].

2.4.3 Conductometric sensing

Conductometric biosensors: Conductometric biosensors quantify the change in the conductance between the pair of electrodes because of an electrochemical reaction (change in conductivity properties of the analyte). Conductometric and impedimetric biosensors are usually used to monitor metabolic processes in living biological systems[19], [21].

2.4.4 Impedimetric sensing

Impedimetric biosensors measure the electrical impedance produced at the electrode/electrolyte interface when a small sinusoidal excitation signal is applied. It involves the application of low amplitude AC voltage at the sensor electrode and then the in/out-of-phase current response is measured as a function of frequency using an impedance analyzer[19], [21], [25]. This technique is also known as Electrochemical Impedance Spectroscopy (EIS). This work will discuss in

expand an integration of a sweat-based impedance biosensor; hence the concept of impedance measurement and collateral circuit design schemes are discussed in subsequent sections.

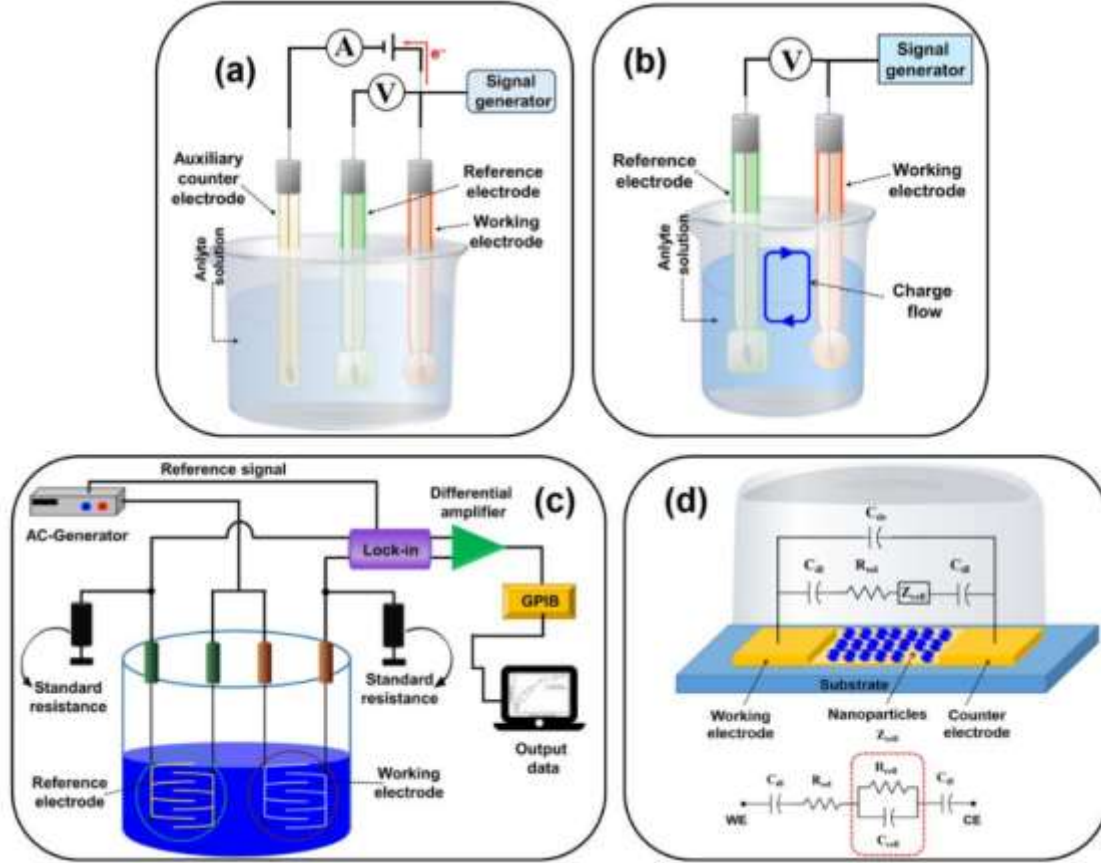


Figure 2.12. A comparison of schematics for commonly used electrochemical sensing techniques such as (A) Amperometric/voltametric (B) potentiometric (C) conductometric and (D) impedimetric biosensors. Source: [19]

2.5 Concept of impedance

The theoretical equation for measuring impedance is as shown in Eqn. 2.1.

$$Z(\theta) = \frac{V(\omega t)}{I(\omega t \pm \theta)} = \text{Re}(Z) + j \times \text{Im}(Z) \quad (2.1)$$

$$Z(\theta) = Z \cos \theta + j Z \sin \theta \quad (2.2)$$

This equation gives some information about a generic impedance measurement process as listed below. If the excitation voltage is constant, the variation in the amplitude and phase of the current will manifest as an impedance. If there is no variation in phase, the impedance is truly the resistance of the system. The measurement of impedance will need a measurement of both magnitude and phase of the measured voltage and current of the DUT. Based on the deductions made above, two prominent, conventional methods viz. zero-crossing detection and Lissajous patterns were devised previously to make such measurements and are discussed in the latter subsections. However, the challenge still stands to design such a system for low current consumption in a small form factor, preferably with minimal hardware components.

2.6 Types of impedance measurement techniques

Resistance measurement can be performed in the most rudimentary method by measuring the voltage applied to the load and dividing it by the current flow measured through the load.

However, impedance being a complex number will have time components associated with it, the reason being the use of a sine wave excitation voltage used to measure corresponding current and impedance. Moreover, the existence of energy-storing components such as inductors and capacitors introduce a time lag or lead in the current signal. Hence, using these properties of circuits in mind with linear time-invariant behavior assumptions, the following impedance measurements can be used.

2.6.1 Zero crossing detector

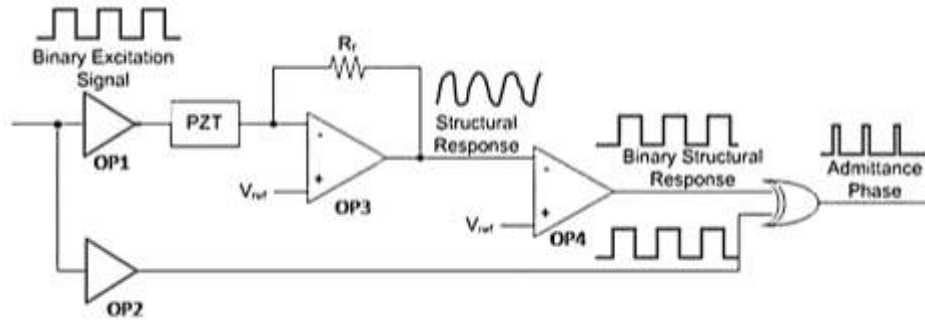


Figure 2.13. A phase measurement circuit for a piezoelectric transducer using a threshold detector and an XOR gate, reprinted from [26].

A zero-crossing detector is a circuit that detects when a signal amplitude crosses zero or a reference voltage. The output of this system depends on the fact that if there is a non-zero, non-negative voltage signal used to excite a load, there will be a current signal with some lead or lag, which can be compared. The method of comparison is usually an XOR operation, wherein the rising edges of a comparator output are compared for the delay, it may be represented as a high output. Figure 2.13 shows a simplified circuit diagram for phase measurement. A rectangular pulse train $V_{in}(t)$ is buffered by an operational amplifier (opamp) and applied to an impedance, in this case, a piezo transducer. The output of opamp OP3 is the current through the load, which is delayed in time by a certain amount. The reference voltage V_{ref} shifts the DC level of the applied input voltage, and it is set to one-half of the peak-to-peak voltage of input signal $V_{in}(t)$. OP4 is a comparator, which shapes the current waveform into digital. The XOR gate detects the difference between the input voltage and the current through the load. OP1 is necessary to drive a highly capacitive PZT, and OP2 is added to delay the excitation signal by the same amount as OP1 [26]. A potential advantage of using this scheme is that the phase can be obtained using the minimum number of components, without digital assistance. Moreover, a similar circuit can be used to evaluate magnitude by an

appropriately designed I-V converter using one opamp. This accounts for the simplicity of design and low inherent power consumption. However, a potential disadvantage may be offsets introduced due to the opamps in the signal chain, which may need a good characterization effort, or digital assistance to correct this.

2.6.2 Lissajous patterns

Lissajous patterns are a method of comparison of two waveforms rather than making an absolute judgment about the period and phase offset of the measured waveform. Thus, instead of plotting two waveforms against a time axis, if a reference waveform is plotted against a measured waveform, then the resultant plot can be used to make some necessary assumptions regarding the properties of the measured waveform. Figure 2.14 shows how this plotting will give an output curve that can find the phase shift of the measured waveform assuming equal reference and measured voltage magnitudes. Figure 2.15 shows the change in the number of lobes for the change in the ratio of frequencies of the reference and measured waveforms.

Lissajous patterns give a two-dimensional output plot, thus it is easier to realize such plots on a paper plotter or an oscilloscope. The phase measurement in this case is highly accurate as the reference waveform may not be generated by the circuit. Thus, a true phase offset is received as an output when the voltage and current waveform are compared. This is better than the former zero-crossing detection technique as the noise effects cancel out on the output plot and does not require a true zero voltage to trigger the timer. However, the disadvantage is the difficulty in programming the interpretation of the Lissajous pattern as a program and the longer processing time in comparison to the zero-crossing detection technique when using digital assistance.

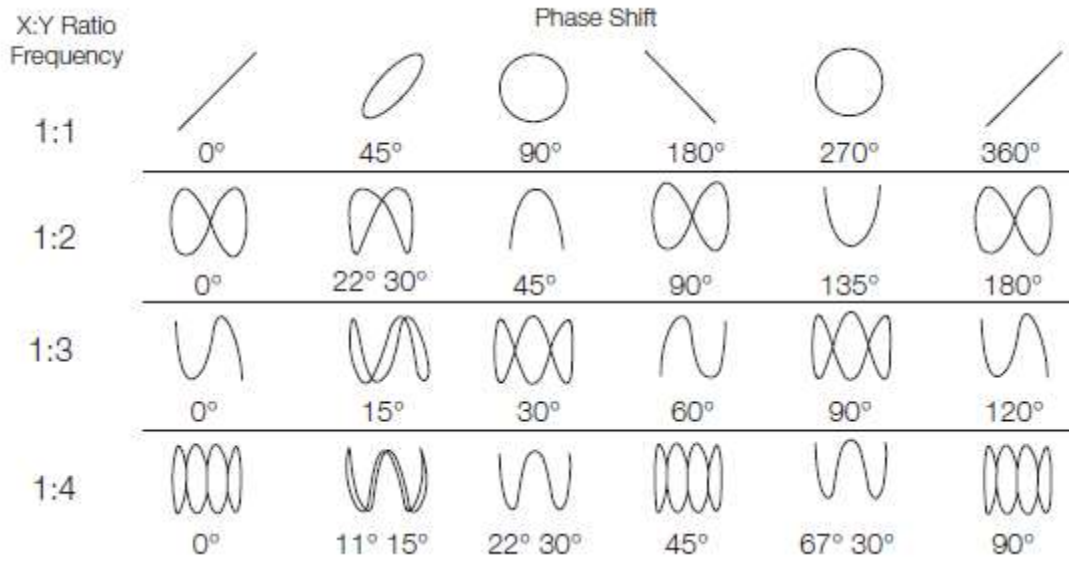


Figure 2.15. Output for a Lissajous pattern for variation of frequency and phase of one signal to the other.

2.7 Comprehensive digital assistance for impedance measurements

The process of impedance measurements can be done using the above methods; however, they offer their circuit-level offsets and errors due to distortion from analog blocks. Moreover, the measurement needs to be digitized using an ADC to store on processor memory for further data analysis. Hence, a method of digital impedance measurement would suit a modern application such as making wearable devices. The process of comprehensive digitization is discussed below.

2.7.1 Odd and even part of a signal

The definition of an even signal is one which is mirror-symmetric if $x(t) = x(-t)$, whereas for an odd signal, $x(t) = -x(-t)$ defines antisymmetric nature of a waveform. This can be observed from the example given below. The sine function is the most simplistic odd function whereas the cosine

function is the most simplistic even function. Thus, if provided with an arbitrary input signal, one can segregate a signal into two output functions, namely an odd and even function.

2.7.2 Extraction of odd and even parts

If we have a signal $x(t)$, then by applying a Fourier transform on this signal, we can obtain a sum of its odd and even parts as shown below.

$$X(f) = \mathcal{F}[x(t)] = \int_{-\infty}^{\infty} [x_r(t) + jx_i(t)]e^{-j2\pi ft} dt \quad (2.3)$$

$$= \int_{-\infty}^{\infty} [x_r(t) + jx_i(t)][\cos(2\pi ft) - j \sin(2\pi ft)] dt \quad (2.4)$$

$$= \int_{-\infty}^{\infty} x_r(t) \cos(2\pi ft) dt + \int_{-\infty}^{\infty} x_i(t) \sin(2\pi ft) dt \quad (2.5)$$

$$+ j \left[\int_{-\infty}^{\infty} x_i(t) \cos(2\pi ft) dt - \int_{-\infty}^{\infty} x_r(t) \sin(2\pi ft) dt \right]$$

$$= [X_{re}(f) + X_{ro}(f)] + j[X_{ie}(f) + X_{io}(f)] \quad (2.6)$$

$$= X_r(f) + jX_i(f) \quad (2.7)$$

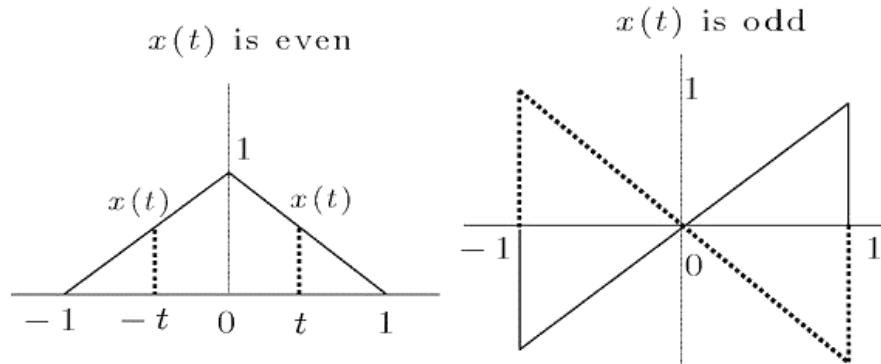


Figure 2.16. Comparison of an even versus an odd function.

With further simplification, one can derive that the even and odd signal manifests from the original signal by manipulating it along with its mirror image.

$$f_e(n) \triangleq \frac{f(n) + f(-n)}{2} \quad (2.8)$$

$$f_o(n) \triangleq \frac{f(n) - f(-n)}{2} \quad (2.9)$$

The advantage of this decomposition is the output being purely odd and even functions, which can be correlated to being imaginary and real values of a measured input function. Thus, the real and imaginary parts of an input signal can be obtained directly, which can be used to calculate the magnitude and phase of the measured signal.

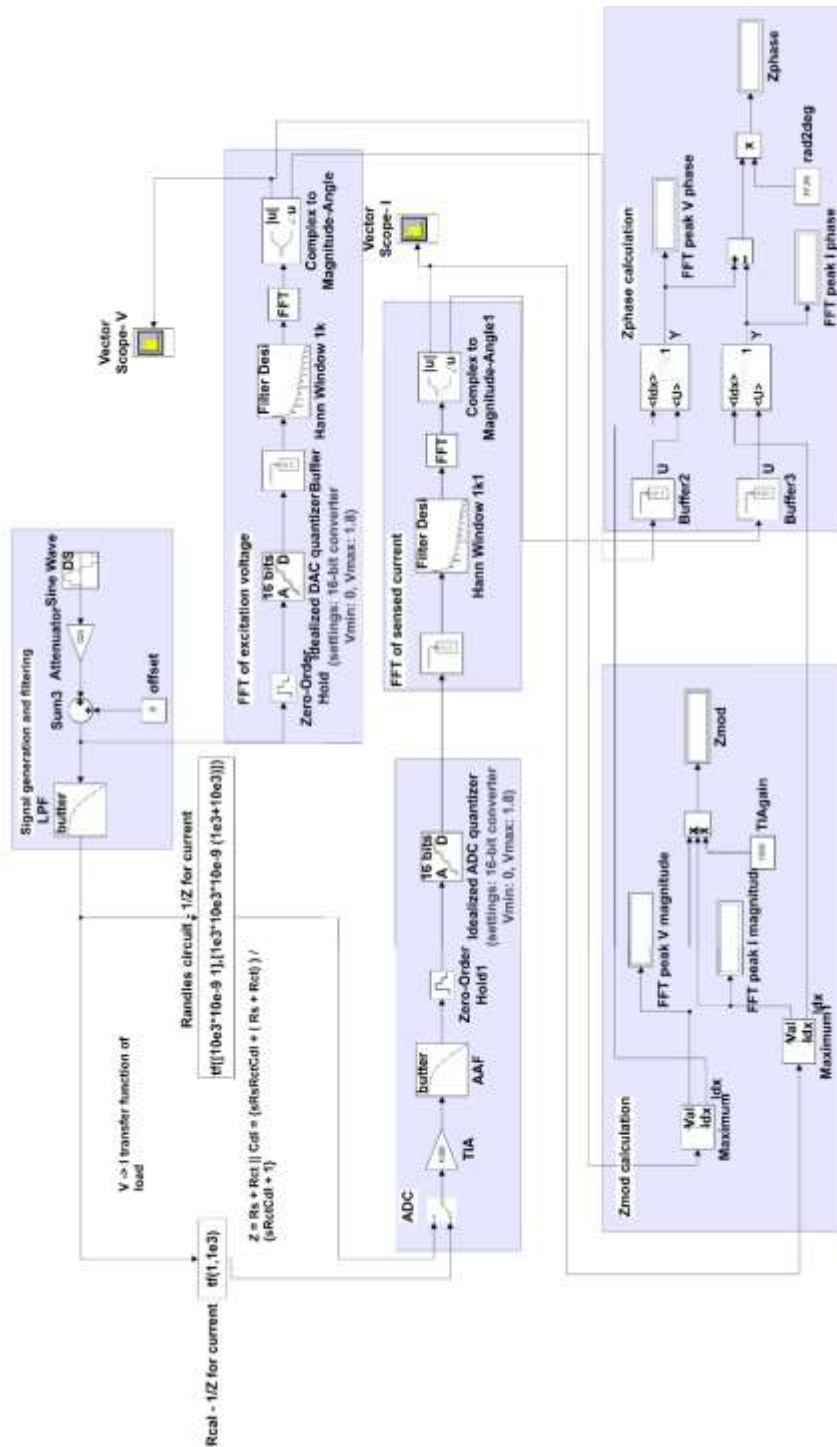
2.7.3 Simulation-based verification

The simulation of the impedance measurement system depends on two facts: measurement of the current passing through the impedance as accurately as possible; and splitting of the real and imaginary part of the signal to represent the real and imaginary part of the impedance. The current sensing mechanism can be implemented in a circuit using an I-V converter.

$$I_{in} = \frac{V_{out}}{R} \quad (2.10)$$

It can be assumed that the voltage waveform is tapped from the generator and the current waveform is tapped from an I-V amplifier and sampled using an ADC. An instrumentation amplifier can be used to subtract these two waveforms to obtain an analog signal that has phase offset and magnitude ratio data. This output waveform is processed by the Fourier transform method in the discrete domain due to the ease of digital implementation. The digital implementation is simplistic: it takes in all the samples, mirrors them simultaneously, and gives out an odd and even value, which is also an imaginary value and real value of the impedance of the load. This implementation is different for the fact that the ADC is preceded by an instrumentation filter for a true comparison

of voltage and current waveforms[28]. Based on these, an ideal model was tested in MATLAB® Simulink as shown in Figure 2.17. A MATLAB® Simulink model of the FFT-based impedance measurement system using a conductance transfer function for resistance and Randle's circuit. Figure 2.17.



CHAPTER 3

DESIGN AND VALIDATION OF THE PROPOSED WEARABLE DEVICE

3.1 Sensors and wearables for diabetes

Diabetes is an endocrine disorder of the pancreas, which is the inability to process sugar taken in as food. As shown in the WHO infographic, roughly 422 million adults worldwide are affected by diabetes, which is 1 in 11 people. Types of diabetes are type 1 where glucose levels drop drastically. Type 2 diabetes creates elevated glucose levels. We will highly focus on the detection of type 2 diabetes for this presentation. Elevated glucose levels lead to other complications such as heart attack, renal failure, gangrene and amputation, blindness, and brain stroke. This in turn also has various financial implications on the patients which include insulin administration and other drugs and in many cases loss of ability to work due to amputation. Alone in the US, 26 million patients have diabetes, among which 7 million are unaware of their condition. Undiagnosed diabetes is more dangerous as the resulting complications could have been prevented by proper diagnosis and treatment in its early stages. Thus, there is a need to create a wearable device that can sense elevated glucose levels.

3.1.1 Evolution of the glucose biosensor

The glucose enzyme electrode was proposed by Clark and Lyons[29] in 1962. Their device relied on the entrapment of the enzyme GOx over an amperometric oxygen electrode that monitored the oxygen consumed by the biocatalytic reaction. Biosensors gained popularity during the 1980s, reflecting the growing emphasis on biotech. New biosensor transduction principles were

introduced during this decade, including fiber-optic and mass-sensitive (piezoelectric) devices[30]–[36].

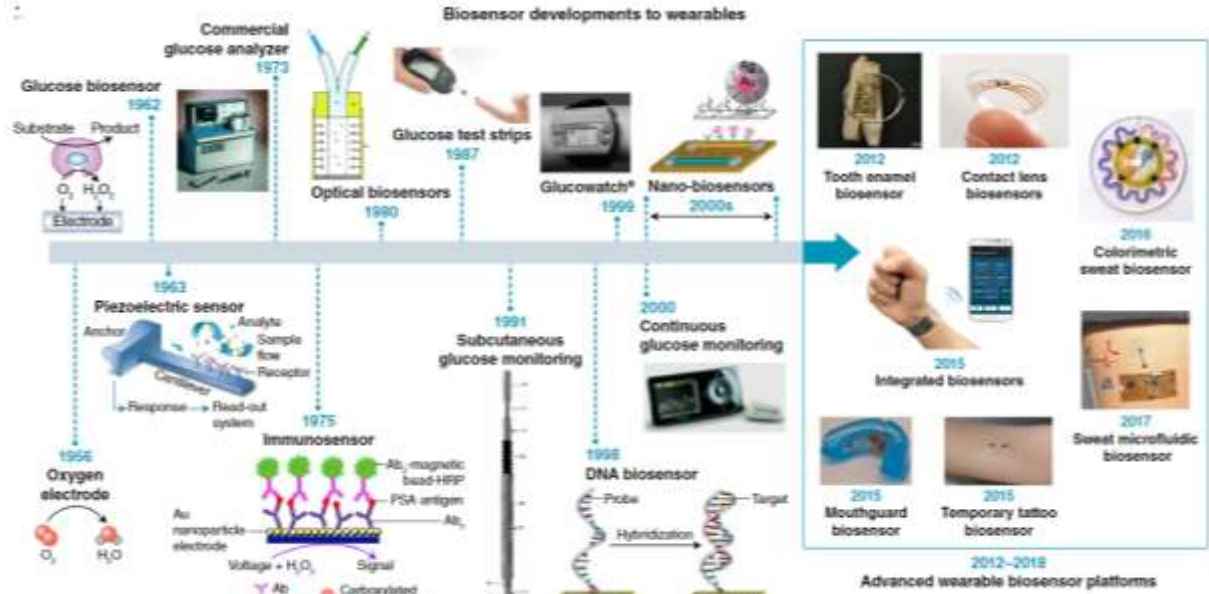


Figure 3.1. Evolution of glucose biosensors over the last century. Source [36]

Considerable efforts during the 1980s led also to the introduction of commercial self-testing blood glucose strips that used mediator-based enzyme electrodes[36]–[38]. Subsequent activity during the 1990s resulted in subcutaneously implantable needle-type electrodes for real-time in vivo glucose monitoring[36], [39]. These subcutaneously implantable glucose sensors moved in the early 2000s to commercial continuous glucose monitors that track in real-time the glucose level in the ISF, along with diabetes-relevant trends and patterns[36], [40], [41]. The emergence of nanotechnology in the late 1990s has led to a variety of nanomaterial-based biosensors exploiting the attractive properties of different nanomaterials, such as silicon nanowires and gold nanoparticles, for label-free or amplified biosensing, respectively[36], [42], [43]. The specific base-pair recognition of DNA sequences led to the development of different DNA biosensors in

the late 1990s[36], [44]–[46]. Such nucleic acid sensors are playing a growing role in genomic sequence analysis. These advances in biosensor technology over the past five decades paved the way for modern wearable biosensors.

3.1.2 Contemporary clinical and wearable glucose-sensing technology

Glucose level sensing by clinically acceptable methods includes 2 major methods: a lab-based sample collection and testing versus a portable glucometer system. For a lab-based approach, a venous blood sample is taken pre and post-fasting, which is a fasting glucose testing methodology.

Table 3.1. Comparison of prevalent glucose level measurements.






Test method	 Lab-based testing	 Portable glucometer
Test turn in time	Fasting plasma glucose = few hours HbA1c = every 2-3 months	1-2 minutes before and after a meal
Basis of testing	Dye or optical techniques	Electrochemical measurement
Professional help	Required	Not required
Invasive	Yes	Yes

Table 3.2. Comparison of commercial continuous glucose monitoring devices.

Commercial device	 Dexcom™ G5 CGM	 Freestyle™ Libre	 GlucoWise™
Sensor sample	Interstitial fluid	Interstitial fluid	Skin proximity
Sensing technique	Chronoamperometry	Chronoamperometry	RF-based dielectric (65GHz)
Data recording	Smartwatch, smartphone	Dedicated recorder	Smartphone
Continuous glucose measurement (CGM)	Yes	Yes	No
Invasive	Yes	Yes	No

For long-term cumulative analysis of the glucose levels of a patient, one may rely on the Hb-A1c methodology, which relies on the detection of glycosylated hemoglobin, formed because of extended exposure of hemoglobin to glucose. Contrary to being a gold standard, some studies do suggest that Hb-A1c may not be able to provide information on glucose trends and excursions and variation in diurnal patterns of the patient[47], [48]. While lab-testing may require professional help, a portable glucometer and lancet can be used by a patient directly to sample their blood glucose level using blood samples from the index finger.

Continuous glucose monitoring (CGM) systems have evolved because of a need for accurately measuring glucose levels on-demand and providing better glycemic management and quality of life[47]. Users reported better user satisfaction and reduced fear of hypoglycemia since CGM systems allow easy and quick identification of dysglycaemia[47], [49]–[52]. Such a system also aids the user in understanding the impact of food and exercise on glucose management, enabling short-term planning such as mealtime adjustment and reducing exercise to prevent dysglycaemia[47], [49]–[52]. However, CGM systems rely on an amperometric interstitial fluid sensor and lancet, that must remain embedded in the skin of the user for extended periods to measure glucose levels. Hence, there is great value to improving the quality of life of the user by providing a wearable solution that is lancet-free and provides the same features and advantages as a CGM system.

3.2 Design objectives of the proposed wearable device

The design objectives for the proposed wearable device can be listed below to set a pathway to integrating the glucose sweat biosensor. The wearable device

1. Is fully non-invasive

2. Has small form factor with minimal external hardware
3. Measure within 20% acceptable error
4. Accepts low sweat sample volume (1-5 μL)
5. Can be used by a sedentary or active user for a week

3.3 Analysis of lab instrument circuitry

In previous works that mention the design of the biosensor, EIS measurements taken by recording current flow using a potentiostat (Gamry Instruments, Warminster, PA, USA) after applying 10 mV AC voltage with a frequency sweep of 1 Hz to 1 kHz[53]. Hence, it would be valuable to understand a pre-existing implementation of a potentiostat and select the useful parts of the architecture for the wearable device. Figure 3.2 shows an ideal representation of the internal components of a potentiostat. As mentioned in the previous section, electrochemical biosensors work on various transduction of electrical signals such as voltage, current, impedance or conductance. These can be sensed using a multitude of circuits that are shown below.

Figure 3.3 shows the signal generation circuitry for the Gamry potentiostat, where there are three 16-bit DACs with 0.25mV bit resolution: DC bias control DAC, scan DAC and attenuation DAC. The DC bias control DAC's controls the DC bias point of the measurement in the $\pm 8\text{V}$ range, whereas the attenuation DAC is used to generate sine waves using direct digital synthesis (DDS) in the 1MHz to 1mHz range with an amplitude of 5.9V to 11 μV using gain control. All sine waves below 1mHz are generated using the scan DAC. In this work, only the DDS based attenuation DAC would be of value to support EIS measurements for the wearable device. Moreover, the 1 Hz - 1kHz range is apt for measuring glucose modulations for the biosensor.

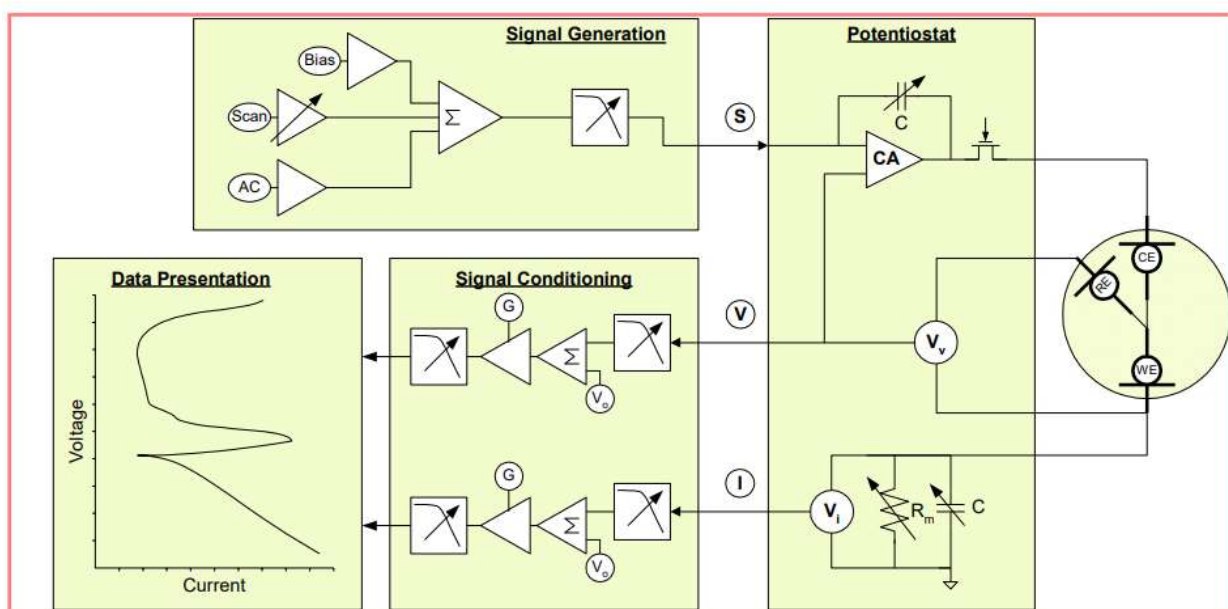


Figure 3.2. An ideal representation of a programmable potentiostat with necessary signal generation, excitation, sensing and signal conditioning blocks. Source: [54]

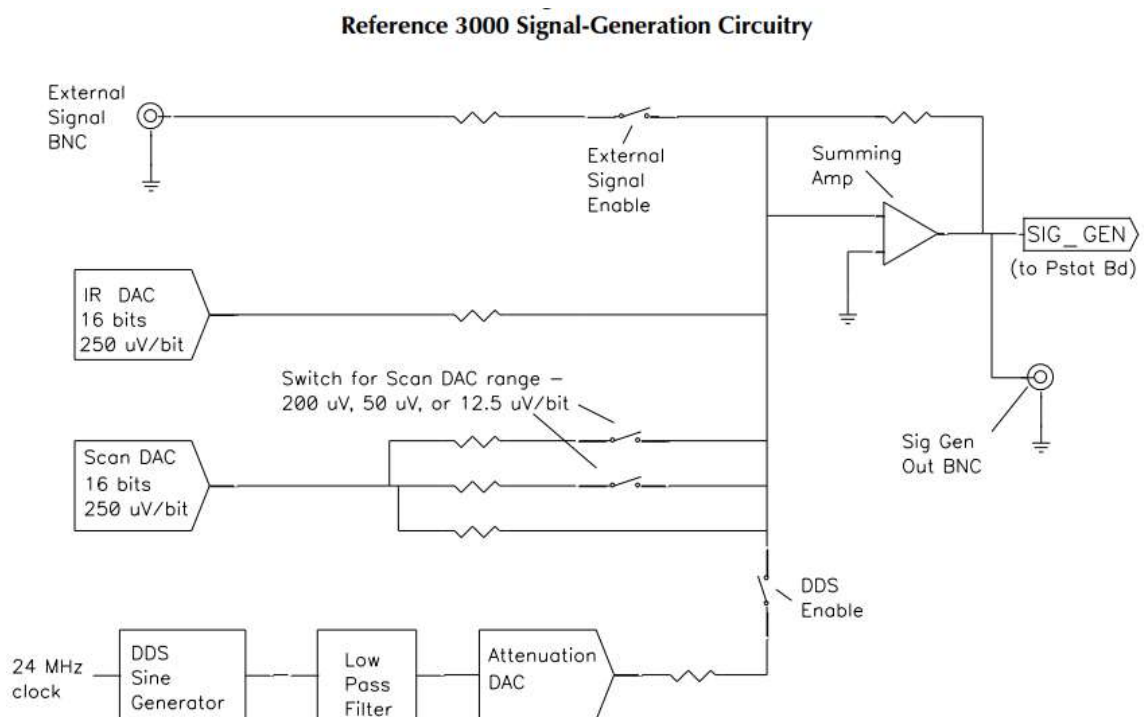


Figure 3.3. Signal generation architecture for the Gamry® Reference 3000. Source: [55]

Reference 3000 Potentiostat Board in Potentiostat Mode
Simplified Schematic/Block Diagram

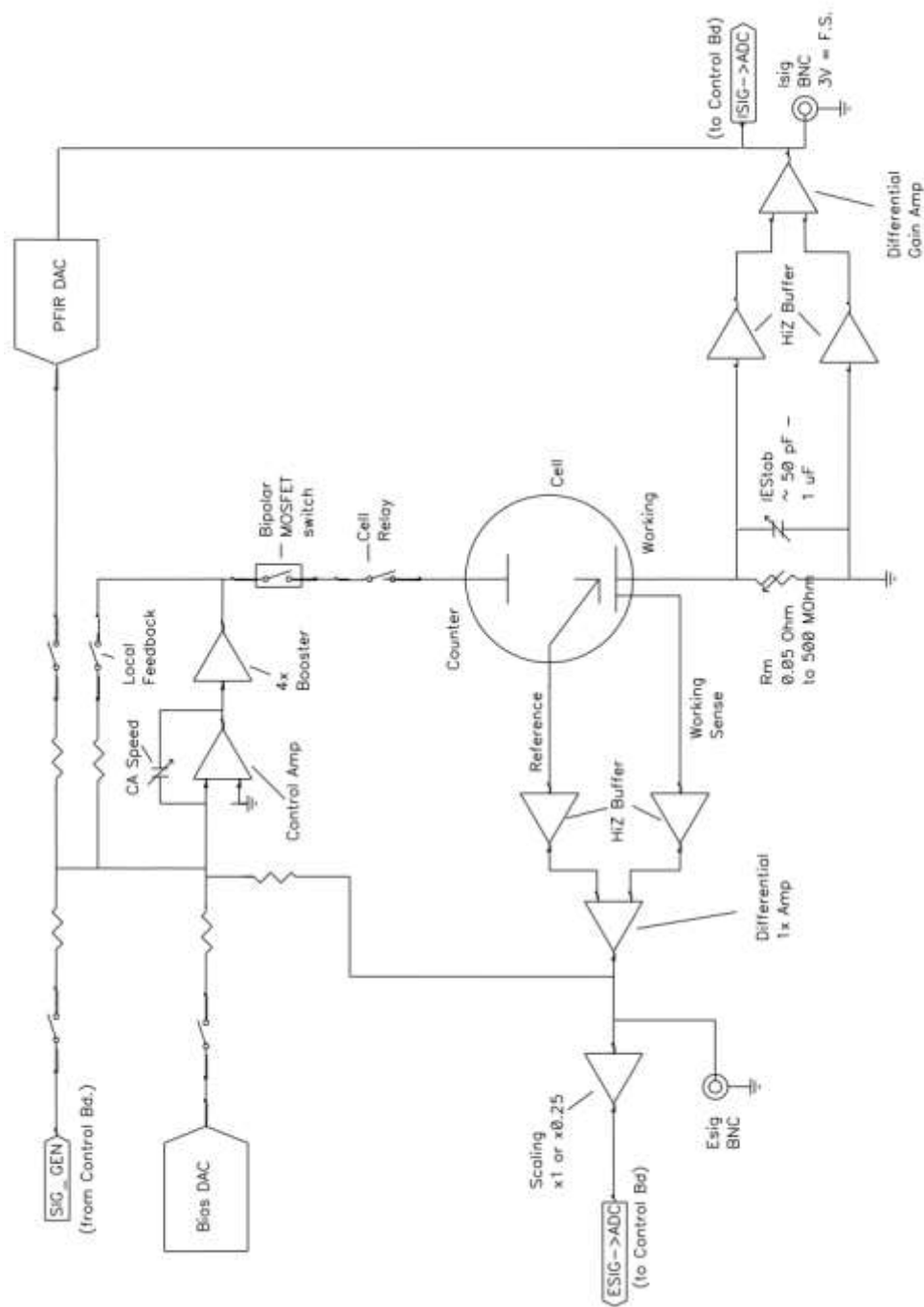


Figure 3.4. Electrochemical cell connection to the Gamry® Reference 3000. Source: [55]

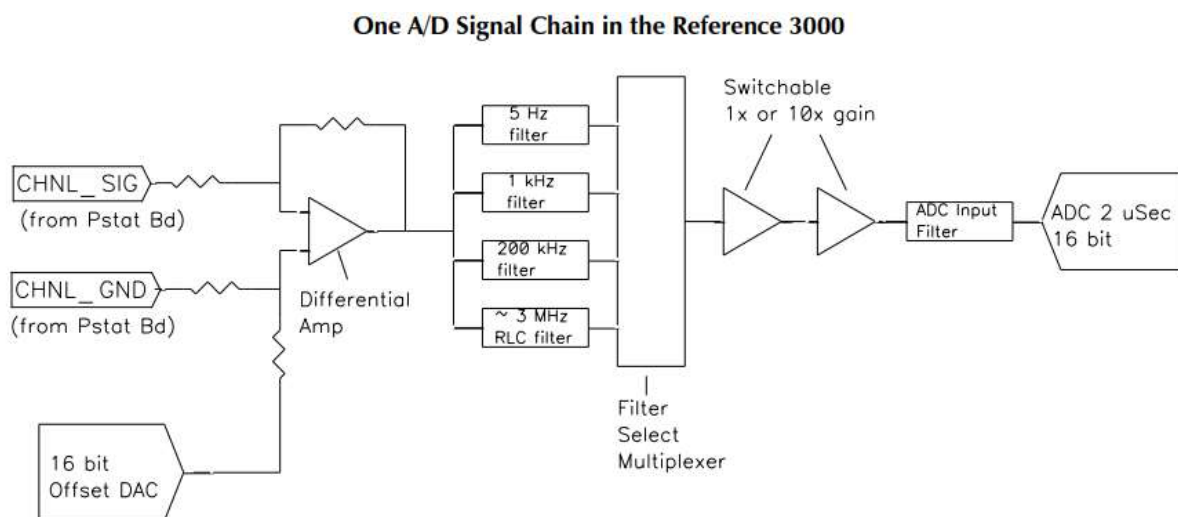


Figure 3.5. Voltage and current sensing ADC circuitry channel for the Gamry® Reference 3000. Source: [55]

Figure 3.4. shows the connections to an electrochemical cell in EIS mode. The measurement loop signal flow begins from the SIG_GEN node, which is supplied by the excitation circuitry in Figure 3.3. The signal is boosted as necessary using the 4x booster which operates in 2 ranges: ± 1.5 A at ± 30 V and ± 3 A at ± 15 V which helps current support measurement of electrochemical cells used in industry and academia. In this work, such a booster may not be necessary due to the low-voltage operation of the biosensor. This schematic also shows a 3-wire electrochemical cell with working, counter, and reference electrodes. However, in this work, a 2-wire biosensor is used, thus there may not be a need of an oversized voltage sense network for ESIG \rightarrow ADC. For the current sense mechanism, R_m is a set of 11 fixed-value decade resistors connected by a relay to change current sensing range from $50\text{m}\Omega$ to $500\text{ M}\Omega$. Moreover, this network is connected to an instrumentation amplifier which eliminates the need for good impedance matching to the load, as well as provides high gain, low offset and low drift. One may select one resistor instead of a decade resistor set as the impedance of the glucose biosensor is well-established[56]. Hence, a 2-wire

current sensor network with a fixed current sense resistor with an instrumentation amplifier is well-suited for the wearable device for minimal possible form factor.

Figure 3.5 shows the ADC sensing circuitry for the Gamry potentiostat. This potentiostat has three 16-bit ADCs. These channels are used to measure load current signal, load voltage in case using >2 wire connection, and system level signal checks respectively. All channels are activated simultaneously to measure voltage and current signals without inherent lag, ensuring good phase measuring accuracy. Each channel is provided with a multiplexed filter system with poles at 5 Hz, 1 kHz, and 200 kHz to support wide band impedance measurement. For a wearable biosensor system, multiple ADC channels may result in higher current consumption. Moreover, unlike lab equipment where cables may be longer and need compensation, the wearable will be small in form factor. Hence, there will not be a need to measure voltage in sync with current and programmatic values of generated V may be used digitally. Hence, one 16-bit ADC is sufficient for the current sensing system for the proposed wearable device.

3.4 Selection of measurement hardware

EIS measurements can be performed using a potentiostat; however, the method of measuring impedance can be based on the Lissajous pattern or discrete Fourier transform (DFT)[57]. In the case of the Lissajous pattern, two waveforms are divided, and their phase difference is calculated using XY plotting. This is a processor-intensive operation and can take a few seconds to yield results. Moreover, this will only allow one sensor to be connected to the potentiostat unless a multiplexer is used. To show larger throughput and least hardware requirement, a DFT-based time division multiplexed (TDM) sensor module has been used, wherein the measurement time was fixed to 13 ms and impedance measurement was performed on four sensors in quick succession.

3.5 System-level design methodology for proposed wearable device

The ADuCM350 (Analog Devices Inc., Norwood, MA) system-on-chip (SoC) is at the heart of the measurement setup. The system-level block diagram is shown in Figure 3.6. The SoC consists of a configurable analog front end (AFE), which consists of a wave generator, a switch matrix, and a 2048-point discrete Fourier transform-based impedance analyzer. The amplitude and frequency of the wave generator are fixed using digital words. The AFE is operated using a binary sequence, which controls wave generation, switching sensor channels, and evaluation impedance. The switch matrix enables time-division multiplexing of sensors with the instrumentation loop to measure each sensor. The process of TDM frequency measurement is as follows. The sequence of the instructions is sent to the AFE first-in-first-out (FIFO) buffer using direct memory access. This helps in achieving low power consumption, as the core processor is not turned on. The wave generator amplitude and frequency are set using respective binary words. Now, the switch matrix connects to a calibration resistor channel to measure the resistance of a precision resistor and uses it as a reference for subsequent measurements. The impedance analyzer block is formed by an I-V converter, analog-to-digital converter (ADC), and DFT engine. The current sensed is converted to a proportional voltage and a 2048-point DFT is performed on it. The real and imaginary parts of the data are converted to magnitude and phase. Two analog pins are selected from which one acts as a generator and the other as a sink. These pins are in turn connected to one of the sensors due to the switching action of the switch matrix. After a 13-ms DFT cycle on one sensor, the AFE switches to the next sensor channel. Thus, the impedance measurement is performed on all four sensors in a combinatorial sequence. Additional details of the circuit are shown in the appendix.

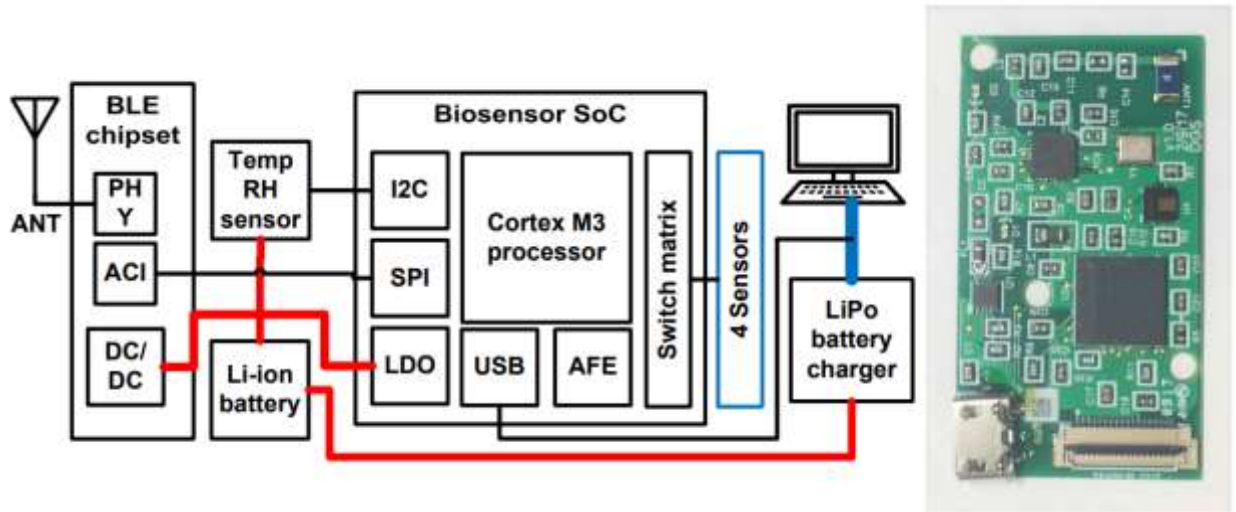


Figure 3.6. A system-level representation of the proposed FFT-based impedance measurement wearable device. Auxiliary circuits include Bluetooth Low Energy, LiPo battery management, and temperature + RH sensor.

3.6 Dry-load calibration

The proposed wearable device was tested for individual channel offset on the calibration channel of a universal dummy cell (Gamry Instruments) against a Gamry® Reference 3000 potentiostat. The dummy cell is shown in Figure 3.7, wherein the calibration side of the cell was used in 2-wire configuration by shorting the reference, counter, and counter sense terminals together on the sink end and working and working sense terminals on the source end. Figure 3.8 shows a Bode plot comparison of the measurements of the over 80-1000 Hz frequency of excitation at 10mVRMS. The 80 Hz limit was chosen based on the Nyquist limit of the 13 ms DFT block in the ADuCM350. For a 13ms processing block, a signal with frequency the inverse of 13 ms can be processed through the said block, which is ~ 80 Hz. However, if the Nyquist theorem is considered, a signal with at least 2×80 Hz will be captured with magnitude and phase information more correctly via this block. Thus, to verify the Nyquist limit, 80 Hz was chosen to understand the performance of

the ADuCM350 impedance measurement system. While no such limit exists for the Gamry® instrument due to low frequency sampling capability, the ADuCM350 shows a higher variation in measurement from 80 Hz to 200 Hz. Higher frequency performance is comparable for both the Gamry® and the ADuCM350 based wearable device. Hence, the accuracy of the device is comparable to the lab instrument.

Precision of both systems was compared by taking $n=800$ measurements of the same cell at 10mVRMS, 1 kHz excitation frequency. The standard deviation and average of all measurements are shown in this plot for both magnitude and phase of impedance. For both systems, the variation of the measurement is well within the 3 standard deviations, showing good reproducibility of the measured impedance magnitude and phase. A slightly quantized jitter is more prominent in the wearable device due to the DFT based impedance calculation, whereas in case of the Gamry®, the measurements are performed using Lissajous patterns. Hence, the variation of measurement is slightly lesser in the Gamry® instrument compared to the wearable device. Nonetheless, the wearable device performance is acceptable for further experimentation.

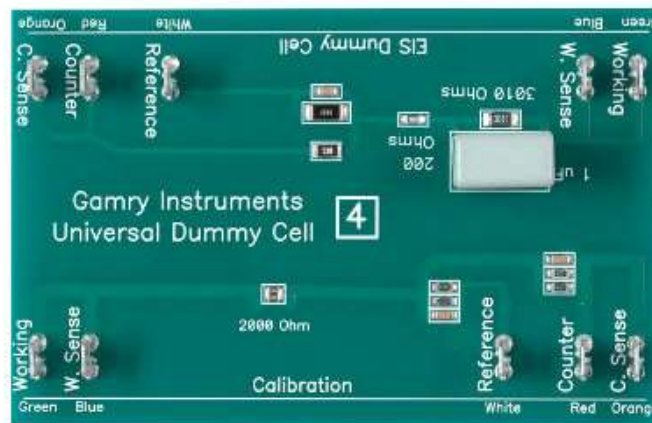


Figure 3.7. A universal dummy cell by Gamry Instruments®. All calibration experiments for this work were done using the side marked for calibration.

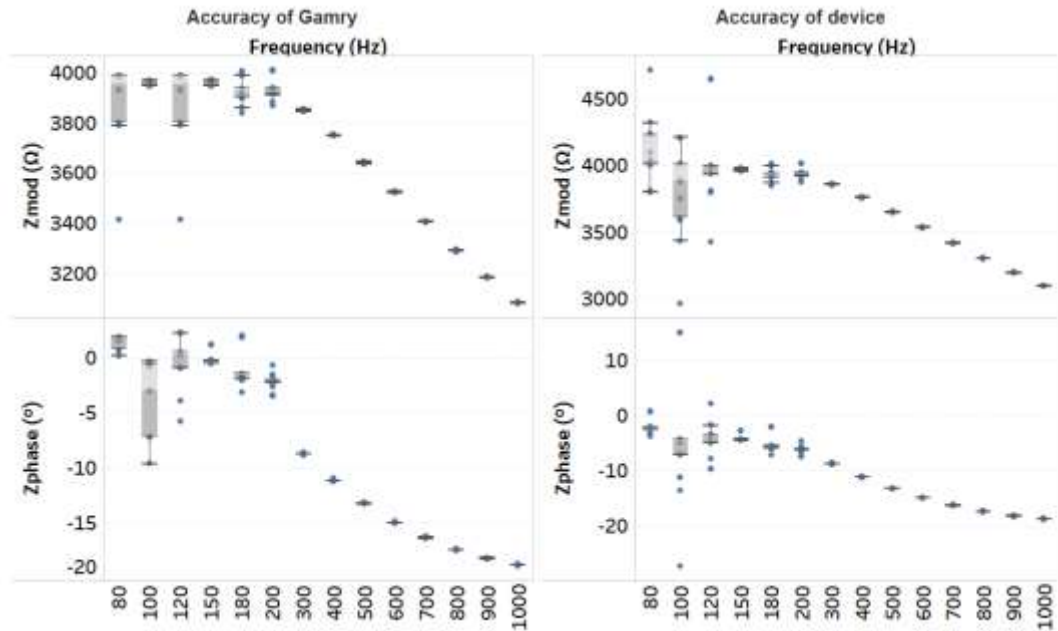


Figure 3.8. Comparison of measured accuracy for Gamry measured impedance values versus the wearable device for a universal load cell.

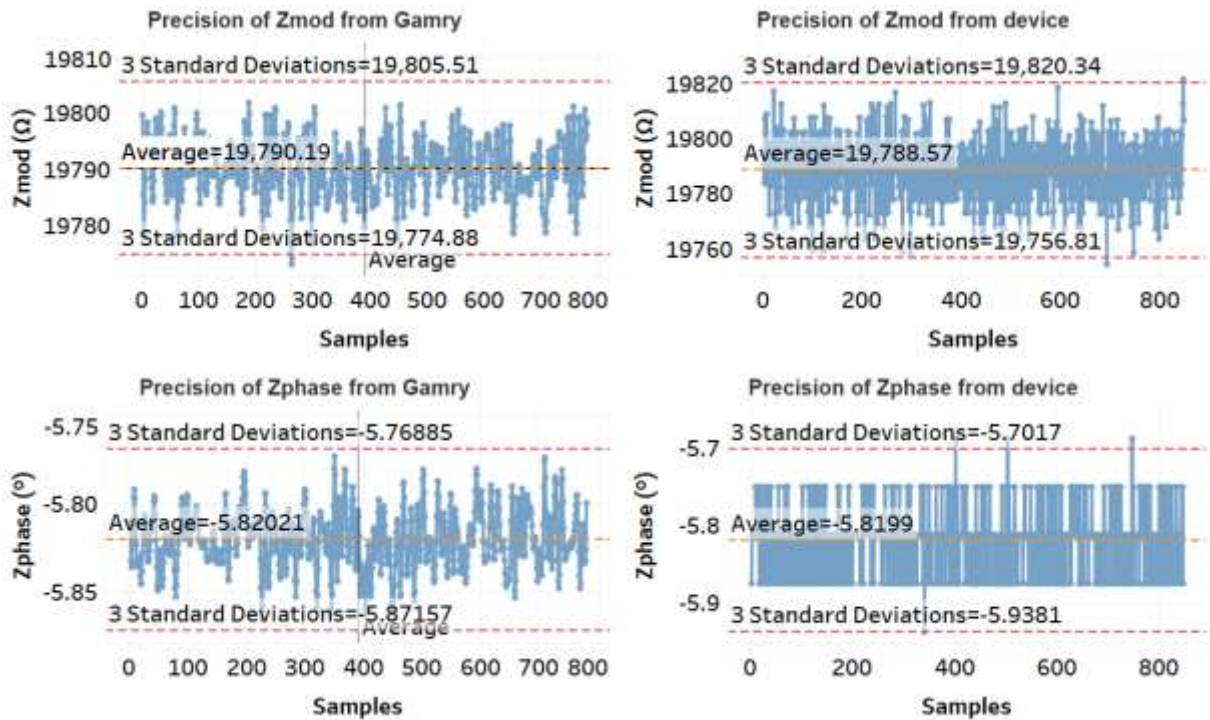


Figure 3.9. Comparison of measured precision for Gamry measured impedance values versus the wearable device for a universal load cell.

3.7 Calibration using control buffers

Glucose dose concentrations ranging from 5-200 mg/dL were made in synthetic sweat buffer with pH values 4, 6, and 8 were introduced on a functionalized sensor and the impedance at 100Hz was recorded to demonstrate proof of binding interaction on the sensor surface. Fig. 3a shows the response of the system as the standard error of the mean of the percentage change function of impedance to varying pH and dose concentrations with a linear fit. Eqn. 1 shows the mathematical percentage change of the measured impedance used to plot dose-response. The system response shows a 3% standard error on most of the dose concentrations thus demonstrating the precision of measurement. Box-whisker plots were created as shown in Fig 3b to investigate the variability of the system response for a given dose concentration irrespective of buffer pH. The true variability of the sensor response was observed to be 10% inter-sample variation in the form of inter-quartile region height of each of the glucose dose concentrations. It can be observed that even with a larger variability, the median divides the inter-quartile region symmetrically, demonstrating a Gaussian distribution. However, there is a need to model this variation as a mathematical relationship to allow accurate detection as well as differentiation of glucose dose concentrations across the dynamic range.

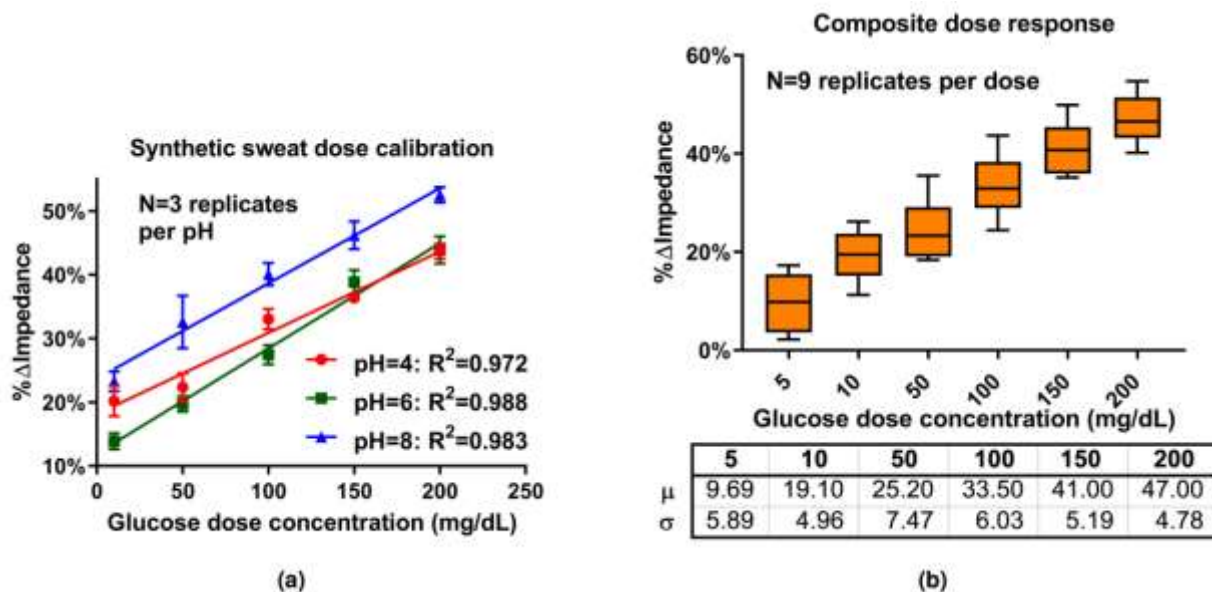


Figure 3.10. A. Calibration dose-response of the system using synthetic sweat buffer of various pH. B. A box-whisker plot is used to observe the true variability of a given dose concentration as a composite of all buffers used in this experiment.

3.8 Effect of temperature and RH

The goal of the sensor is to function as a wearable device; hence, assessing its performance over a wide range of temperatures from room temperature to elevated body temperature is important. Figure 9B shows the test conditions set for the temperature study, in which a temperature profile ranging from 25 to 40 °C and back to 25 °C was applied twice to the sensor as well as the sensor module. Concurrently, at an interval of 5 min, dose concentrations starting from 10 to 200 ng/mL were dispensed in increments of 10 ng/mL. Figure 9C, D shows measured fractional change in Z_{mod} and Z_{imag} for synthetic sweat buffer for pH 4 and 8. The measured change of Z_{imag} was fit to a second-order polynomial with an R^2 of ~ 0.92 . Table 2 shows the R^2 and the variability of the fractional change function of Z_{imag} measured for 90 min. Based on this R^2 value, a variability

of ~7.6% from the ideal second-order polynomial fit was shown for a temperature range of 25–40 °C for repetitive temperature cycles.

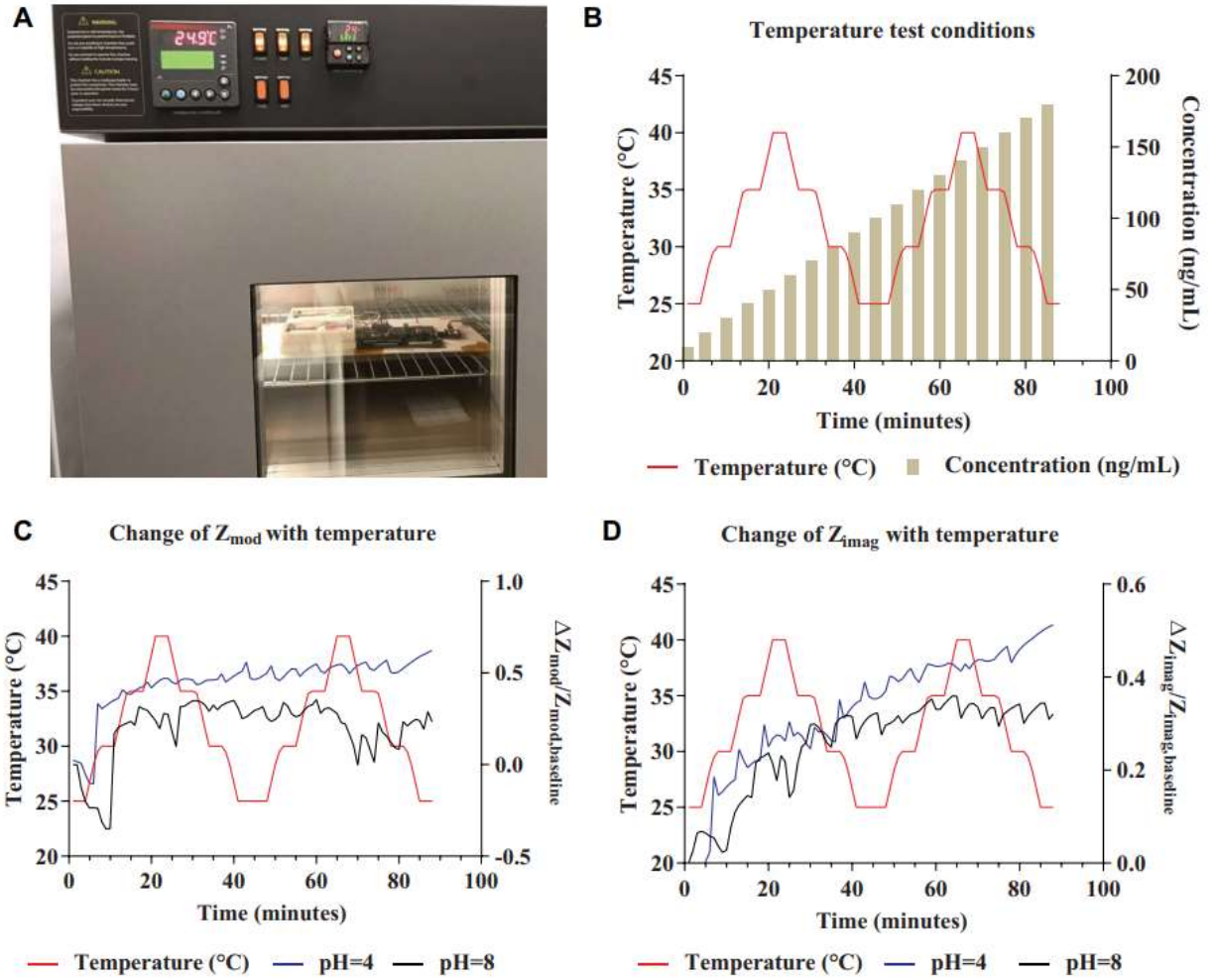


Figure 3.11. The sensor module was connected to four cortisol biosensors and placed in the temperature chamber for temperature testing. The change of measured impedance parameters was recorded, along with the instantaneous temperature. Cortisol doses made in synthetic sweat buffer of pH 4 and 8 were used for this experiment. (B) The test conditions for temperature study include an increase of dose concentration every 5 min and a change of temperature as per a profile. (C) Fractional change of Z_{mod} . (D) Fractional change of Z_{imag} . The change in Z_{imag} is a quadratic function corresponding to an increase in cortisol dose concentration irrespective of change in temperature[57].

3.9 Incremental noise analysis of the sensor

Noise is an undesirable measured quantity that accompanies a true measured quantity. This introduces an amount of uncertainty in the accuracy and repeatability of the measurement device. Sources of noise have been well characterized for CMOS devices in the past[58]–[60]. Primarily, the two major sources of noise discussed in academic as well as industrial design are thermal noise and flicker noise for complementary metal-oxide-semiconductor (CMOS) transistors. Thermal noise is a result of electrical fluctuations caused by thermal energy[60]. This electron motion is popularly known as Brownian motion. The RMS noise voltage is expressed as in (3.1) where k is the Boltzmann constant, T is the absolute temperature in kelvin and R is the resistance of the device under test. Thus, thermal noise will increase with the temperature rise. In CMOS transistors, this noise is a summation of the noise generated by the gate and channel resistance. In case a capacitor is connected in parallel with the resistive noise source, the RMS thermal noise is denoted as in Eqn. 3. Thus, thermal noise can be controlled using a shunt capacitor[61].

$$\overline{v_{thermal}^2} = 4kTR \quad (3.1)$$

$$\overline{v_{RC}^2} = \frac{kT}{C} \quad (3.2)$$

Flicker noise or popularly known as $1/f$ noise is the resultant of attractive forces at the silicon-oxide interface in a CMOS transistor giving rise to several energy states[58]. The RMS flicker noise is expressed as in Eqn. 4 where K is a statistically calculated, process-dependent parameter, W and L are the dimensions of the transistor, C_{ox} is the capacitance of oxide film per square and f is the frequency of interest. Thus, $1/f$ noise is a function of frequency and is a source of error for low-frequency circuits.

$$\overline{v_f^2} = \frac{K}{WLC_{ox}\Delta f} \quad (3.3)$$

A comprehensive noise model [62] is used to provide a noise treatment for the biosensors mentioned in this work. For a non-faradaic electrode-electrolyte interface, the valence of the electrolyte is z . In addition, the measurement is performed for a single frequency, thus the bandwidth of the system is 1 Hz. Fig 1c shows the incremental circuit model established using impedance measurements[63]. Three noise sources due to R_s , R_{ASA} , and R_{ct} can be identified using previously mentioned noise equations. Moreover, the measurement device's response time of 13 ms is smaller than the biosensor's response time of 5 minutes. Based on these assumptions, a noise model was proposed for the biosensor used in this work as shown in Fig. 1d, which was derived from Fig. 1c9 by dividing the cross-section of the sensor into three parts. Since an active semiconducting film is a partially conductive film with some resistance based on its doping levels, it is prone to a noise voltage like a resistor and can be modeled as a thermal noise source. It can be assumed that there is a presence of $1/f$ noise due to this film due to semiconductor material, which is a result of charge carrier generation as well as recombination. However, since a capacitance C_{ASA} exists in parallel with the noise sources, this noise can be modeled as a kT/C noise of the active semiconducting film. Considering the biosensing electrical double layer and charge transfer resistance, these are modeled to be circuit components for an ideal polarized electrode (IPE), however, they are imperfect in a real scenario. Thus, the noise of this region can be assumed to be a variation in the current density of the charge carriers depending upon the strength of the electrical potential, which in turn depends on the location of the slip plane. However, since the ion motion is slower than an electron's motion, a function $M(\omega)$ is used to model the frequency-dependent

effect of this current noise source. The solution resistance is a bulk effect and can be assumed to be a resistor, thus the thermal noise effect. The final expression of the noise voltage would be a summation of all these noise sources as given in Eqn. 5.

$$\begin{aligned} \overline{v^2} = & 4kT(R_S + R_{electrode}) + 2zqI.M(\omega).(R_{ct}|\left|\frac{1}{j\omega C_{dl}}\right|) + kT C_{ASA} \\ & + \frac{K}{WLC_{ox}\Delta f} \end{aligned} \quad (3.4)$$

The veracity of this model is confirmed using a noise test for 30 minutes on a non-functionalized sensor surface wet with 1X phosphate saline buffer (PBS) using a high-speed potentiostat (Zurich Instruments, Switzerland). Fig. 2c shows the variation of noise spectra at an interval of 5 minutes. The noise voltage follows a trend inversely proportional to the frequency and is maximum at t=5 minutes, whereas it decreases with time and is at a minimum at t=30 minutes at 100 Hz excitation frequency. Thus, as the introduction of PBS reaches an equilibrium, the noise amplitude of the system starts decreasing for 100 Hz excitation frequency. The RMS noise voltage is shown in Fig. 2b.

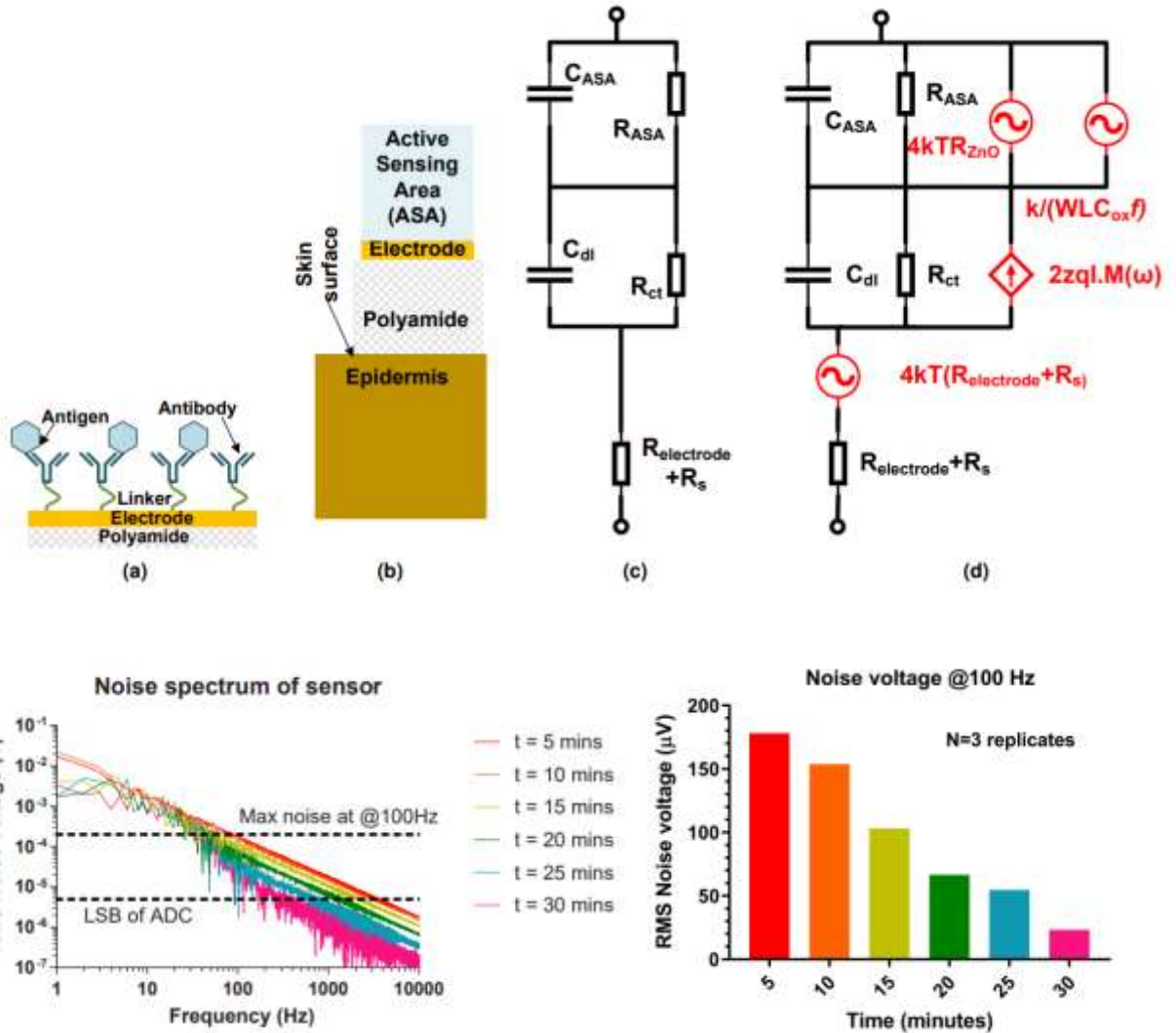


Figure 3.12. (a) A cross-section of antigen-antibody interaction on the functionalized biosensor surface. (b) Cross-section of the materials of the biosensor when placed on the skin (not to scale). (c) Incremental circuit model of the biosensor. (d) Noise source superposition on the incremental circuit model. (e) FFT noise spectrum of the biosensor when dosed with synthetic sweat without glucose, demarcated with noise margins. (f) Noise voltage level progression for the 100 Hz band of the FFT spectrum over 30 minutes.

3.10 Finite state machine (FSM) approach to firmware implementation

A finite state machine (FSM) is a finite automaton, which is a mathematical model of computation.

It is an abstract machine that can have one or more states at a given point in time. This architecture

is capable of transitioning from one state to the other when provided with the right input triggers. FSMs can execute a predetermined set of tasks based on the sequence of events that may interact with it, e.g., vending machines, elevators, traffic lights, etc. Wearable device firmware also depends on FSM architecture to ensure proper user interaction and data collection when deployed. The FSM used for this work is shown in Figure 3.13.

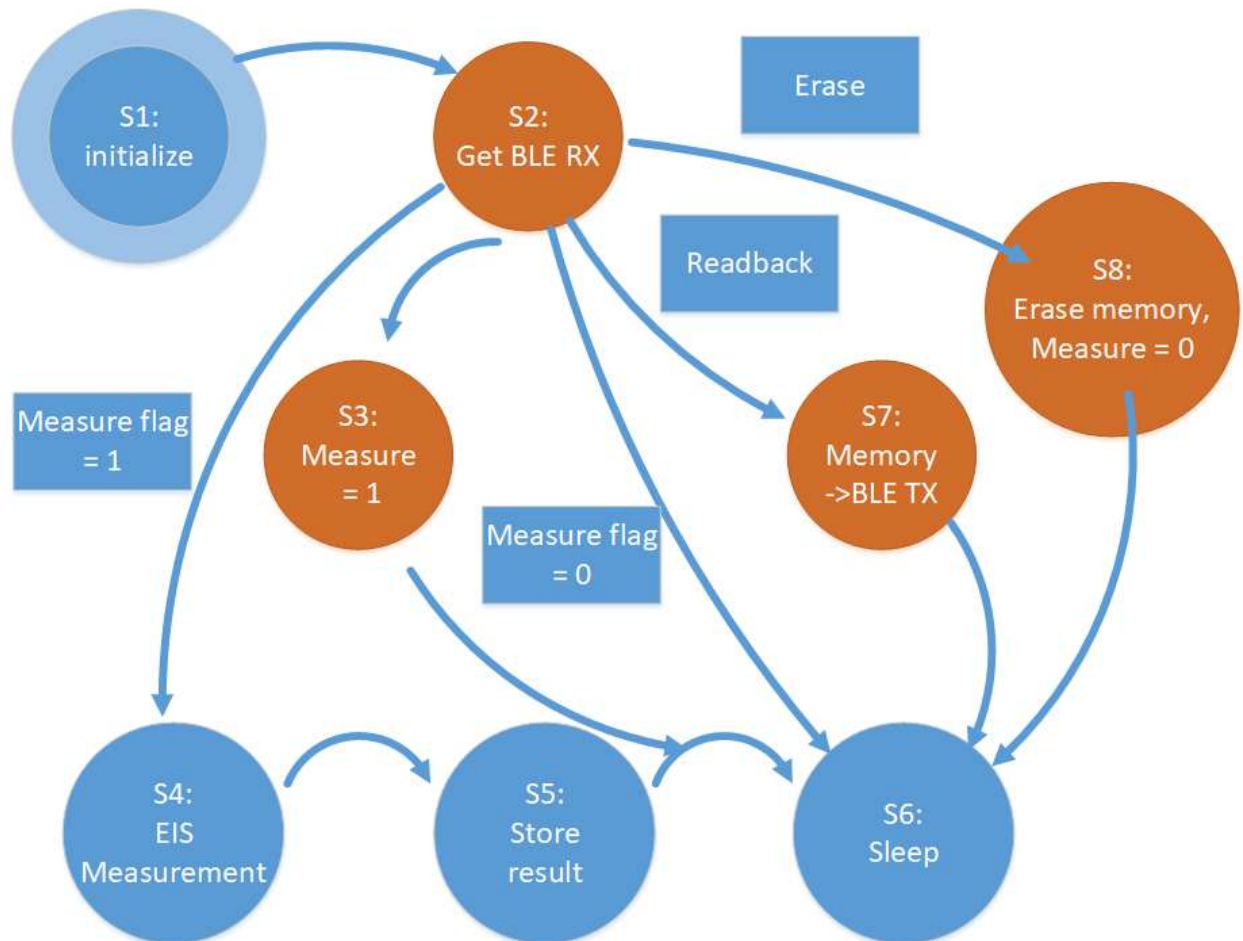


Figure 3.13. An example of a finite state machine for the proposed wearable device with states demarcated as S_n and relevant flags.

The wearable firmware begins proper initialization of the device at state S_1 , then moves into state S_2 , which performs a read from the Bluetooth coprocessor. This checks for any commands received from a smartphone. If the command is received, it will be parsed and proper actions will

be taken, e.g., a trigger of a measurement or memory readback. However, if no measurement was performed earlier, and a measure command is received, the flag will be set high in state S3. This will ensure program execution now goes through states S4 and S5. State S6 is introduced as a sleep time to ensure the FSM does not enable any peripherals or processor cores during this period for saving battery power. This time may be adjusted and is discussed in the next section. When a readback command is issued, state S7 sends all stored impedance measurements to the smartphone for data curation. When the measurement is not required anymore, the erase command is issued, wherein state 8 erases all recorded measurements and disables the measure flag.

3.11 Power optimization using time-averaging

For the proposed wearable device, the ultimate objective to be achieved would be very similar to a data conversion system, i.e., achieving a low power consumption per every measurement performed. Similarly, the capability of the device to measure with minimal power will be observed by varying operating conditions. A battery-operated device is generally operated at a very low, sleep-mode supply current. However, the device requires a larger amount of current to operate in an active state. Thus, for such an uneven distribution of current, an average over the time taken by the device to execute the program from start to end. Thus, the battery selection for a fixed average current is performed as follows.

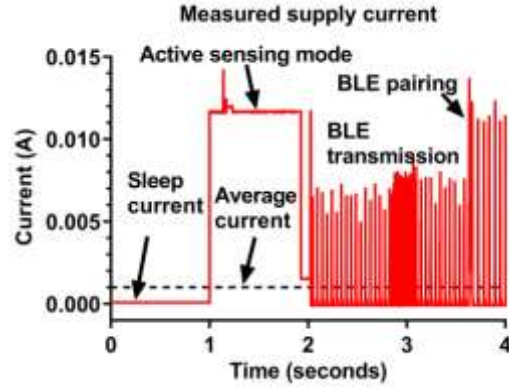


Figure 3.14. Measured current consumption of the proposed wearable device using a DC power analyzer. Each of the FSM states is demarcated to highlight the shape of the current waveform as per firmware execution.

Let the sleep current of the device in question be I_{sleep} for time t_{sleep} and the active current of the device is I_{active} for time t_{active} . Since the device completes one program cycle, the total time for one program cycle t_{total} is the summation of t_{sleep} and t_{active} . For the proposed device, I_{sleep} was found to be 0.1mA, I_{active} as 12mA, t_{sleep} as 60 s, and t_{active} as 1s. Assuming the Bluetooth data transfer does not happen until explicitly triggered, the battery life can be calculated using the measurements above, leading to an average current of 1 mA using Eqn. (3.5) and Eqn. (3.6). If a battery of 168mAh is used, the system will be functional for 168 hours, i.e., 1-week, meeting the target objective.

$$t_{\text{total}} = t_{\text{sleep}} + t_{\text{active}} \quad (3.5)$$

$$I_{\text{avg}} = I_{\text{sleep}} \times \frac{t_{\text{sleep}}}{t_{\text{total}}} + I_{\text{Active}} \times \frac{t_{\text{active}}}{t_{\text{total}}} \quad (3.6)$$

CHAPTER 4

MODELLING SENSOR BEHAVIOR FOR HUMAN SUBJECT DATA

The behavior of a biosensor can be established using conventional methods in a steady environment, at a fixed temperature, and relative humidity. However, the effects of the environmental and human subjects may affect the outcome of the sensor quite differently in comparison to the pre-established sensor. Hence, understanding the behavior of the wearable device in interaction with a cohort of human subjects would give a deeper insight into system robustness towards clinical acceptance. The upcoming sections discuss the collection and analysis of human subject data using time-series analysis and machine learning regression methods.

4.1 Collection of human subject data

An independent sample t-test was performed between the reference and the sensor data to validate the distribution probability and to compare the mean distribution between the analytical methods. The total mean measurements at each time point are accompanied by a sample size of 40 (10 subjects \times 4-time points) and their respective variability in concentrations are presented in the supplementary section. These values confirm that the differences in the distributions of the measurements by the method are statistically insignificant. Regarding reporting the biomarker levels among the three methods of data collection for the two sweat markers, it can be observed that the power lies between 0.82 and 0.87 with an α of 0.05. Based on this study, we are confident that there is a possibility of achieving a power value of >0.93 in future work by increasing the cohort of participants in the study. This would help healthcare professionals in understanding the

relationship between macronutrient consumption versus fluctuations in glycemic-adrenal indices by relying on measurements from the WATCH sensing platform.

4.2 Methods of modeling

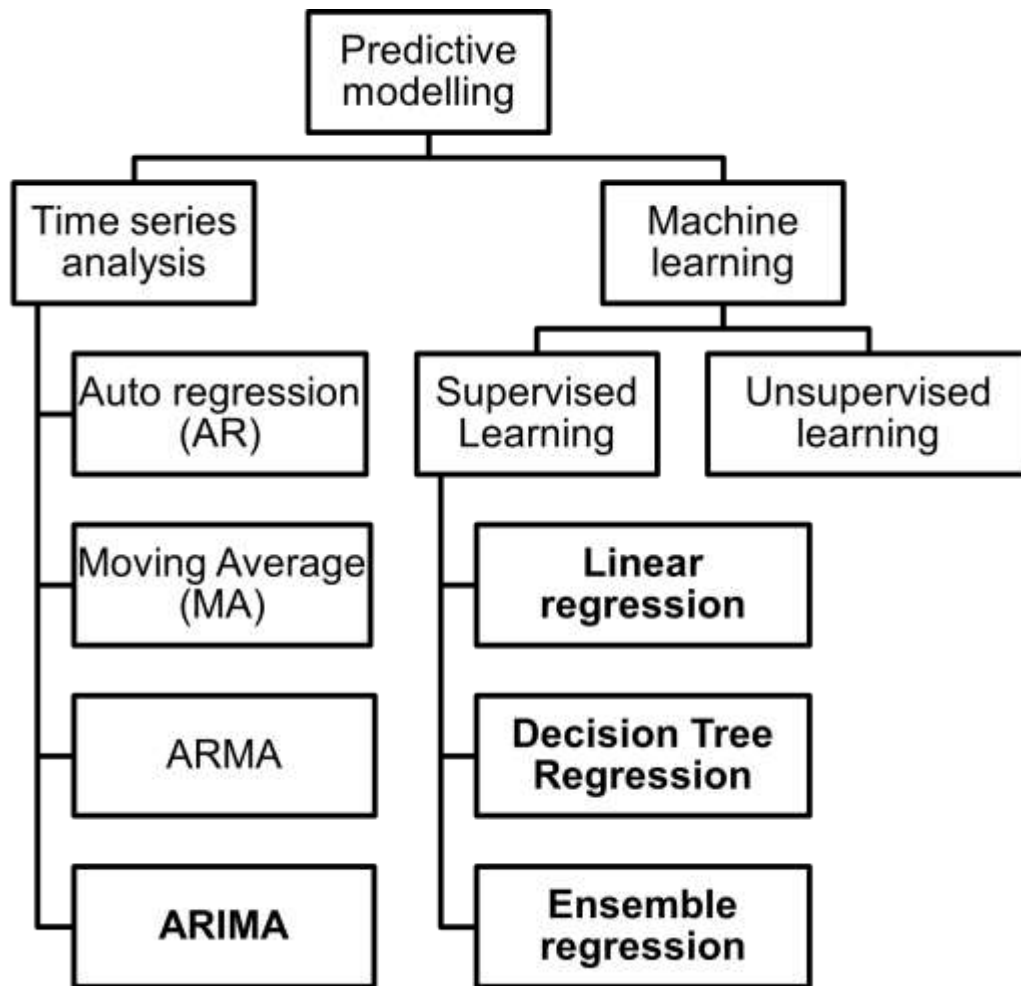


Figure 4.1. Classification of methods of data modeling for the proposed wearable device. The methods shown in bold are discussed in this work.

4.3 Exploratory data analysis and preparation

Exploratory data analysis is the process of performing an initial investigation on data to discover patterns, correlations, find anomalies check for assumptions using graphical plots.

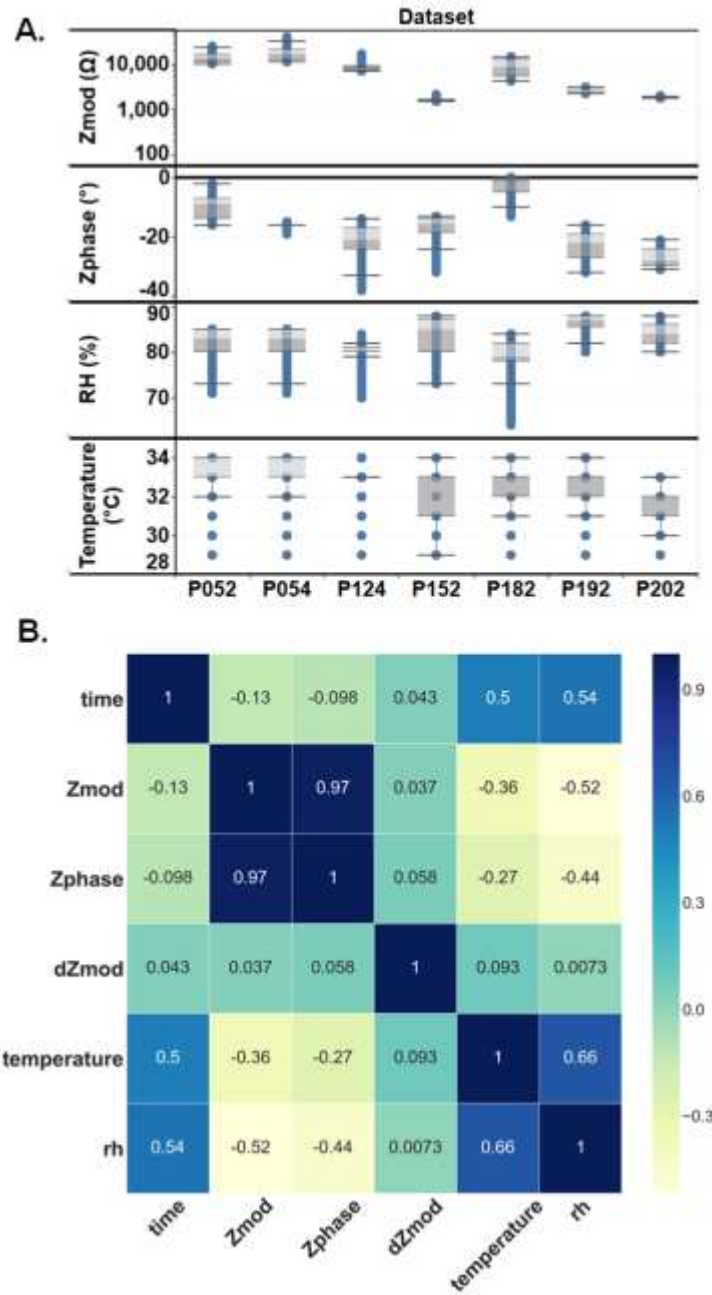


Figure 4.2. (A) Box plot of values of selected features across the data collected from various subjects. (B) Correlation matrix of the selected features for the training data.

Before building a machine learning algorithm for glucose sweat prediction, the dataset was explored to understand the underlying relationship between the data set. The signal obtained is the impedance signal of the sensor which translates to values of glucose present in the sweat. As seen

in Figure 2(A) we see the distribution box plot overall range for Z_{mod} value lies between 1-20k Ω . The sensor used for this study is the capacitive sensor and we expect to see the values of Z_{mod} within 30k Ω and subsequent Z_{phase} values would be mostly negative. Apart from the impedance signal, we have also integrated temperature and RH sensors on the reader. The skin temperature and %RH have been measured at every minute and provided as the input for the prediction of the sweat glucose. Figure 2(A) shows the overall distribution of measure input parameters. Overall observed values for the temperature are in the range of 28-36 °C with a mean value of 33.5 °C and mean %RH values for the subjects included in the study is 82. The observed temperature statistics do match with the generalized description of the healthy human cohort while performing routine activities as described in figure 1(B). With the input signal being a complex impedance signal in terms of Z_{mod} and Z_{phase} , another confounding which is dZ_{mod} , which is the running difference of the Z_{mod} values between the previous and current values. As explained in the model building section we have seen the improvement of accuracy in the model with addition dZ_{mod} .

The relationship within the input parameters has been analyzed with the help of a correlation matrix. Figure 2(B) shows the correlation matrix presented in terms of heatmap where blue is 1 which is the highest possible positive correlation and yellow is the maximum negative correlation of -1. The in-between values are represented by the gradients of yellow for the negative correlation and gradients of blue for the positive correlation. The main intent behind analyzing the correlation matrix is to avoid redundant features while modeling. The highest correlation is seen between Z_{mod} and Z_{phase} with 0.97 Pearson's correlation coefficient. As both the parameters are highly correlated, so we include only Z_{mod} values for the model building. Other parameters that show reasonable correlation with each other can be used as input parameters to the machine learning

model. This confirms there are no redundant features that will be included in the model-building stage.

4.3.1 Interpolation

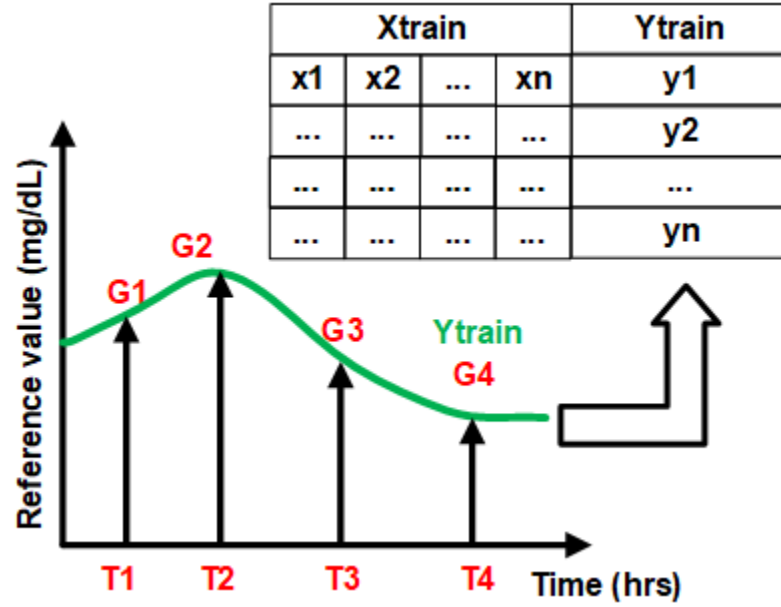


Figure 4.3. Concept diagram of interpolation signal generation using reference points.

Figure 3(A) represents the building of a continuous signal using the discrete data points. The discrete glucose concentration from the sweat is measured using the ELISA method and the signal is interpolated to obtain a smooth continuous time-varying signal. Given the periodic nature of the glucose molecule, we use a bicubic method of interpolation. The obtained continuous signal is used as the output parameter for regression building. The continuous signal is obtained for minute frequency. The interpolation method allows performing on-demand sampling of the glucose. Based on the nature of the dataset we have tested the linear regression, decision tree regression, and ensemble regression algorithm available in the MATLAB toolbox.

4.4 Machine learning-based regression

The system-level block diagram used for the glucose monitoring system has been explained in Figure 7. The data collection is done with the help of an electrochemical sensor and reader. The reader samples the impedance signal at every minute. Along with impedance skin temperature and relative humidity are also measured. The raw input signal is transferred to the cloud storage server via a mobile application. The raw input signal is passed to the data pipeline and predicted glucose concentration. output is obtained at the end of the pipeline. As the system is the on-demand user can request any time to see the predicted glucose output. The training of the model has been taken care of in a separate pipeline. The extracted final model is used for the prediction of glucose concentration.

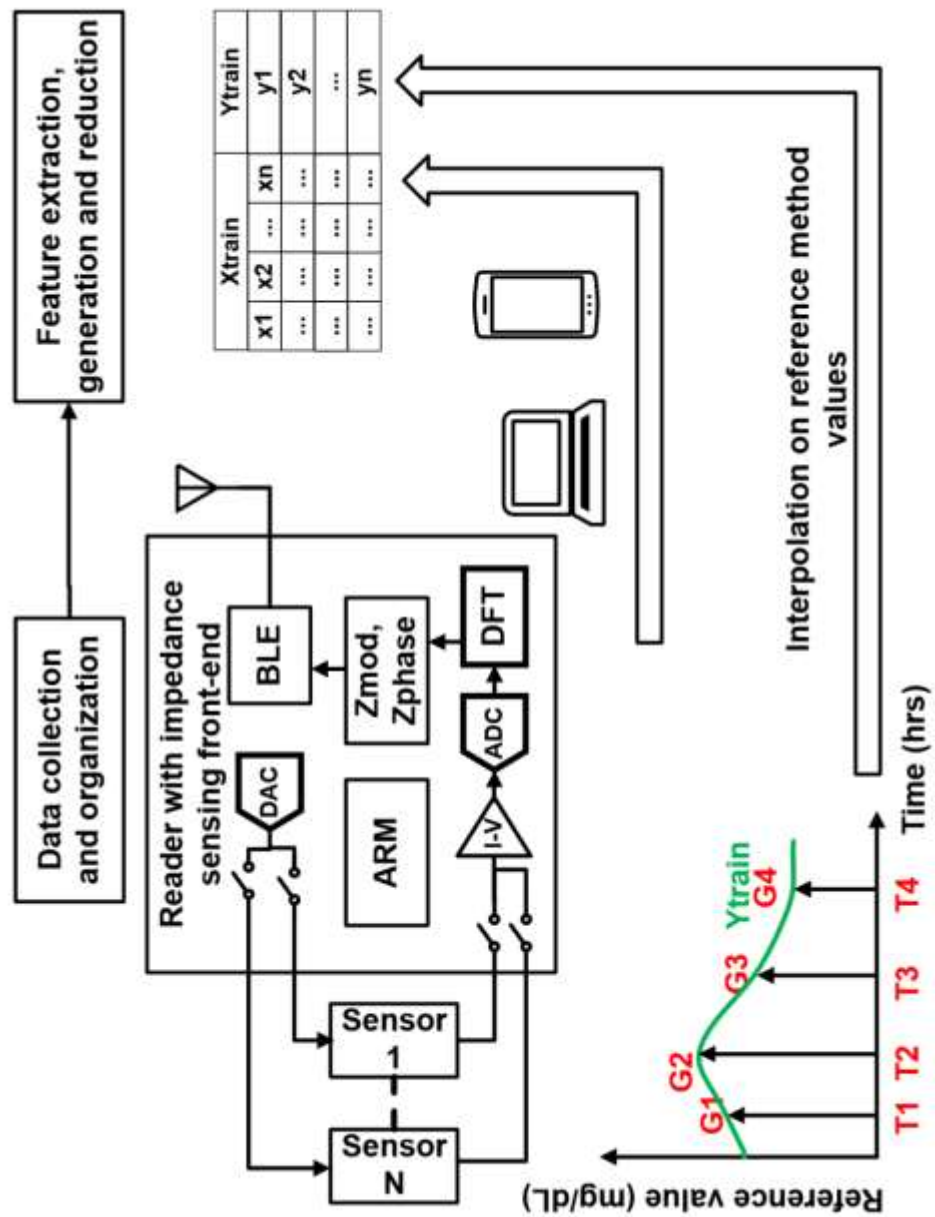


Figure 4.4. Complete system-level diagram of the wearable device-app-cloud platform infrastructure to support collection, curation, and analysis of sweat biosensor data, part 1 of 2.

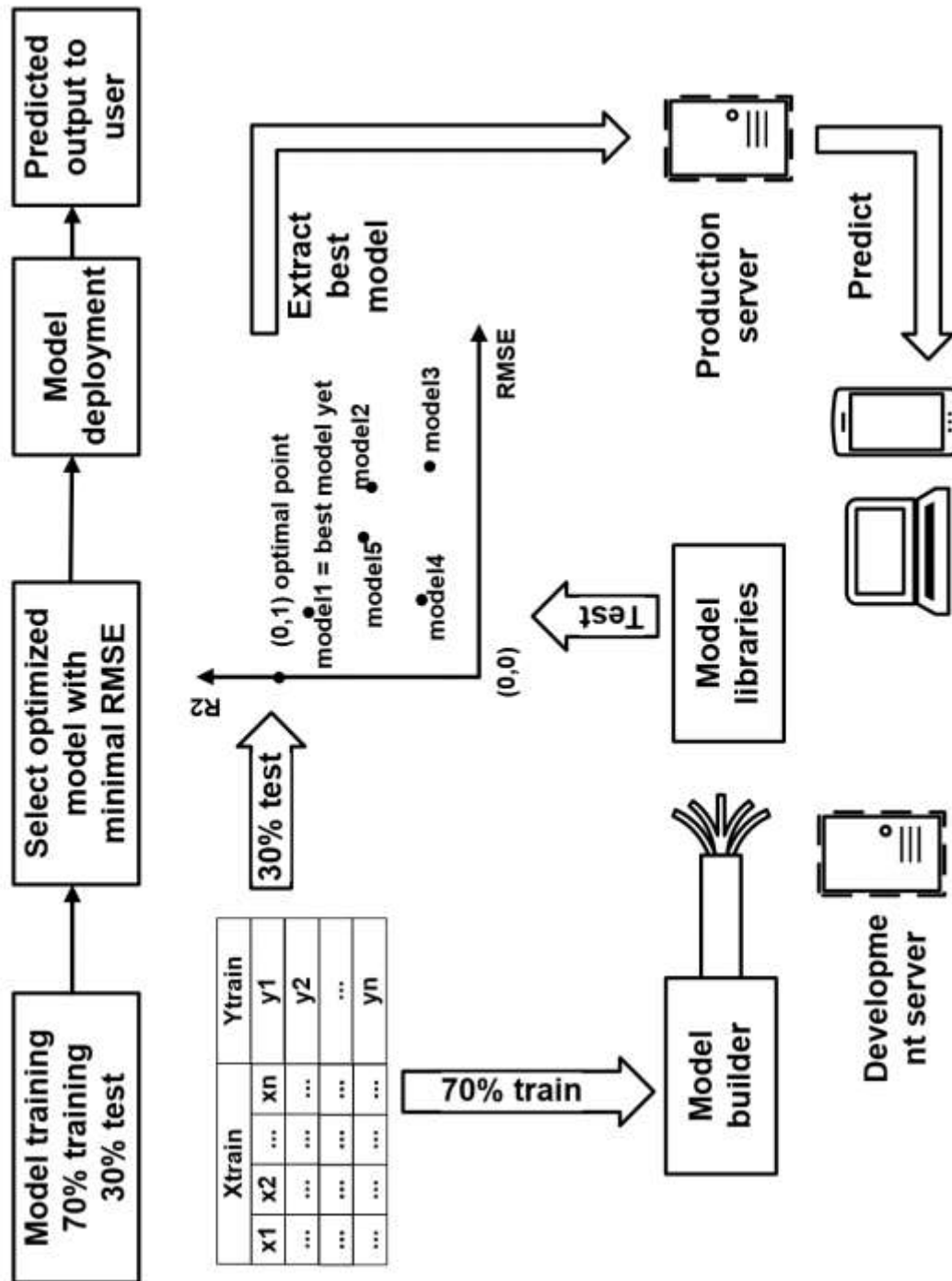


Figure 4.5. Complete system-level diagram of the wearable device-app-cloud platform infrastructure to support collection, curation, and analysis of sweat biosensor data, part 2 of 2.

4.4.1 Generalization

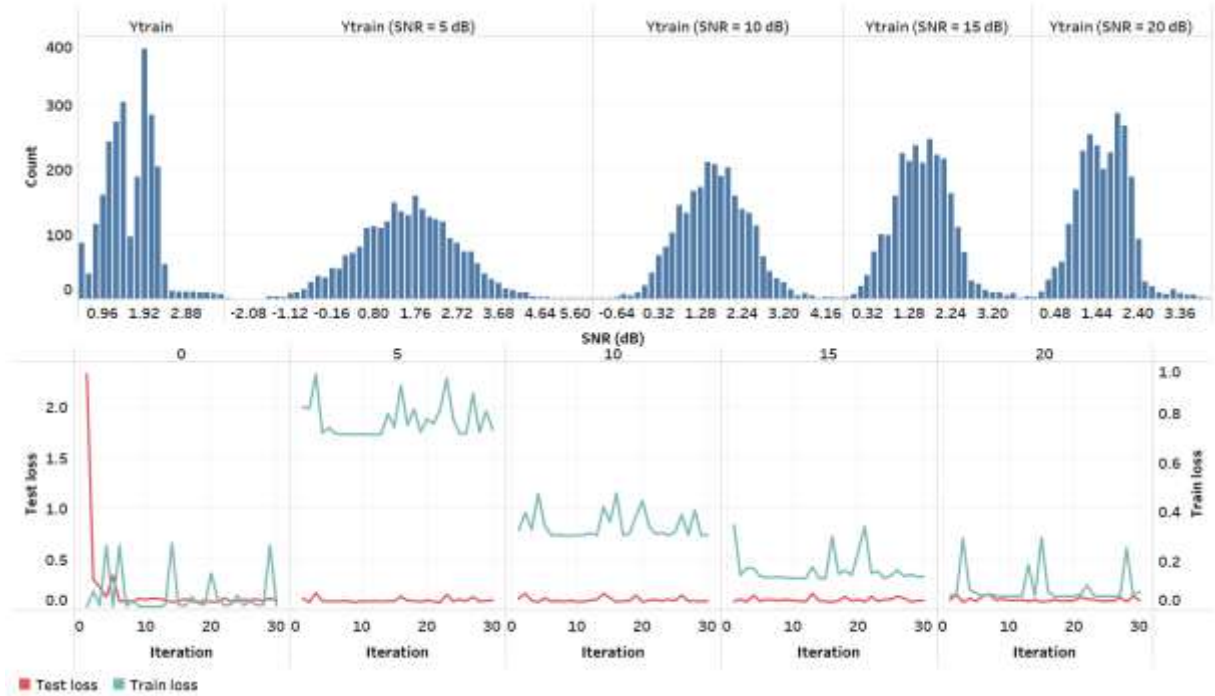


Figure 4.6. Change in the skew of interpolated training dataset when adding Gaussian noise with varying equivalent SNR of the output signal. This affects the change in train and test loss.

Figure 4 explains the noise addition to introduce the variability for generalization. The results obtained from the interpolation are vulnerable to real-world noises from various sources. To take care of these shortcomings, a Gaussian noise parameter, also known as additive white noise, was introduced to the result set that was obtained from the interpolation. The results obtained after adding white noise resulted in response signals with a signal-to-noise (SNR) ratio of values 1, 5, 10, 15, and 20 dB were analyzed to select the final choice of model. The objective is to minimize the loss but also to allow room for generalization and avoid overfitting. From Figure 4, SNR of 10 dB avoided overfitting of the train and test loss with the minimum gap between predicted and actual output. In the case of higher SNR values, the train and test loss look very similar to the

response signal without any noise. In the case of lower SNRs, the train and test loss values do not seem to converge, showing an error of $>20\%$, which is beyond the acceptable clinical limits[64]. Hence, SNR of 10 dB was found to be the optimal SNR ratio for the generalization of the model training process.

4.4.2 Validation methodology

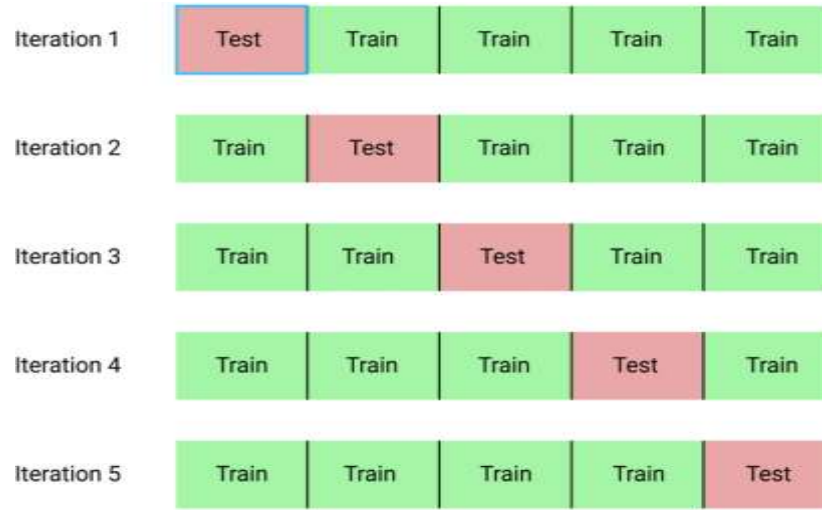


Figure 4.7 An example of the workflow of the k-fold validation methodology.

Figure 4.7 represents the k-fold method where the execution was done in the iteration manner and the results are represented as box plots for the visual comparison in Fig. 4B. K value was chosen as 5 for this study. The dataset size was comparatively small, hence $k = 5$ provided a robust outcome. K-fold validation helps to build confidence in the model performance. Figure 4B captured the essence of all 5 iterations with the methodology they were executed. The next phase of model building is algorithm selection. We have tested logistic regression, naïve Bayes, k-nearest neighbor, decision tree, and support vector machine using the k-fold cross-validation method for spot quick checking the performance of the algorithms. K-fold cross-validation

process adds the additional validation phase during the training phase itself. This happens before the model is exposed to the test dataset. The training process is broken down into k iterations. The training dataset is divided into the k sections. All $(k-1)$ sections are used for the training and the remaining one is used as the internal validation set. The performance of the algorithm is noted for the iteration. The same is repeated for the k items every time the validation set is different. The performance of the algorithm is aggregated for comparison. For the study, we have used $k=5$.

4.4.3 Training results

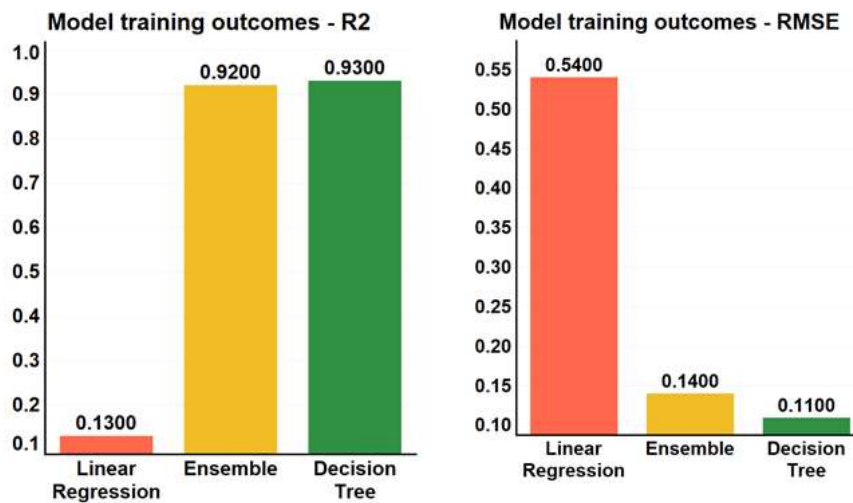


Figure 4.8. Comparison of the RMSE and R2 values obtained for various machine learning regression models used during the model training process.

4.4.4 Test results

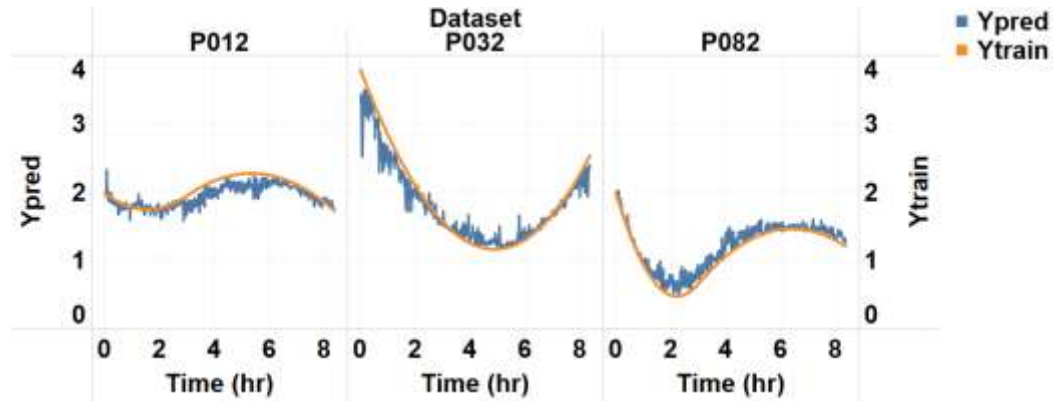


Figure 4.9. Results obtained on the test dataset for the 3 human subject data showing the actual progression of reported values and interpolated reference values.

The next set of results obtained were from testing the algorithms for sweat glucose prediction on the human subject and the algorithm has been tested on three subjects. The predicted value follows the trends for the sweat glucose value. The sweat values for the test subject are converted to a continuous curve using the same bicubic interpolation methodology used for building the continuous monitoring set values. The predicted values show the presence of the noise when added via the generalization process. The decision tree model building has used two types of generalization techniques. As given in the MATLAB Machine Learning toolbox the L1 regularization offered by the algorithm to reduce the statistical overfit of the model was used. Also, the addition of external white noise to the level of SNR=10 dB signal to the training values. The noise addition takes care of variability that might be present in the real signal. The overall results give a good fit when the predicted signal is compared with the actual signal.

4.5 Time series analysis

A time series is simply a series of data points ordered in time. In time series, time is often the independent variable, and the goal is usually to make a forecast for the future. Time series data can be described using certain mathematical characteristics such as the change in value over time and the direction in which the amplitude of the data fluctuates. Such properties of the time series data used in common literature are discussed below.

4.5.1 Trend

A trend is a gradual upward or downward shift in the level of the series or the tendency of the series values to increase or decrease over time. Trends are either local or global, but a single series can exhibit both types. Trends can also be either linear or nonlinear. Linear trends are positive or negative additive increments to the level of the series, comparable to the effect of simple interest on the principal. Nonlinear trends are often multiplicative, with increments that are proportional to the previous series value(s).

4.5.2 Seasonality

A seasonal cycle is a repetitive behavior of values in the time series data and depends on the interval of your series. For instance, monthly data typically cycles over quarters and years. A monthly series might show a significant quarterly cycle with a low in the first quarter or a yearly cycle with a peak every December. Series that show a seasonal cycle is said to exhibit seasonality. Seasonal patterns are useful in obtaining good fits and forecasts, and there are exponential smoothing and ARIMA models that capture seasonality.

A nonseasonal cycle is a repetitive, possibly unpredictable, pattern in the series values.

Some series, such as the unemployment rate, clearly display cyclical behavior; however, the periodicity of the cycle varies over time, making it difficult to predict when a high or low will occur. Other series may have predictable cycles but do not neatly fit into the Gregorian calendar or have cycles longer than a year. For example, the tides follow the lunar calendar, international travel and trade-related to the Olympics swell every four years, and there are many religious holidays whose Gregorian dates change from year to year.

Nonseasonal cyclical patterns are difficult to model and generally increase uncertainty in forecasting. The stock market, for example, provides numerous instances of series that have defied the efforts of forecasters. All the same, nonseasonal patterns must be accounted for when they exist. In many cases, you can still identify a model that fits the historical data reasonably well, which gives you the best chance to minimize uncertainty in forecasting.

Many series experience abrupt changes in level. They generally come in two types:

- A sudden, temporary shift, or pulse, in the series level
- A sudden, permanent shift, or step, in the series level
- When steps or pulses are observed, it is important to find a plausible explanation. Time series models are designed to account for gradual, not sudden, change. As a result, they tend to underestimate pulses and be ruined by steps, which leads to poor model fits and uncertain forecasts. (Some instances of seasonality may appear to exhibit sudden changes in level, but the level is constant from one seasonal period to the next.)
- If a disturbance can be explained, it can be modeled using an intervention or event. For example, during August 1973, an oil embargo imposed by the Organization of Petroleum Exporting Countries (OPEC) caused a drastic change in the inflation rate, which then returned to

normal levels in the ensuing months. By specifying a point intervention for the month of the embargo, you can improve the fit of your model, thus indirectly improving your forecasts. For example, a retail store might find that sales were much higher than usual on the day all items were marked 50% off. By specifying the 50%-off promotion as a recurring event, you can improve the fit of your model and estimate the effect of repeating the promotion on future dates. Shifts in the level of a time series that cannot be explained are referred to as outliers. These observations are inconsistent with the remainder of the series and can dramatically influence the analysis and, consequently, affect the forecasting ability of the time series model.

The following figure displays several types of outliers commonly occurring in time series. The blue lines represent a series without outliers. The red lines suggest a pattern that might be present if the series contained outliers. These outliers are all classified as deterministic because they affect only the mean level of the series.

- **Additive Outlier.** An additive outlier appears as a surprisingly large or small value occurring for a single observation. Subsequent observations are unaffected by an additive outlier. Consecutive additive outliers are typically referred to as additive outlier patches.
- **Innovational Outlier.** An innovational outlier is characterized by an initial impact with effects lingering over subsequent observations. The influence of the outliers may increase as time proceeds.
- **Level Shift Outlier.** For a level shift, all observations appearing after the outlier move to a new level. In contrast to additive outliers, a level shift outlier affects many observations and has a permanent effect.

- **Transient Change Outlier.** Transient change outliers are similar to level shift outliers, but the effect of the outlier diminishes exponentially over the subsequent observations. Eventually, the series returns to its normal level.
- **Seasonal Additive Outlier.** A seasonal additive outlier appears as a surprisingly large or small value occurring repeatedly at regular intervals.
- **Local Trend Outlier.** A local trend outlier yields a general drift in the series caused by a pattern in the outliers after the onset of the initial outlier.

Outlier detection in time series involves determining the location, type, and magnitude of any outliers present. Tsay (1988) proposed an iterative procedure for detecting a mean level change to identify deterministic outliers. This process involves comparing a time series model that assumes no outliers are present to another model that incorporates outliers. Differences between the models yield estimates of the effect of treating any given point as an outlier.

4.5.3 Autocorrelation

Autocorrelation and partial autocorrelation are measures of association between current and past series values and indicate which past series values are most useful in predicting future values. With this knowledge, you can determine the order of processes in an ARIMA model. Hence, an autocorrelation function (ACF) is the correlation between series values that are k intervals apart. Partial autocorrelation function (PACF) is the correlation between series values that are k intervals apart, accounting for the values of the intervals between. The x-axis of the ACF plot indicates the lag at which the autocorrelation is computed; the y axis indicates the value of the correlation (between -1 and 1). For example, a spike at lag 1 in an ACF plot indicates a strong correlation between each series value and the preceding value, a spike at lag 2 indicates a strong correlation

between each value and the value occurring two points previously, and so on. A positive correlation indicates that large current values correspond with large values at the specified lag; a negative correlation indicates that large current values correspond with small values at the specified lag. The absolute value of a correlation is a measure of the strength of the association, with larger absolute values indicating stronger relationships.

4.5.4 Stationarity in time-series data

A stationary time series is one for which the statistical properties do not change over time, however, it does not imply that the time series data does not vary over time. In a clearer aspect, the properties of the change of values in the times series data can be considered as conserved or unchanged.

The Augmented Dickey-Fuller test for a unit root assesses the null hypothesis of a unit root using the model

$$y_t = c + \delta t + \phi y_{t-1} + \beta_1 \Delta y_{t-1} + \dots + \beta_p \Delta y_{t-p} + \epsilon_t,$$

where

- Δ is the differencing operator, such that $\Delta y_t = y_t - y_{t-1}$.
- The number of lagged difference terms, p , is user-specified.
- ϵ_t is a mean zero innovation process.

The null hypothesis of a unit root is

$$H_0: \phi = 1.$$

Under the alternative hypothesis, $\phi < 1$.

Variants of the model allow for different growth characteristics. The model with $\delta = 0$ has no trend component, and the model with $c = 0$ and $\delta = 0$ has no drift or trend.

A test that fails to reject the null hypothesis fails to reject the possibility of a unit root. Engle's ARCH test assesses the null hypothesis that a series of residuals (r_t) exhibits no conditional heteroscedasticity (ARCH effects), against the alternative that an ARCH(L) model describes the series.

The ARCH(L) model has the following form:

$$r_t^2 = a_0 + a_1 r_{t-1}^2 + \dots + a_L r_{t-L}^2 + \varepsilon_t,$$

where there is at least one $a_j \neq 0$, $j = 0, \dots, L$.

The test statistic is the Lagrange multiplier statistic TR_2 , where:

- T is the sample size.
- R^2 is the coefficient of determination from fitting the ARCH(L) model for several lags (L) via regression.

Under the null hypothesis, the asymptotic distribution of the test statistic is chi-square with L degrees of freedom.

4.5.5 Operations on time-series data

The most common operations that can be applied to time-series data are autoregression and moving average.

$$y = X_1\beta_1 + \dots + X_p\beta_p + \varepsilon_t \quad (4.1)$$

$$y = \frac{1}{q} (X_1\beta_1 + \dots + X_q\beta_q) \quad (4.2)$$

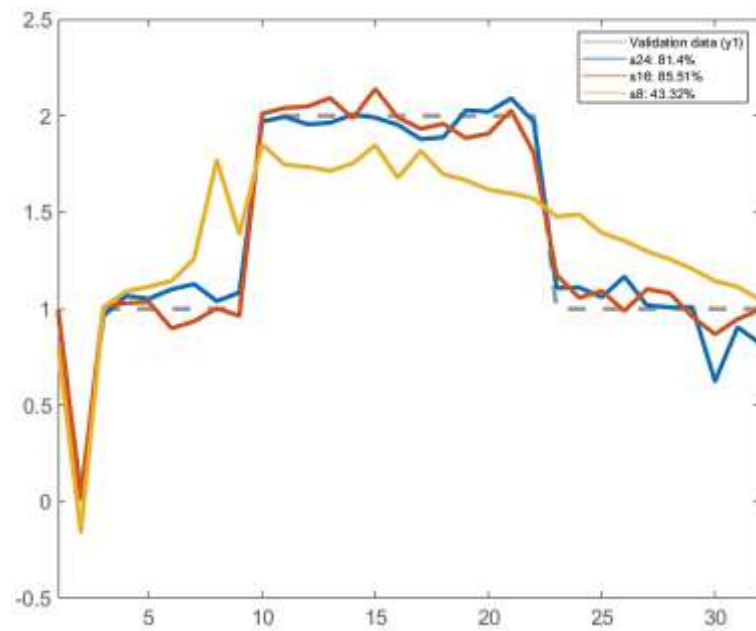


Figure 4.10. An example of an autoregression function with window sizes 8, 16, and 24 when evaluated for a square wave pulse. Higher AR order implies a good fit for fast-moving input signals.

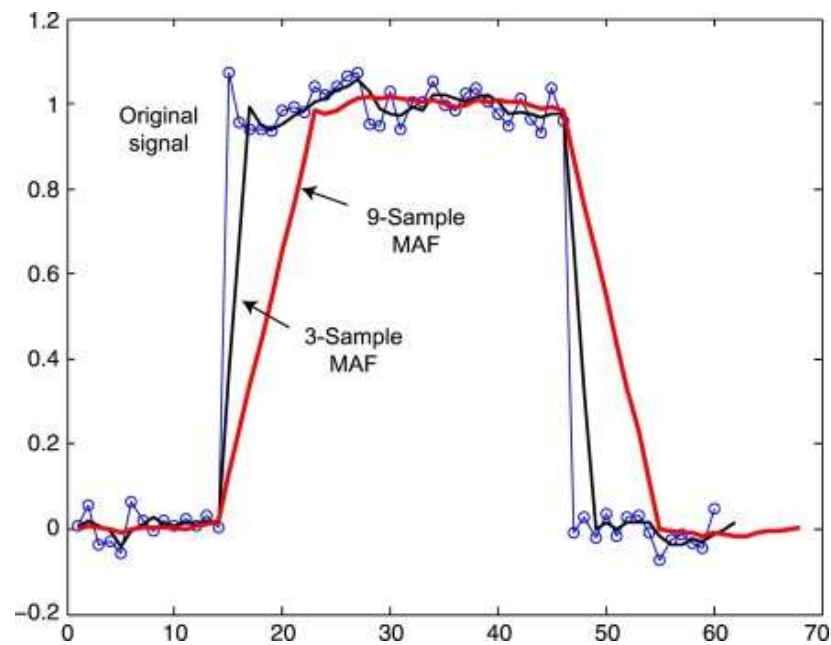


Figure 4.11. An example of a moving average function with window sizes 3 and 9 when evaluated for a square wave pulse. Higher window size implies a sluggish response in time.

4.5.6 ARIMA modeling and test results

ARIMA(p,d,q) is one of the most commonly used curve fit functions used for time-series analysis, where p is the order of auto-regressive (AR) terms, d is the number of integrating terms and q is the number of moving -average (MA) terms. For the above data set, p was determined using the number of significant peaks in the auto-correlation plot of the primary predictor's impedance magnitude (Zmod) and first differential of impedance magnitude (dZmod), which shows a change in sensor response with change in glucose concentration as per dose calibration. Figs. 4a,4d show 2 extreme cases among the 20 data set, wherein the autocorrelation plot shows 5 initial lag peaks for subject 1 and 10 initial lag peaks for subject 2, which exceed the 3σ confidence interval. Hence, the maximum peaks are defined as $p = 10$. The ARIMA(10,0,3) regression curve fit used for the above data sets is given in Eqn. 13 and Eqn. 14, where y is the output, X is the input values for the predictors, β are the coefficients obtained from regression ARIMA fit, μ is the variance, L is the lag operator, θ are the moving average coefficients and ϵ_t is Gaussian white noise. The coefficients of the ARIMA(10,0,3) curve fit are shown in Table 2. The p-value for a given predictor defines its significance in predicting the output time series, which is the interpolated sweat glucose value. If $p < 0.05$, then the predictor 5/14 is assumed to be significant as it rejects the null hypothesis, else the predictor can be assumed to be non-significant, hence can be removed from the curve fit expression. In this case, predictors AR4 can be safely assumed to not contribute to the prediction. The AIC of this curve fit was -3131.438 , ensuring a good curve fit and low prediction error. This is corroborated by the ARIMA outputs plotted against the interpolated glucose values in Figs. 5a, 5b. The error histogram is shown in Fig. 5c, demonstrating a low predicted sweat glucose error for the interpolated sweat glucose measurements.

$$y = X_1\beta_1 + \cdots + X_{10}\beta_{10} + \mu_t \quad (4.3)$$

$$(1 - \phi_1 L - \cdots - \phi_{10} L^{10})\mu_t \quad (4.4)$$

$$= (1 + \theta_1 L + \theta_2 L^2 + \theta_3 L^3)\varepsilon_t \quad (2)$$

Table 4.1. ARIMA (10,0,3) coefficients

Predictor	Value	Std. Error	p-value
Intercept	2.2236	0.0011792	0
AR1	1.1696	0.016376	0
AR2	-0.79248	0.015316	0
AR3	0.71839	0.044644	2.9197e-58
AR4	0.10234	0.044076	0.020235
AR5	-0.22962	0.032213	1.0166e-12
AR6	0.1	0.034417	0.0036662
AR7	-0.20436	0.034488	3.109e-09
AR8	0.11278	0.03253	0.00052668
AR9	-0.075336	0.032725	0.021328
AR10	0.085203	0.026248	0.0011702
MA1	-0.60583	0.017528	9.1092e-262
MA2	0.7133	0.024382	3.8771e-188
MA3	-0.40103	0.050977	3.6377e-15
Beta(Zimag)	-0.00025308	4.887e-06	0
Beta(Zmod)	0.00054978	1.1027e-05	0
Beta(Zphase)	-0.023363	0.0014868	1.2261e-55
Beta(Zreal)	-0.00047466	9.8819e-06	0
Beta(dZimag)	-5.2582e-06	6.8561e-07	1.7285e-14
Beta(dZmod)	-7.0023e-06	1.5741e-07	0
Beta(dZphase)	-0.0045203	0.0022546	0.044974
Beta(dZreal)	1.1458e-05	6.5176e-07	3.5439e-69
Beta(rh)	-0.022069	0.00070336	4.2615e-216
Variance	0.0075866	0.00025797	4.2045e-190

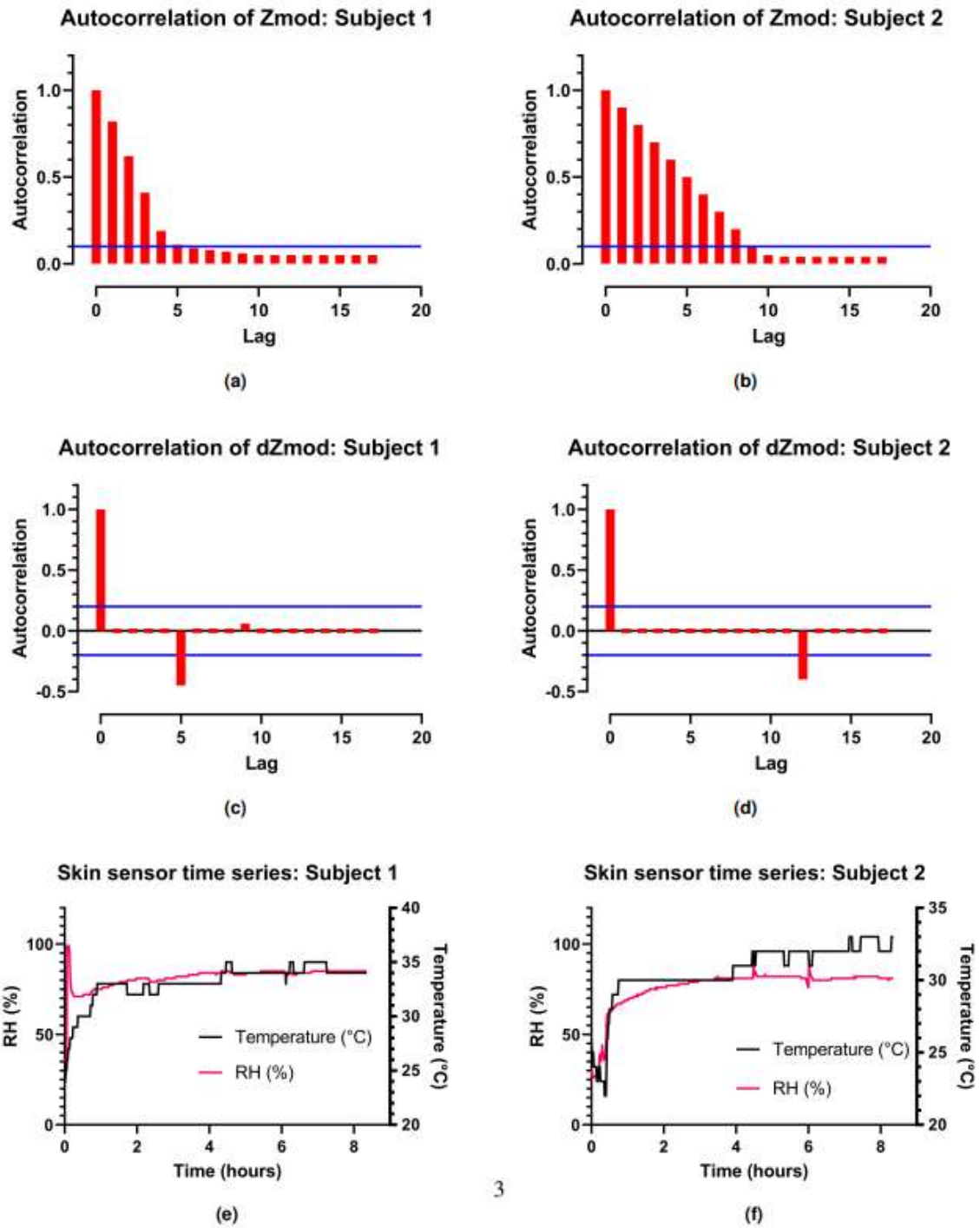


Figure 4.12. (A) Autocorrelation plot for Zmod for subject 1. (B) Autocorrelation plot for Zmod for subject 2. (C) Autocorrelation plot for dZmod for subject 1. (D) Autocorrelation plot for

dZmod for subject 2. (E) Skin temperature and relative humidity for subject 1. (F) Skin temperature and relative humidity for subject 2.

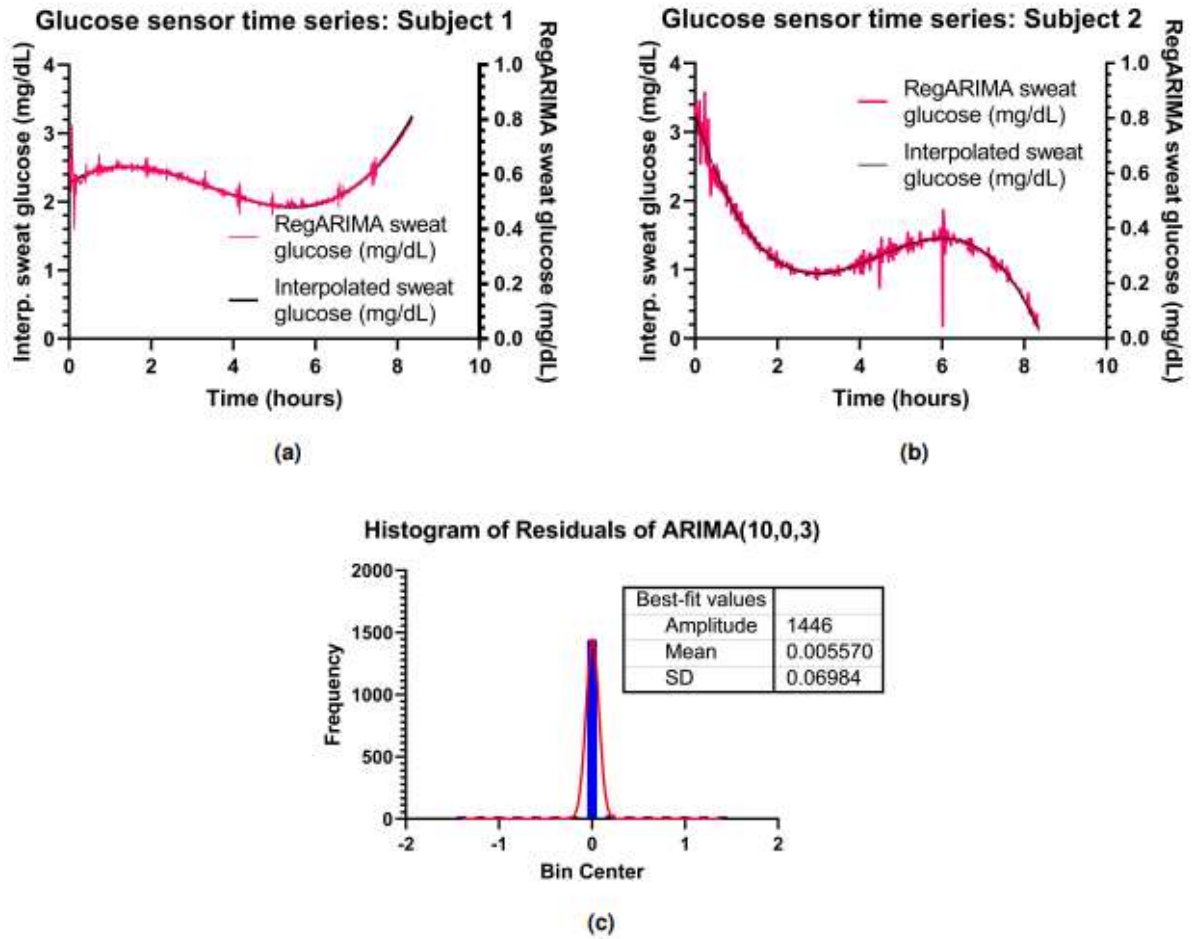


Figure 4.13. (A) Comparison of interpolated vs. RegARIMA sweat glucose concentrations for subject 1. (B) Comparison of interpolated vs. RegARIMA sweat glucose concentrations for subject 2. (C) Histogram of residuals for ARIMA(10,0,3) model.

CHAPTER 5

CONCLUSION

This work is a discussion of the methodology of designing a wearable device that is integrated with an electrochemical glucose sensing, sweat biosensor which can be used as a decision support system for diabetic users. The wearable device was designed keeping in mind the philosophy of design from the commercial wearable market while adding novelty in linking a biological signal response to auxiliary sensing and a data collection platform. The wearable device was tested for impedance measurement accuracy of 1% and noise performance that is at least 20x better than the noise performance of the sensor at 100 Hz. The firmware of the device was written as a finite state machine to provide rudimentary interaction with the device for starting data recording, retrieving data, and turning off measurement for efficient battery usage for 1 week. The resultant wearable platform was implemented and used to collect data from 10 human subjects to understand the behavior of the system under varied user conditions, environmental states, and sedentary lifestyles. The data collected was used to analyze the measurement performance of the device against a clinical reference, and two modeling methodologies, ARIMA vis-à-vis machine learning regression, were used to assess the interdependence of data features with the interpolated reference output. This sensing scheme can be further extended for multiplexed detection of biomarkers in various combinations and biological media to detect the presence, absence, or modulation of said biomarker(s) due to an underlying condition or factor affecting the user's lifestyle.

APPENDIX

ELECTRICAL DESIGN DOCUMENTATION

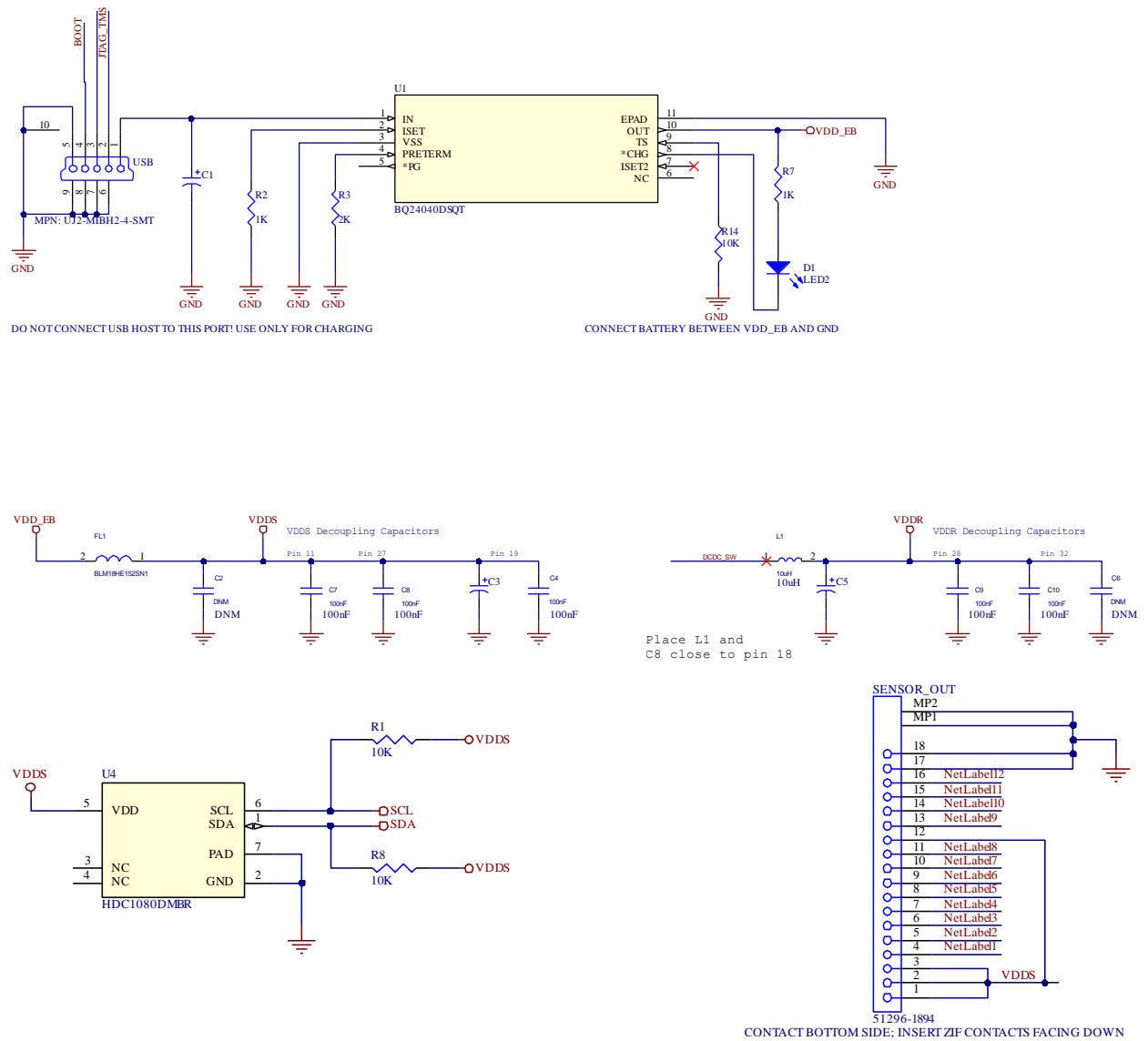


Figure A.1. Schematic, printed circuit board layers and assembly information for the proposed wearable device.

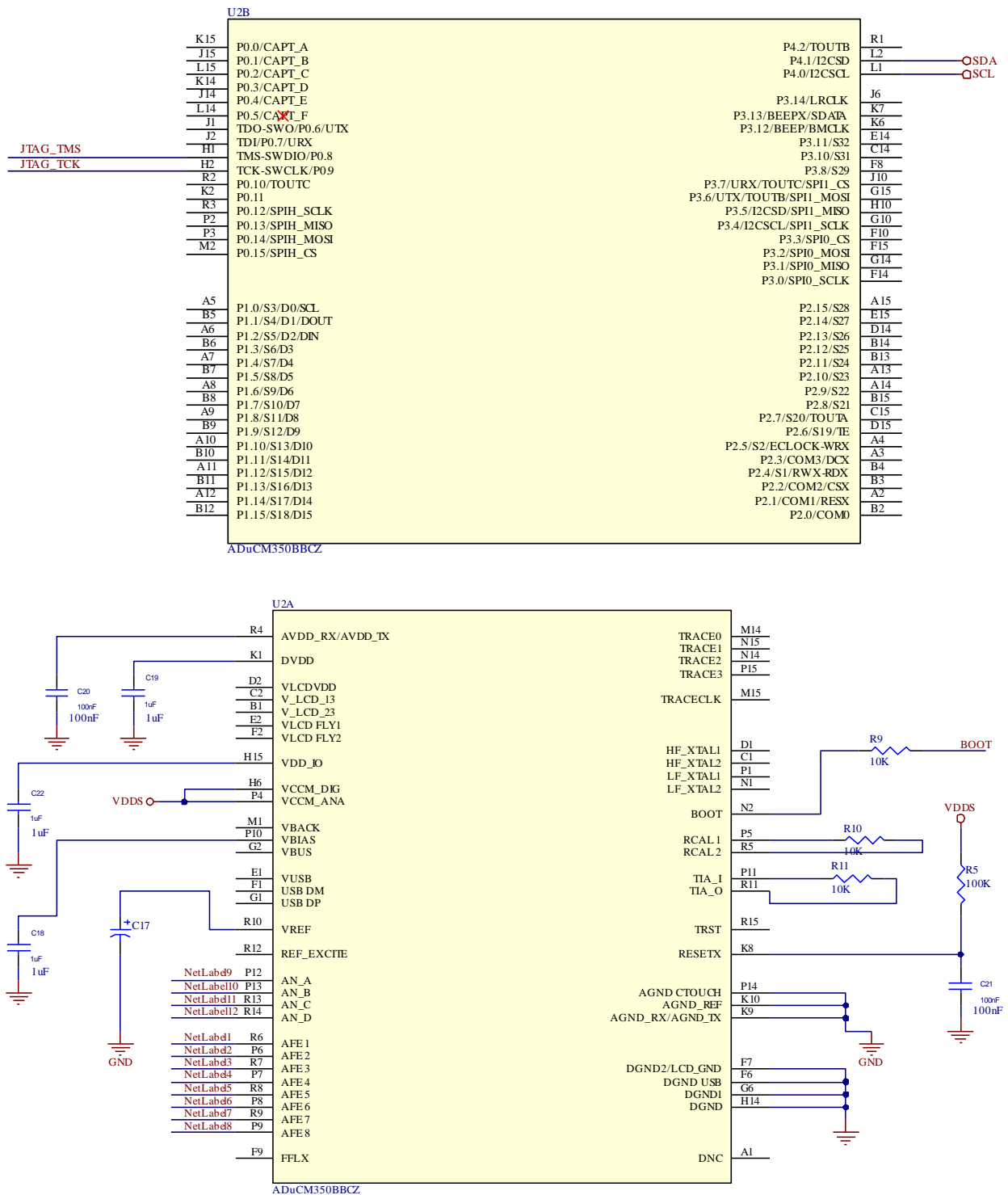
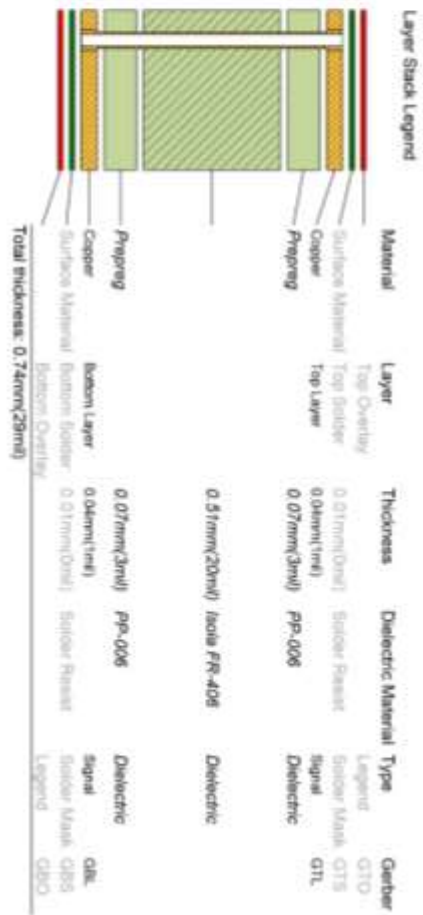
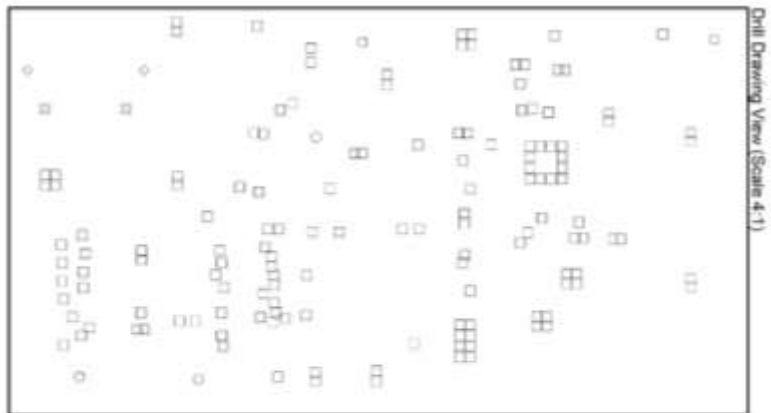


Figure A.1. continued.



Print Table				
Symbol	Count	Hole Size	Hole Type	Via / Pad Template
□	141	0.06mm(1.00000000000mm)	Plated Round	(Mixed)
■	2	0.65mm(2.56200000000mm)	Plated Slot	(Mixed)
■	2	0.65mm(2.56000000000mm)	Plated Slot	2700_120x60_140x100
○	3	0.71mm(2.80000000000mm)	Plated Round	120_120x60_Bor100
○	3	2.54mm(100.0000000000mm)	Non-Plated Round	Via (Mixed)
150 Total				Pad c120x54

Fabrication Notes

1. Hole tolerances are ± 0.003 in for holes less than 20 mil, else ± 0.005 in
2. Minimum line width is 0.003 in with 0.003 in clearance
3. ENIG Board finish
4. Top silkscreen only

Figure A.1. continued.

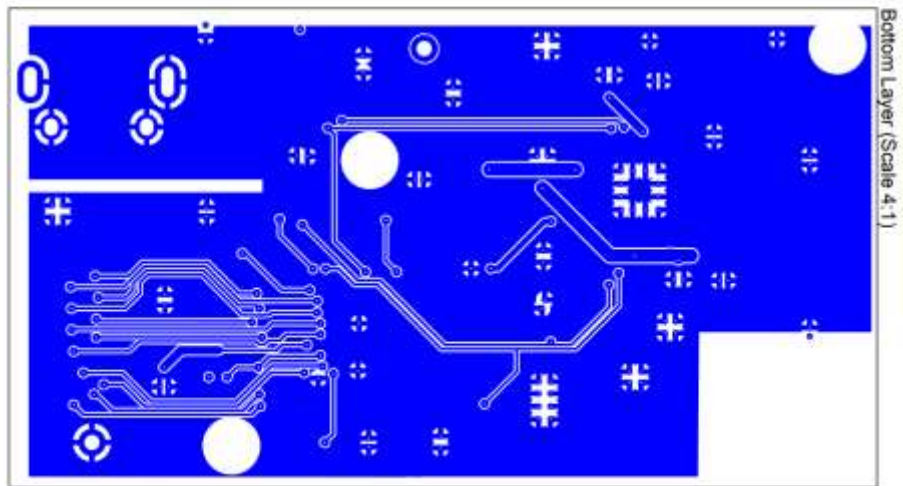
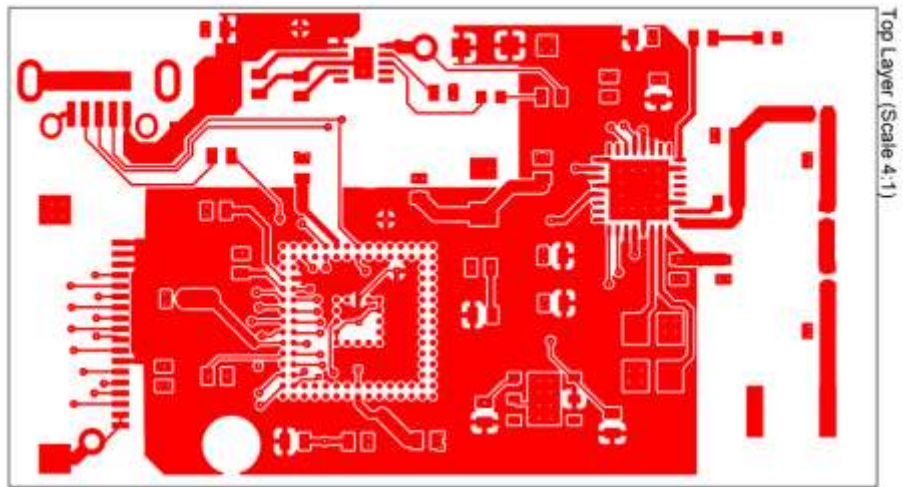


Figure A.1. continued.

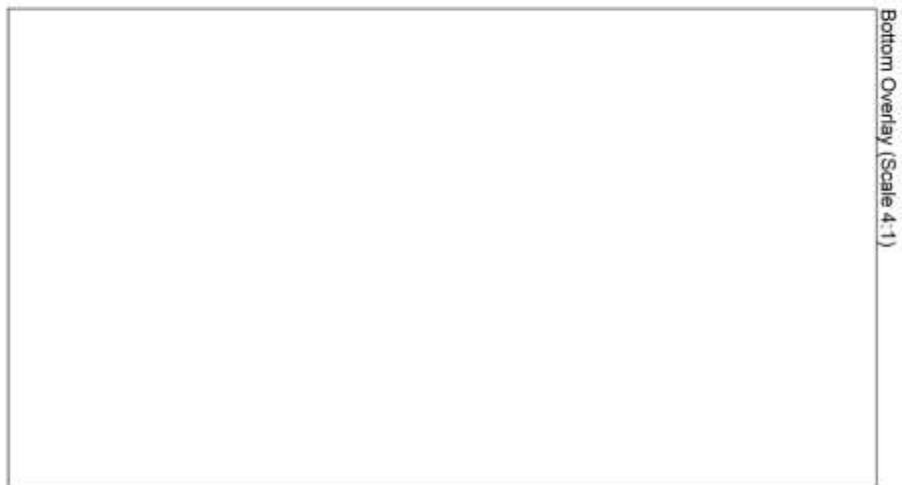
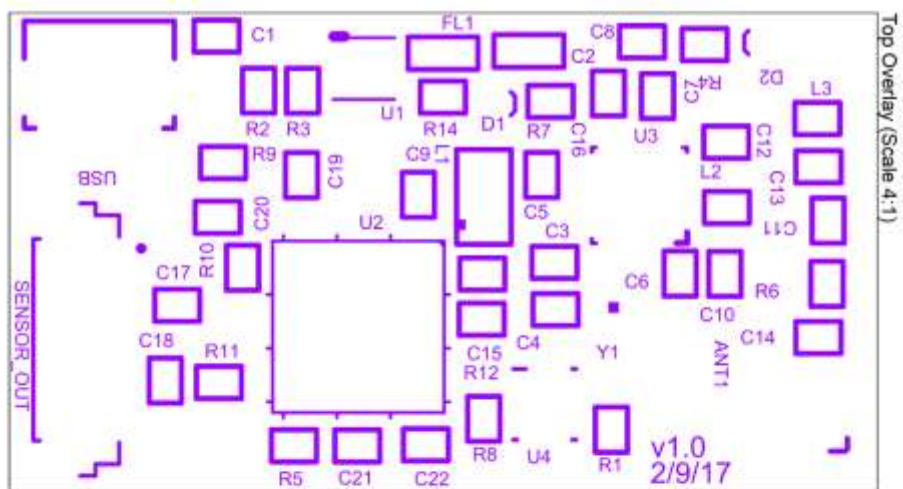
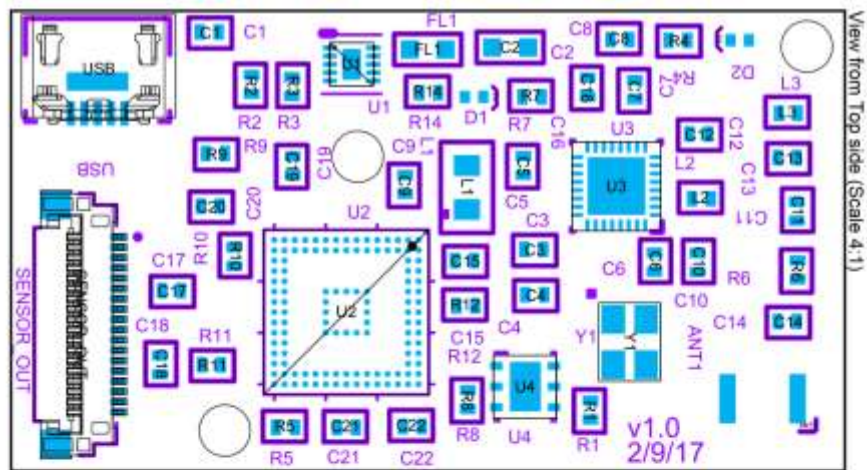


Figure A.1. continued.



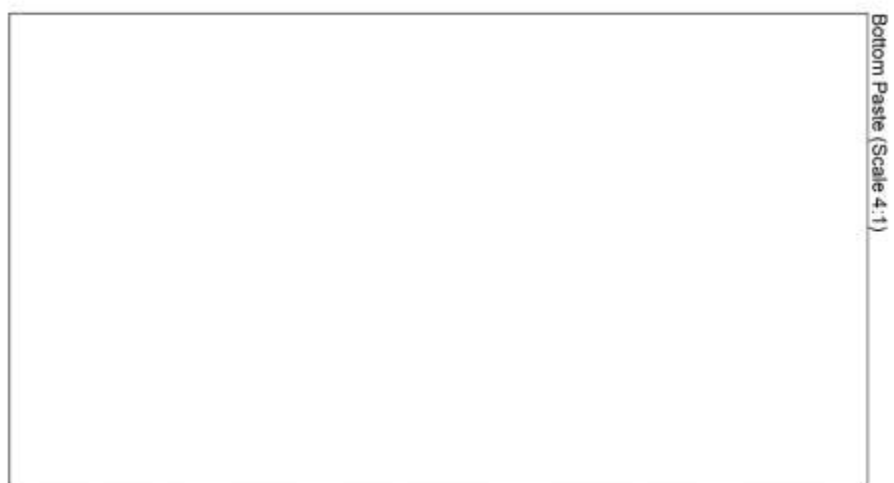
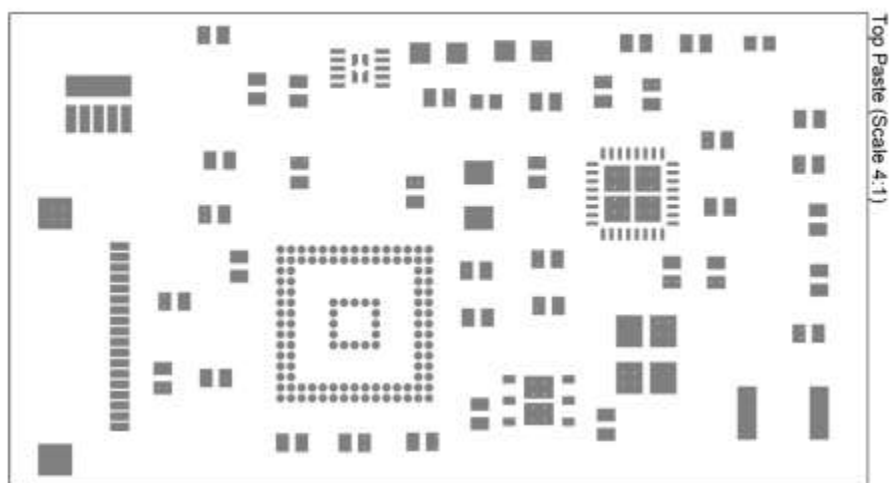


Figure A.1. continued.

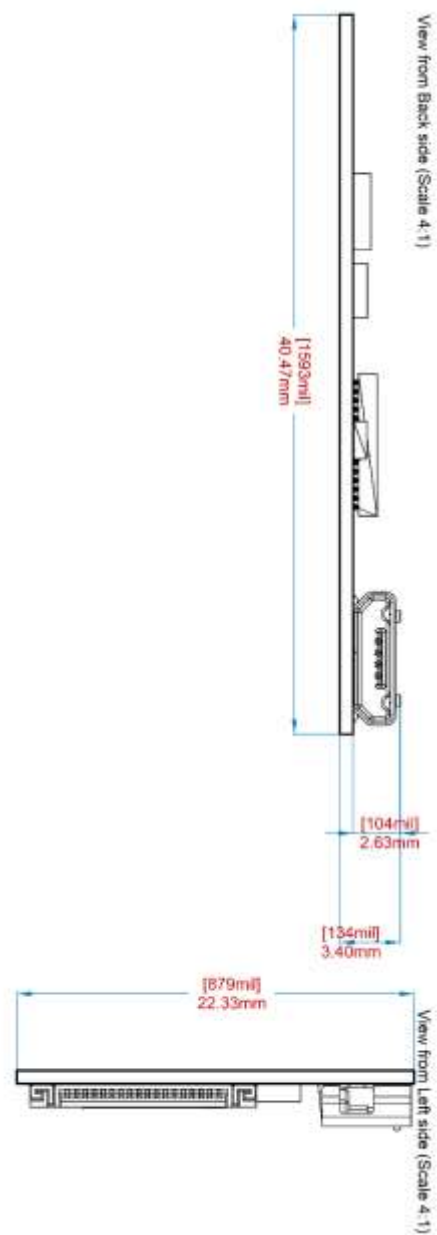


Figure A.1. continued.

Table A.1. Pick and place information for components used for the wearable device.

Designator	Layer	Footprint	Center-X(mil)	Center-Y(mil)	Rotation
R14	Top Layer	402	797.945	722.52	360
C17	Top Layer	402	306.386	344.567	180
C18	Top Layer	402	284.449	202.551	270
C22	Top Layer	402	766.732	84.724	360
C12	Top Layer	402	1313.976	643.779	180
Y1	Top Layer	TSX3225	1182.087	246.142	90
ANT1	Top Layer	FR05-S1-N-0110B	1436.024	137.874	180
R12	Top Layer	402	869.095	315.039	360
R5	Top Layer	402	524.575	83.039	360
SENSOR_OUT	Top Layer	MOLX-51296-1894	144.685	279.606	270
R11	Top Layer	402	382.874	202.835	180
R10	Top Layer	402	426.181	409.527	270
R9	Top Layer	402	390.465	606.378	180
R8	Top Layer	402	873.032	136.189	90
R6	Top Layer	402	1502.953	383.937	90
R1	Top Layer	402	1107.284	116.22	90
L3	Top Layer	402	1485.236	683.149	360
L2	Top Layer	402	1319.102	520.047	360
L1	Top Layer	805	871.063	541.417	270
FL1	Top Layer	603	796.26	805.197	180
C21	Top Layer	402	640.748	82.756	360
C20	Top Layer	402	380.622	505.984	180
C19	Top Layer	402	538.386	583.291	90
C16	Top Layer	402	1101.661	733.425	90
C15	Top Layer	402	866.221	401.937	180
C14	Top Layer	402	1483.268	285.512	180
C13	Top Layer	402	1483.268	598.504	180
C11	Top Layer	402	1500.984	496.142	270
C10	Top Layer	402	1311.728	398.212	270
C9	Top Layer	402	752.953	547.323	90
C8	Top Layer	402	1163.465	823.976	360
C7	Top Layer	402	1191.929	728.425	90
C6	Top Layer	402	1229.334	398.838	270
C5	Top Layer	402	979.331	583.583	90
C4	Top Layer	402	1000.701	336.693	180
C3	Top Layer	402	998.732	423.307	180
C2	Top Layer	603	953.74	809.134	0

U1	Top Layer	DSQ10_P9X1P5	650.748	776.89	0
D1	Top Layer	LED0402	884.842	714.646	180
D2	Top Layer	LED0402	1392.433	822.913	360
U4	Top Layer	DMB0006A	982.6	160.971	0
USB	Top Layer	USB_B_MICRO	165.354	702.835	270
U3	Top Layer	TI_RSM_4x4mm	1156.614	544.213	180
U2	Top Layer	BC_120_3	640.748	303.228	270
R4	Top Layer	402	1274.323	822.913	180
R3	Top Layer	402	536.417	734.331	270
R2	Top Layer	402	459.646	738.551	90
R7	Top Layer	402	995.362	714.646	0
C1	Top Layer	402	378.654	838.661	180

Table A.2. Bill of materials for the components used in the wearable device.

Designator	Description	Manufacturer Part Number	Manufacturer
ANT1	Fractus Micro Extend 2.5Ghz Chip Antenna	FR05-S1-N-0-102	Fractus
C1, C3, C5, C17	Polarized Capacitor (Surface Mount)	GRM155R60J106ME44D	Murata
C2		DNM	DNM
C4	Capacitor, Ceramic X7R, 100nf, 25V, -10%/+10%, -	C0402C104K8PACTU	KEMET
C6, C14		DNM	DNM
C7, C8, C9, C10, C15, C20, C21	CAPACITOR, CERAMIC X7R, 100nf, 6.3V, -10%/+10%, -, 0402, SMD	C0402C104K8PACTU	KEMET
C11	CAPACITOR, CERAMIC C0G/NP0, 12pf, 50V, -5%/+5%, -, 0402, SMD	GRM1555C1H120GA01D	Murata
C12, C13	CAPACITOR, CERAMIC C0G/NP0, 1.2pf, 50V, -0.1pf/+0.1pf, -, 0402, SMD	GJM1555C1H1R2BB01D	Murata
C16, C18, C19, C22	CAPACITOR, CERAMIC X5R, 1uf, 10V, -10%/+10%, -55DEGC/+85DEGC, 0402, SMD	C0402C105K8PACTU	KEMET
D1, D2	Typical RED, GREEN, YELLOW, AMBER LED	HSMS-C150	Broadcom Avago
FL1	FILTER, EMI, 1500@100mhz, -, 0603, SMD	BLM18HE152SN1D	Murata
L1	INDUCTOR, CHIP, 10uh, -20%/+20%, 0.11A, 0805, SMD	CKS2125100M-T	Taiyo Yuden

L2	INDUCTOR, CHIP, 15nh, -5%/+5%, 0.3A, 0402, SMD	LQW15AN15NJ00D	Murata
L3	INDUCTOR, CHIP, 2nh, -0.3nh/+0.3nh, 0.3A, 0402, SMD	LQP03TN2N0B02D	Murata
R1, R8, R9, R10, R11, R14	Resistor	RC0402FR-0710KL	Yageo
R2, R4, R7	Resistor	ERA6AEB4023V	Panasonic
R3	Resistor	ERA6AEB4023V	Panasonic
R5, R12	Resistor	ERJ-2RKF4023X	Panasonic
R6	Resistor, Thick Film, 0, -1%/+1%, 0.063w, 50V, 0402	CRCW04020000Z0ED	Vishay
SENSOR_OUT	0.5 Mm Pitch Easy-On (TM) Type FPC Connector, 1.3 Mm Mated Height, Right Angle, ZIF, SMT, Bottom Contact, 18 Circuits,	51296-1894	Molex
U1	1A Li Ion Battery Charger	BQ24040DSQT	Texas Instruments
U2	Configurable Impedance Network Analyzer & Potentiostat with Integrated Cortex M3 Core	ADUCM350BBCZ	Analog Devices
U3	IC, Digital, 2.4ghz Simple link Wireless MCU, Pitch 0,4mm, Qfn32, SMD	CC2650F128RSMT	Texas Instruments
U4	Temperature + Rh Sensor	HDC1080DMBR	Texas Instruments
USB	USB On-The-Go (OTG) Mini-B Receptacle, Right Angle, SMT, 0.80mm (.031") Pitch, Solder Tabs with Back Cover, Recessed Type	UJ2-MIBH2-4-SMT-TR	CUI Devices
Y1	CRYSTAL, CRYSTAL OSCILLATOR, 24mhz, -15PPM/DEGC/+15PPM/DEGC, -, SMD	ABM3B-24.000MHZ-B2-T	Abracon

REFERENCES

- [1] S. C. Mukhopadhyay, “Wearable Sensors for Human Activity Monitoring: A Review,” *IEEE Sens. J.*, vol. 15, no. 3, pp. 1321–1330, Mar. 2015, doi: 10.1109/JSEN.2014.2370945.
- [2] L. Piwek, D. A. Ellis, S. Andrews, and A. Joinson, “The Rise of Consumer Health Wearables: Promises and Barriers,” *PLOS Med.*, vol. 13, no. 2, p. e1001953, Feb. 2016, doi: 10.1371/JOURNAL.PMED.1001953.
- [3] C. M. Hales, C. D. Fryar, M. D. Carroll, D. S. Freedman, Y. Aoki, and C. L. Ogden, “Differences in Obesity Prevalence by Demographic Characteristics and Urbanization Level Among Adults in the United States, 2013-2016,” *JAMA*, vol. 319, no. 23, pp. 2419–2429, Jun. 2018, doi: 10.1001/JAMA.2018.7270.
- [4] S. B. Roberts and M. B. Heyman, “Dietary Composition and Obesity: Do We Need to Look beyond Dietary Fat?,” *J. Nutr.*, vol. 130, no. 2, pp. 267S-267S, Feb. 2000, doi: 10.1093/JN/130.2.267S.
- [5] J. O. Hill, H. R. Wyatt, and E. L. Melanson, “GENETIC AND ENVIRONMENTAL CONTRIBUTIONS TO OBESITY,” *Med. Clin. North Am.*, vol. 84, no. 2, pp. 333–346, Mar. 2000, doi: 10.1016/S0025-7125(05)70224-8.
- [6] A. T. Ali and N. J. Crowther, “Health risks associated with obesity,” <http://dx.doi.org/10.1080/22201009.2005.10872117>, vol. 10, no. 2, pp. 56–61, 2014, doi: 10.1080/22201009.2005.10872117.
- [7] Y. Heianza and L. Qi, “Gene-Diet Interaction and Precision Nutrition in Obesity,” *Int. J. Mol. Sci.* 2017, Vol. 18, Page 787, vol. 18, no. 4, p. 787, Apr. 2017, doi: 10.3390/IJMS18040787.
- [8] Z. He *et al.*, “High-fat diet and chronic stress aggravate adrenal function abnormality induced by prenatal caffeine exposure in male offspring rats,” *Sci. Reports* 2017 71, vol. 7, no. 1, pp. 1–9, Nov. 2017, doi: 10.1038/s41598-017-14881-0.
- [9] D. Sankhala, M. Pali, K.-C. Lin, B. Jagannath, S. Muthukumar, and S. Prasad, “Analysis of bio-electro-chemical signals from passive sweat-based wearable electro-impedance spectroscopy (EIS) towards assessing blood glucose modulations.”
- [10] ConsumerLab, “ConsumerLab report on Wearable Technology and IoT – Ericsson - Ericsson,” www.ericsson.com, 2021. <https://www.ericsson.com/en/reports-and-papers/consumerlab/reports/wearable-technology-and-the-internet-of-things> (accessed Oct. 21, 2021).

- [11] “North American Consumer Technographics® Consumer Technology Survey, 2014,” *Forrester*, 2014, Accessed: Oct. 21, 2021. [Online]. Available: <https://www.forrester.com/North+American+Technographics+Consumer+Technology+Survey+2013/-/E-sus2092>.
- [12] “ARM technology driving the wearable trend - Embedded blog - Arm Community blogs - Arm Community.” <https://community.arm.com/arm-community-blogs/b/embedded-blog/posts/arm-technology-driving-the-wearable-trend> (accessed Oct. 22, 2021).
- [13] “Apollo4 - Ambiq.” <https://ambiq.com/apollo4/> (accessed Oct. 24, 2021).
- [14] “DE NOVO CLASSIFICATION REQUEST FOR ECG APP REGULATORY INFORMATION.”
- [15] “Microsoft_Band_Teardown-20.jpg (1000×667).” https://cdn.sparkfun.com/assets/home_page_posts/1/6/8/1/Microsoft_Band_Teardown-20.jpg (accessed Oct. 04, 2021).
- [16] “Huawei Watch 3 Teardown - iFixit.” <https://www.ifixit.com/Teardown/Huawei+Watch+3+Teardown/143845> (accessed Oct. 04, 2021).
- [17] “Fitbit Sense Teardown - iFixit.” <https://www.ifixit.com/Teardown/Fitbit+Sense+Teardown/137130> (accessed Oct. 04, 2021).
- [18] “Apple Watch Series 6 Teardown - iFixit.” <https://www.ifixit.com/Teardown/Apple+Watch+Series+6+Teardown/136694> (accessed Oct. 04, 2021).
- [19] V. Naresh and N. Lee, “A review on biosensors and recent development of nanostructured materials-enabled biosensors,” *Sensors (Switzerland)*, vol. 21, no. 4. Multidisciplinary Digital Publishing Institute, pp. 1–35, Feb. 05, 2021, doi: 10.3390/s21041109.
- [20] V. Velusamy, K. Arshak, O. Korostynska, K. Oliwa, and C. Adley, “An overview of foodborne pathogen detection: In the perspective of biosensors,” *Biotechnology Advances*, vol. 28, no. 2. pp. 232–254, Mar. 2010, doi: 10.1016/j.biotechadv.2009.12.004.
- [21] D. Grieshaber, R. MacKenzie, J. Vörös, and E. Reimhult, “Electrochemical Biosensors - Sensor Principles and Architectures,” *Sensors*, vol. 8, no. 3, pp. 1400–1458, Mar. 2008, doi: 10.3390/s80314000.
- [22] A. M. Pisoschi, “Potentiometric Biosensors: Concept and Analytical Applications-An Editorial,” *Biochem. Anal. Biochem.*, vol. 5, no. 3, 2016, doi: 10.4172/2161-1009.1000e164.

- [23] B. D. Malhotra and M. A. Ali, “Nanomaterials in Biosensors,” in *Nanomaterials for Biosensors*, Elsevier, 2018, pp. 1–74.
- [24] M. S. Alaejos and F. J. García Montelongo, “Application of amperometric biosensors to the determination of vitamins and alpha-amino acids,” *Chem. Rev.*, vol. 104, no. 7, pp. 3239–66, Jul. 2004, doi: 10.1021/cr0304471.
- [25] R. Radhakrishnan, I. I. Suni, C. S. Bever, and B. D. Hammock, “Impedance biosensors: Applications to sustainability and remaining technical challenges,” in *ACS Sustainable Chemistry and Engineering*, Jul. 2014, vol. 2, no. 7, pp. 1649–1655, doi: 10.1021/sc500106y.
- [26] D. Zhou, D. S. Ha, and D. J. Inman, “Ultra low-power active wireless sensor for structural health monitoring,” *Smart Struct. Syst.*, vol. 6, no. 5–6, pp. 675–687, 2010, doi: 10.12989/SSS.2010.6.5_6.675.
- [27] “File:Lissajous phase.svg - Wikimedia Commons.”
https://commons.wikimedia.org/wiki/File:Lissajous_phase.svg#metadata (accessed Oct. 04, 2021).
- [28] G. Qu *et al.*, “A 0.28m Ω -sensitivity 105dB-dynamic-range electrochemical impedance spectroscopy soc for electrochemical gas detection,” in *Digest of Technical Papers - IEEE International Solid-State Circuits Conference*, 2018, vol. 61, pp. 286–288, doi: 10.1109/ISSCC.2018.8310296.
- [29] L. C. Clark and C. Lyons, “ELECTRODE SYSTEMS FOR CONTINUOUS MONITORING IN CARDIOVASCULAR SURGERY,” *Ann. N. Y. Acad. Sci.*, vol. 102, no. 1, pp. 29–45, 1962, doi: 10.1111/j.1749-6632.1962.tb13623.x.
- [30] J. Ngeh-Ngwainbi, A. A. Suleiman, and G. G. Guilbault, “Piezoelectric crystal biosensors,” *Biosens. Bioelectron.*, vol. 5, no. 1, pp. 13–26, Jan. 1990, doi: 10.1016/0956-5663(90)80023-7.
- [31] D. Le Guillou-Buffello, M. Gindre, P. Johnson, P. Laugier, and V. Migonney, “An alternative quantitative acoustical and electrical method for detection of cell adhesion process in real-time,” *Biotechnol. Bioeng.*, vol. 108, no. 4, pp. 947–962, Apr. 2011, doi: 10.1002/bit.23005.
- [32] H. Muramatsu, J. M. Dicks, E. Tamiya, and I. Karube, “Piezoelectric Crystal Biosensor Modified with Protein A for Determination of Immunoglobulins,” *Anal. Chem.*, vol. 59, no. 23, pp. 2760–2763, 1987, doi: 10.1021/ac00150a007.
- [33] M. D. Ward and D. A. Buttry, “In situ interfacial mass detection with piezoelectric transducers,” *Science*, vol. 249, no. 4972, pp. 1000–1007, 1990, doi: 10.1126/science.249.4972.1000.

- [34] W. R. Seitz, "Chemical sensors based on fiber optics," *Anal. Chem.*, vol. 56, no. 1, pp. 16A-34A, Jan. 1984, doi: 10.1021/ac00265a001.
- [35] M. A. Arnold, "Enzyme-Based Fiber Optic Sensor," *Anal. Chem.*, vol. 57, no. 2, pp. 565–566, Feb. 1985, doi: 10.1021/ac50001a055.
- [36] K. J. C. AS, de Á. BE, and W. J, "Wearable biosensors for healthcare monitoring," *Nat. Biotechnol.*, vol. 37, no. 4, pp. 389–406, Apr. 2019, doi: 10.1038/S41587-019-0045-Y.
- [37] H. PI and G. MJ, "Disposable electrochemical biosensors," *Analyst*, vol. 116, no. 12, pp. 1217–1220, 1991, doi: 10.1039/AN9911601217.
- [38] F. JE and H. HA, "Electrochemical biosensors," *Anal. Chem.*, vol. 59, no. 15, pp. 933–944, 1987, doi: 10.1021/AC00142A001.
- [39] B. DS *et al.*, "Design and in vitro studies of a needle-type glucose sensor for subcutaneous monitoring," *Anal. Chem.*, vol. 63, no. 17, pp. 1692–1696, Sep. 1991, doi: 10.1021/AC00017A008.
- [40] W. GS and G. R, "Biosensors for real-time in vivo measurements," *Biosens. Bioelectron.*, vol. 20, no. 12, pp. 2388–2403, Jun. 2005, doi: 10.1016/J.BIOS.2004.12.003.
- [41] T. Battelino *et al.*, "Clinical targets for continuous glucose monitoring data interpretation: Recommendations from the international consensus on time in range," *Diabetes Care*, vol. 42, no. 8, pp. 1593–1603, Aug. 2019, doi: 10.2337/dci19-0028.
- [42] Z. Dai, I. G. Rosen, C. Wang, N. P. Barnett, and S. E. Luczak, "Using drinking data and pharmacokinetic modeling to calibrate transport model and blind deconvolution based data analysis software for transdermal alcohol biosensors," *Math. Biosci. Eng.*, vol. 13, no. 5, pp. 911–934, Mar. 2016, doi: 10.3934/mbe.2016023.
- [43] P. JK, N. JM, V. RA, M. CA, and A. DH, "Cyclopentane-modified PNA improves the sensitivity of nanoparticle-based scanometric DNA detection," *Chem. Commun. (Camb).*, no. 16, pp. 2101–2103, Apr. 2005, doi: 10.1039/B418383E.
- [44] H. T.-T. in *Biotechnology and* undefined 1998, "Cutting out the middleman: DNA biosensors based on electrochemical oxidation," *Elsevier*, Accessed: Oct. 24, 2021. [Online]. Available: <https://www.sciencedirect.com/science/article/pii/S0167779997011621>.
- [45] W. J, "From DNA biosensors to gene chips," *Nucleic Acids Res.*, vol. 28, no. 16, pp. 3011–3016, Aug. 2000, doi: 10.1093/NAR/28.16.3011.
- [46] O. KJ and G. JJ, "An introduction to electrochemical DNA biosensors," *Analyst*, vol. 132, no. 7, pp. 603–610, 2007, doi: 10.1039/B701816A.

- [47] R. Lin, F. Brown, S. James, J. Jones, and E. Ekinici, "Continuous glucose monitoring: A review of the evidence in type 1 and 2 diabetes mellitus," *Diabet. Med.*, vol. 38, no. 5, May 2021, doi: 10.1111/dme.14528.
- [48] I. B. Hirsch and C. A. Verderese, "Professional flash continuous glucose monitoring with ambulatory glucose profile reporting to supplement A1C: Rationale and practical implementation," *Endocr. Pract.*, vol. 23, no. 11, pp. 1333–1344, Aug. 2017, doi: 10.4158/EP171962.RA.
- [49] A. Wood, D. O'Neal, J. Furler, and E. I. Ekinici, "Continuous glucose monitoring: a review of the evidence, opportunities for future use and ongoing challenges," *Internal Medicine Journal*, vol. 48, no. 5, pp. 499–508, 2018, doi: 10.1111/imj.13770.
- [50] O. Schnell *et al.*, "Role of Continuous Glucose Monitoring in Clinical Trials: Recommendations on Reporting," *Diabetes Technology and Therapeutics*, vol. 19, no. 7, Mary Ann Liebert Inc., pp. 391–399, Jul. 01, 2017, doi: 10.1089/dia.2017.0054.
- [51] O. Moser *et al.*, "Glucose management for exercise using continuous glucose monitoring (CGM) and intermittently scanned CGM (isCGM) systems in type 1 diabetes: position statement of the European Association for the Study of Diabetes (EASD) and of the International Society of," *Diabetologia*, vol. 63, no. 12, pp. 2501–2520, Oct. 2020, doi: 10.1007/s00125-020-05263-9.
- [52] S. R. Patton, "Adherence to glycemic monitoring in diabetes," *Journal of Diabetes Science and Technology*, vol. 9, no. 3, J Diabetes Sci Technol, pp. 668–675, May 01, 2015, doi: 10.1177/1932296814567709.
- [53] R. D. Munje, S. Muthukumar, and S. Prasad, "Lancet-free and label-free diagnostics of glucose in sweat using Zinc Oxide based flexible bioelectronics," *Sensors Actuators, B Chem.*, vol. 238, pp. 482–490, 2017, doi: 10.1016/j.snb.2016.07.088.
- [54] C. Beasley, "Potentiostat Fundamentals."
- [55] G. Instruments, "Reference 3000TM Potentiostat/Galvanostat/ZRA Operator's Manual," 2012, Accessed: Nov. 14, 2021. [Online]. Available: www.gamry.com/service-support/.
- [56] R. D. Munje, S. Muthukumar, and S. Prasad, "Lancet-free and label-free diagnostics of glucose in sweat using Zinc Oxide based flexible bioelectronics," *Sensors Actuators, B Chem.*, vol. 238, pp. 482–490, Jan. 2017, doi: 10.1016/j.snb.2016.07.088.
- [57] D. Sankhala, S. Muthukumar, and S. Prasad, "A Four-Channel Electrical Impedance Spectroscopy Module for Cortisol Biosensing in Sweat-Based Wearable Applications," *SLAS Technol.*, vol. 23, no. 6, pp. 529–539, Feb. 2018, doi: 10.1177/2472630318759257.

- [58] F. N. Hooge, “1/f noise sources,” *IEEE Trans. Electron Devices*, vol. 41, no. 11, pp. 1926–1935, Nov. 1994, doi: 10.1109/16.333808.
- [59] F. N. Hooge, T. G. M. Kleinpenning, and L. K. J. Vandamme, “Experimental studies on 1/f noise,” *Reports on Progress in Physics*, vol. 44, no. 5. IOP Publishing, pp. 479–532, 1981, doi: 10.1088/0034-4885/44/5/001.
- [60] J. B. Johnson, “Thermal Agitation of Electricity in Conductors,” *Phys. Rev.*, vol. 32, no. 1, pp. 97–109, Jul. 1928, doi: 10.1103/PhysRev.32.97.
- [61] B. Razavi, *Design of Analog CMOS Integrated Circuits*, 1st ed. New York, NY, USA: McGraw-Hill, Inc., 2001.
- [62] A. Hassibi, R. Navid, R. W. Dutton, and T. H. Lee, “Comprehensive study of noise processes in electrode electrolyte interfaces,” *J. Appl. Phys.*, vol. 96, no. 2, pp. 1074–1082, 2004, doi: 10.1063/1.1755429.
- [63] R. D. Munje, S. Muthukumar, B. Jagannath, and S. Prasad, “A new paradigm in sweat based wearable diagnostics biosensors using Room Temperature Ionic Liquids (RTILs),” *Sci. Rep.*, vol. 7, no. 1, p. 1950, 2017, doi: 10.1038/s41598-017-02133-0.
- [64] W. L. Clarke, “The Original Clarke Error Grid Analysis (EGA),” in *Diabetes Technology and Therapeutics*, Oct. 2005, vol. 7, no. 5, pp. 776–779, doi: 10.1089/dia.2005.7.776.

BIOGRAPHICAL SKETCH

Devangsingh Sankhala was born in Jodhpur, in the state of Rajasthan, India in 1992. He completed his schooling at Vallabh Vidyanagar, in the state of Gujarat, India. He completed his Bachelor of Engineering, specializing in Electronics and Communications Engineering from G. H. Patel College of Engineering and Technology, Vallabh Vidyanagar, India in May 2014. He has served as a Power Distribution Systems Design and Manufacturing Engineer at G. M. Enterprises, Vithal Udyognagar, India for five years while also working on his bachelor's degree. He joined The University of Texas at Dallas in August 2015 in the master's program in Electrical Engineering, thereafter, graduating in 2017 to join the PhD program.

During his PhD program, he has interned at EnLiSense LLC, specializing in field deployment of low-power wearable hardware and Texas Instruments Inc. in semiconductor reliability simulations. His current research interests include mixed-signal integrated circuit design, and system level circuit design towards making low-power wearable devices and creating hardware-software codesign platforms for health data analytics.

CURRICULUM VITAE

Devangsingh G. Sankhala

November 11, 2021

Contact Information:

Department of Electrical Engineering

The University of Texas at Dallas

800 W Campbell Rd

Richardson, TX 75080-3021, USA

Educational History:

BE, Electronics and Communication Engineering, Gujarat Technological University, 2014

MS, Electrical Engineering, The University of Texas at Dallas, 2017

Employment History:

Reliability Engineering Intern (ATD), Texas Instrument Inc., Aug 2020 – Dec 2020

Hardware and Systems Engineering Intern, EnLiSense LLC, Aug 2019 – Dec 2019

Hardware and Systems Engineering Intern, EnLiSense LLC, May 2018 – Aug 2018

Graduate Research Assistant, The University of Texas at Dallas, Aug 2017 – Dec 2021

Electrical Engineer, GM Enterprises, VU Nagar, India, Aug 2010 – Jun 2015